

Università degli Studi di Genova  
Scuola di Scienze Matematiche, Fisiche e Naturali

Anno Accademico 2024/2025

Tesi di Laurea Magistrale in Fisica  
Curriculum di Fisica delle Interazioni Fondamentali

**Opening Pandora's box**  
**A dedicated study of the automatic event**  
**reconstruction in the ICARUS-T600**  
**experiment**

**Candidato**  
Mattia Sotgia

**Relatrice**  
Dr. Alice Campani  
**Relatore**  
Prof. Marco Pallavicini

**Correlatrice**  
Prof. Carla Biggio

Genova, 15 ottobre 2025



I have done something very bad today by  
proposing a particle that cannot be  
detected; it is something no theorist should  
ever do.

---

*(Wolfgang Pauli)*



## Abstract

The three-flavor neutrino mixing minimal extension of the Standard Model (SM) has been established by a number of experiments in the past two decades. However, a series of experimental anomalies were observed, indicating a possible hint of the existence of a fourth neutrino, called *sterile neutrino* because it does not undergo weak interaction.

This  $3 + 1$  extension of the SM is the main physics target of the ICARUS experiment as part of the Short-Baseline Neutrino (SBN) program at Fermilab. The ICARUS-T600 760-ton detector is a Liquid Argon Time Projection Chamber (LAr-TPC) successfully employed at the LNGS laboratories for a three-year physics run and now collecting data at Fermi National Accelerator Laboratory (FNAL). The physics program of the ICARUS experiment also includes the measurement of neutrino-Argon cross sections employing the off-axis Neutrino at the Main Injector (NuMI) beam and several Beyond Standard Model studies.

The automatic TPC event reconstruction in ICARUS is performed using the Pandora Pattern Finding Algorithm framework that performs a 3D reconstruction of the image recorded in the collected event, including the identification of interaction vertices and the classification of tracks and showers inside the TPC.

In view of the standalone ICARUS oscillation  $\nu_\mu$ CC analysis and of the future combined SBN oscillation analysis, a thorough evaluation of the performances of reconstruction chain, as well as the systematic uncertainties induced on the reconstructed neutrino energy spectrum is essential. The main objective of this work is to evaluate the performances of single steps of the reconstruction sequence, while possibly testing improvements of the machine learning algorithms employed in specific stages of the chain.



# Contents

Introduction,	1
<b>Chapter 1.</b>	Active and sterile neutrinos, 5
1.1.	Neutrinos: a journey across history, 5
1.2.	Neutrinos in the Standard Model, 7
1.2.1.	Neutrino interactions, 8
1.2.2.	Flavour oscillations, 12
1.3.	Short baseline anomalies, 24
1.3.1.	The sterile neutrino hypothesis, 29
1.3.2.	Experimental status and future perspectives, 31
<b>Chapter 2.</b>	The SBN program at Fermilab and the ICARUS experiment, 37
2.1.	The Short Baseline Neutrino program at Fermilab, 37
2.1.1.	Neutrino beam, 41
2.2.	Liquid Argon Time Projection Chambers, 44
2.3.	The SBN near detector: SBND, 48
2.4.	The ICARUS-T600 detector, 49
2.4.1.	The ICARUS detector subsystems, 54
<b>Chapter 3.</b>	ICARUS data processing and event reconstruction, 57
3.1.	Data acquisition, 57
3.2.	ICARUS Data processing, 60
3.2.1.	Light reconstruction, 62
3.2.2.	Cosmic ray tagger reconstruction, 62
3.2.3.	Wireplanes signal reconstruction, 65
3.3.	TPC event reconstruction, 68
3.3.1.	Geometry of the ICARUS detector, 70

3.3.2.	Pandora approach to the event reconstruction,	71
3.3.3.	PandoraFastReco: <i>unambiguous</i> cosmic hits removal,	72
3.3.4.	PandoraNeutrino: topological neutrino event reconstruction,	77
3.3.5.	PandoraCosmic: cosmic-ray muon reconstruction,	80
3.4.	Calorimetry and particle identification,	80
3.5.	SPINE: machine learning particle identification,	82
3.6.	Simulation of the full detector,	84
<b>Chapter 4.</b>	<b>Validating and evaluating the efficiency of Pandora reconstruction,</b>	<b>85</b>
4.1.	Data sample and selection,	86
4.2.	<i>Cheating</i> Pandora reconstruction,	90
4.2.1.	Two-dimensional clustering,	92
4.2.2.	Three-dimensional vertex,	97
4.2.3.	Three-dimensional track and shower reconstruction,	101
4.2.4.	Particle hierarchy reconstruction,	103
4.2.5.	Particle classification,	107
4.3.	Efficiency evaluation for different reconstruction stages,	110
4.3.1.	Results,	111
4.3.2.	Extracting the selection efficiency,	115
4.4.	Impact of the vertex reconstruction,	120
4.4.1.	Future outlook: improving the vertex creation algorithm,	123
	Conclusions,	129
<b>Appendix A.</b>	<b>Acronyms,</b>	<b>A-1</b>
	Bibliography,	i

# List of Figures

1.1.	(Anti)Neutrino-matter cross-sections . . . . .	9
1.2.	Diagrams of some interaction topologies for neutrinos in matter . . . . .	10
1.3.	The solar neutrino flux produced by all the reactions inside Sun's core . . . . .	14
1.4.	SNO+SK results for the “solar neutrino problem” . . . . .	17
1.5.	MSW effect is solar neutrinos . . . . .	20
1.6.	Neutrino mass ordering . . . . .	21
1.7.	LSND anomalous excess . . . . .	25
1.8.	The LNSD detector and results . . . . .	27
1.9.	MiniBooNE detector and results . . . . .	28
1.10.	Neutrino mass ordering with the sterile state . . . . .	30
1.11.	Parameter spaces in both the $\nu_e$ appearance and $\nu_\mu$ disappearance channels . . . . .	34
1.12.	Status of the global experimental searches . . . . .	35
2.1.	Electron neutrino appearance probability in the 3 + 1 sterile oscillation scenario . . . . .	39
2.2.	SBN sensitivity plots in both appearance and disappearance channels . . . . .	40
2.3.	Fermilab Accelerator complex . . . . .	42
2.4.	BNB flux predictions at the near and far detectors . . . . .	43
2.5.	LArTPC illustration . . . . .	45
2.6.	T300 module Induction-2 and collection planes wire orientation . . . . .	50
2.7.	ICARUS TPC wires and field cage . . . . .	51
2.8.	ICARUS detector illustration . . . . .	52
2.9.	BNB and NuMI collected POT . . . . .	53
3.1.	ICARUS DAQ illustration . . . . .	59
3.2.	<i>Stage0</i> and <i>Stage1</i> data processing pipeline . . . . .	61
3.3.	PMT reconstructed <i>OpHits</i> . . . . .	63

3.4. CRT Hit reconstruction in space . . . . .	64
3.5. TPC plane signal . . . . .	65
3.6. TPC signal processing . . . . .	67
3.7. LArPandora output data products . . . . .	72
3.8. Overview of Pandora reconstruction chain . . . . .	73
3.9. PandoraFastReco path illustration . . . . .	74
3.10. Three-dimensional reconstruction helper tools . . . . .	76
3.11. PandoraCosmic and PandoraNeutrino paths illustration . . . . .	78
3.12. SPINE end-to-end machine learning approach . . . . .	83
3.13. LArSoft complete overview . . . . .	84
4.1. CheatingClusterCreation versus TrackClusterCreation algorithm . . . . .	93
4.2. Definition of hit purity and completeness . . . . .	95
4.3. Hit purity and completeness with CheatingClusterCreation algorithm . .	96
4.4. Hit completeness versus number of hits on collection plane . . . . .	97
4.5. Example of an event for which the reconstructed muon completeness is lower than 0.4, i.e., $\mu_{\text{completeness}} \simeq 0.318$ . In this case the lower completeness is due to the true muon particle being split into two slices, of which only one (slice A) is reconstructed as corresponding to a $1\mu5p$ interaction and thus selected as a signal candidate. . . . .	98
4.6. CheatingVertexCreation and CheatingVertexSelection algorithms . . . . .	99
4.7. CheatingVertexCreation with an OoFV vertex . . . . .	101
4.8. Vertex displacement from truth . . . . .	102
4.9. Hit purity and completeness with CheatingPfoCreation algorithm . . . . .	104
4.10. True versus reconstructed primary proton multiplicity . . . . .	105
4.11. Particle hierarchy cheating failure modes . . . . .	108
4.12. Track and shower classification BDT score . . . . .	109
4.13. Evaluation of the reconstruction and selection efficiency for different configurations . . . . .	113
4.14. Event reconstruction and selection efficiency for different cuts . . . . .	114
4.15. Evaluation of the reconstruction and selection efficiency for different configurations with the modified event selection . . . . .	118
4.16. Event reconstruction and selection efficiency with the cheated vertex creation . . . . .	121
4.17. PID scores with the cheated vertex creation . . . . .	124

*List of Figures* v

- 4.18. Working principle of the DL vertex algorithm . . . . . 126



# Introduction

Neutrinos are the most abundant particles in the universe. Billions of these elusive particles pass through each square centimetre every second, primarily originating from our neighbouring star, the Sun. Within the Sun's core, they are created by nuclear reactions and then travel unaltered to the Earth due to their weakly interactive nature. Other sources of neutrinos include core-collapse supernovae, cosmic rays interacting within the Earth's atmosphere and nuclear reactors and accelerator complexes.

The discovery of neutrino oscillations, and thus the need to include a mass term for neutrinos, is a striking proof of physics Beyond the Standard Model (BSM). Given the current limits on neutrino masses and their smallness compared with other Standard Model particles, several alternative mechanisms for their generation have been proposed over the years. In general, mechanisms that generate neutrino masses require the introduction of new particle states beyond the Standard Model, none of which have yet been observed. Adding these particle states would substantially modify neutrino-related observables and affect oscillation phenomenology.

Interest in this area has recently been driven by a series of anomalous neutrino measurements in short-baseline oscillation experiments at particle accelerators, such as LSND and MiniBooNE, as well as in Gallium-based experiments, such as GALLEX, SAGE and BEST, and in reactor-based experiments, including recently Neutrino-4.

However, none of these experimental anomalies proved to be definitive, and the overall measurement scenario is far from being understood, with large inconsistencies between results derived from different channels. A programme to achieve a sensitivity larger than  $5\sigma$  on multiple short-baseline oscillation channels is essential to test past measurements and provide a comprehensive overview of neutrino oscillation physics.

The Short Baseline Neutrino (SBN) programme at Fermilab was designed with this goal and is a short-baseline, multi-detector experimental project based at Fermilab and taking data along the Booster Neutrino Beam (BNB) baseline. All the detectors are liquid

## 2 Introduction

argon time projection chambers (LArTPCs), exploiting the high-precision calorimetric capabilities and millimetre-scale three-dimensional tracking capabilities this technique guarantees to achieve unprecedented sensitivity in the search for sterile neutrinos.

The SBND detector operates closer to the BNB beam source, at a distance of 110 m acting as the Near Detector for the SBN program; it is relevant for the SBN program since it provides a flux monitor, measuring the unoscillated neutrino spectrum.

The ICARUS T600 detector acts as the SBN Far Detector (SBN-FD) at a baseline of 600 m. The locations of the ICARUS detector and of the SBN Near Detector, SBND, were chosen to optimise sensitivity to neutrino oscillations and minimise the impact of flux systematics. The ICARUS detector is also exposed to the flux of neutrinos coming from the Neutrino from the Main Injector (NuMI) Beam, crossing the detector  $\sim 6^\circ$  off-axis with respect to the direction of BNB. The ICARUS detector has now completed its fourth physics campaign, with the first data-taking campaign conducted with the full SBN detector suite fully operational and in physics mode. With a fraction of these data corresponding to the second data-taking campaign, the collaboration has started investigating the  $\nu_\mu$ -disappearance channel, analysing the two among the simplest topologies, i.e.,  $1\mu 1p$  and  $1\mu Np$  events.

In order to improve the event selection efficiency and minimise systematic uncertainties relating to reconstruction efficiency, a thorough investigation of event reconstruction in the ICARUS TPC is necessary. This should be accompanied by an effort to align the signal processing and event reconstruction chains of the experiments involved in the SBN program, in view of future joint analyses.

Among the steps involved in event processing and reconstruction, one of the most important is the creation of particle objects from the charge signal deposited on the readout wireplanes, followed by the construction of the event hierarchy that entails the identification of the interaction structure and especially primary particles originating directly from the interaction vertex. This serves as a starting point for subsequent event processing steps and analyses. This process is performed using topological and calorimetric information by two separate set of tools: the former following a machine-learning-based approach and the latter relying on traditional rule-based, physics-informed methods.

Widespread among multiple experiments employing the LArTPC technology, the traditional, physics-informed approach to the event reconstruction is based on a comprehensive set of algorithms known as Pandora. Pandora was developed to be highly modular, allowing each of the algorithms to be used in different stages of the event reconstruction chain and to be updated by new, more efficient algorithms solving the same

task. This modular approach also permits the introduction of algorithms that alter the reconstruction to allow usage of Monte Carlo information for simulated events. This approach is key to making targeted improvements to the event reconstruction chain, which is ultimately the aim of this work.

To be able to use these tools, a preliminary validation of the algorithms involved in the reconstruction and their altered, truth-based version is required; once algorithms were validated for use within the ICARUS event reconstruction, the focus became their joint usage with a targeted event selection to draw an estimate of the efficiencies of the main reconstruction steps. This will allow targeted improvements to reconstruction stages, thereby laying the ground for future work, including but not limited to the upcoming  $\nu_e$ -appearance analysis, where refined reconstruction tools/methods/algorithms can provide improved shower-like particle reconstruction. Reconstructing this type of interaction is challenging due to the complex final state topology it produces.

The outline of the thesis is the following:

- [chapter 1](#) is devoted to introducing the theoretical and experimental framework of the Standard Model of Particle Physics, and provides an overview of the present status of neutrino physics, including their classical picture, the phenomenology of neutrino oscillator behaviour, and the main anomalies driving the current sterile neutrino scenario.
- [chapter 2](#) provides a detailed description of the ICARUS T600 detector, its three sub-systems (the Time Projection Chamber, the light collection system, and the cosmic ray tagging system), and its main physics goals, both in the context of the SBN program and as a standalone experiment.
- [chapter 3](#) describes the major steps involved in the data acquisition and data signal processing with details on the tools employed to reconstruct physical information on the measured interactions for each ICARUS subsystem and especially on the TPC signal processing and event reconstruction.
- In [chapter 4](#) the specific set of tools employed to study the efficiency of the event reconstruction is described and validated; the strategy used to perform the analysis to extract the efficiencies of the stages involved in the event reconstruction is presented. Finally, based on the outcome of this study, the next steps to improve specific stages of the reconstruction chain are illustrated.



# 1

## Active and sterile neutrinos

It doesn't matter how beautiful your theory is, it doesn't matter how smart you are. If it doesn't agree with experiment, it's wrong.

---

(Richard P. Feynman)

### 1.1. Neutrinos: a journey across history

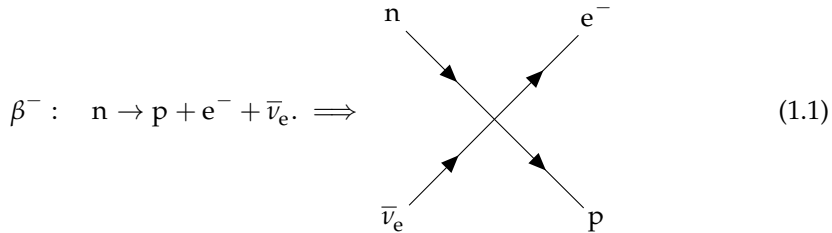
Dating back to 1914, the history of neutrinos began with the first paper published by Sir James Chadwick [1], who, investigating the phenomenology of beta decays, discovered that the emitted electron energy spectra was not a single vertical emission line (delta shaped) but a continuous spectrum.

The  $\beta$  decay process, up until then, was thought to be just the emission of a single electron from a neutron decaying at rest to a proton,  $n \rightarrow p + e^-$ , and so the electron was expected to carry all the neutron energy. A continuous  $e^-$  spectrum broke this expectation. W. Pauli in 1930 proposed the idea that the emission of the electron occurred along with the emission of another fermionic particle, far less massive than the electron, carrying no electric charge [2]. Even if Pauli did not label this particle “neutrino” yet, its idea was all contained in his letter.

Enrico Fermi, a prominent scientist of that era, developed Pauli’s idea, calling this new particle *neutrino* [3, 4] — from *neutron*, the only chargeless particle discovered so far, aside from photons — adding the suffix *-ino*, meaning smaller (and lighter). Fermi’s idea was the first *field theory* of quantum mechanics, suggesting that the  $\beta$  decay could be formalized as a four-fermion point interaction, involving a neutron decaying to a proton

## 6     Chapter 1. Active and sterile neutrinos

to produce an electron and a neutrino,



Fermi's effective theory managed to explain the  $\beta$  decay energy spectrum of the electron successfully, even preserving the angular momentum conservation. The value of the coupling constant measured by Fermi for this interaction, called  $G_F$ , was

$$G_F^{(\beta)} \simeq 1.166 \times 10^{-5} / \text{GeV}^2, \quad (1.2)$$

implying that this type of interaction had a minimal cross section, which justified calling this type of interaction *weak*. Up until then, however, the neutrino was yet to be "directly" observed. It took twenty-six years of experimental efforts to actually detect the traces of this "ghostly" particle. The first experimental observation of electron antineutrinos produced by beta decays from the Savannah River reactor happened in 1956; a team led by F. Reines and C. L. Cowan observed the signature of inverse beta decay process (IB)

$$\bar{\nu}_e + p \rightarrow n + e^+ \quad (1.3)$$

in a water tank. The positron quickly finds an electron in water and produces two gamma rays by pair annihilation. This does not provide a unique signature, since there are other processes producing two gamma rays in water. So the complete event signature required the additional detection of the neutron. Using cadmium — a strong neutron absorber — dissolved in water, photons from the de-excitation of cadmium were detected, a mere 5  $\mu\text{s}$  after the prompt photons from IBD [5].

The world of particle physics was discovering new particles very fast and putting together the picture we today know as the Standard Model (SM) of particle physics: in the same years the electron neutrino was discovered, a team led by Carl D. Anderson and Seth Neddermeyer discovered the muon by detecting charged particles with weather balloons at different heights in the atmosphere, which they described as the heavier relative to the electron, since it showed a less prominent curvature than the electron when passed through a magnetic field; this discovery was later confirmed [6–8]. The discovery

led many physicists to start questioning the relationship between neutrinos and muons/electrons. In 1959 Bruno Pontecorvo examined this problem and questioned himself about the nature of neutrinos [9]: are neutrinos produced alongside electrons and neutrinos produced alongside muons the same? This led to the neutrino experiment at Brookhaven National Laboratories (BNL) guided by L. M. Lederman, M. Schwarz, and J. Steinberger. At BNL, using the Brookhaven Alternating Gradient Synchrotron (AGS), protons were accelerated toward a beryllium target: the resulting kaons and pions decayed in-flight, producing muons and muon antineutrinos. Using a spark chamber located behind a concrete wall stopping the produced muons, they were able to detect the muons produced by the interaction of muon antineutrinos but saw no electron-like event. This represented strong proof that there are at least two *families* of neutrinos [10].

In 1989 the ALEPH detector at the LEP  $e^+e^-$  collider studied the  $Z^0$  resonance and set strong constraints on the number of neutrino families  $N_\nu \simeq 3$  [11], thereby ruling out the possibility of a fourth (active) neutrino family and suggesting a third neutrino should exist. In 1975 the third “*heavier*” brother of the electron and the muon, the tau, was discovered [12]; this discovery led physicists to expect that a third neutrino had to exist. The tau neutrino signature was finally detected in 2000 in the DONuT (Direct Observation of the Nu Tau) experiment at Fermilab, twenty-five years after the discovery of the tau lepton.

## 1.2. Neutrinos in the Standard Model

The state of the art of particle physics is defined by the Standard Model (SM). In the SM of particle physics the strong, weak and electromagnetic interactions are described by the gauge symmetries  $SU(3)_C \times SU(2)_L \times U(1)_Y$  [13]. The SM is the most comprehensive theory of particle physics, and has been experimentally tested with high accuracy. Neutrinos in the minimal SM are massless fermions — meaning that their spin is half-integer — that do not have strong nor electromagnetic interactions. As for all the particles in the SM, we can define the helicity  $\mathcal{H} = \boldsymbol{\sigma} \cdot \mathbf{p} / |\mathbf{p}|$  as the projection of the spin  $\boldsymbol{\sigma}$  on the particle momentum  $\mathbf{p}$ ; however, differently from other particles of the SM, only left-handed ( $\mathcal{H} = -1$ ) neutrinos and right-handed ( $\mathcal{H} = +1$ ) antineutrinos have been observed. The experimental evidence of this peculiarity of neutrinos was first seen by M. Goldhaber, L. Grodzins and A. W. Sunyar in 1958 [14]. Helicity for massless particles is equivalent to their chirality (or handedness), which is why we can define positive helicity as right-handed antineutrinos and negative helicity as left-handed neutrinos.

The SM includes three families of neutrinos, each paired with the corresponding charged lepton: the electron neutrino  $\nu_e$ , the muon neutrino  $\nu_\mu$  and the tau neutrino  $\nu_\tau$ , and the corresponding three antiparticles.

### 1.2.1. Neutrino interactions

In the SM neutrinos can, therefore, only interact via the weak interaction, which is mediated by three vector bosons,  $W^\pm$  and  $Z^0$ . The experimental evidence of the  $W^\pm$  and  $Z^0$  bosons, constituting a strong proof of the SM theory, arrived between 1982 and 1983. The experiments UA1/UA2, led by Nobel physics laureate Carlo Rubbia, and located inside the CERN-Sp $\bar{p}$ S accelerator ring, saw signatures of these bosons with proton-antiproton collisions with a high significance [15, 16].

The types of interactions that are possible for neutrinos are multiple. In general a neutrino can interact with other SM particles via the exchange of either a  $W$  boson — thus resulting in a charged current (CC) event, with the corresponding charged lepton on the other side of such vertices — or of a  $Z$  boson — resulting in a neutral current (NC) interaction, where the outgoing particle is the same flavour neutrino. In both cases, the diagram is completed by stitching on the other side of the boson line the interaction with the matter. The interaction in its entirety is required to conserve both charge and momentum. According to what the final state particles of the interaction are, the interactions themselves can be classified. A brief description of the most relevant interaction modes is provided in the following.

**Charged current interactions** Neutrino-matter interactions show a rich phenomenology that varies dramatically across different energy scales. Multiple mechanisms determine the total cross-section of the  $\nu$ -matter interaction, as shown by Figure 1.1.

- Starting on the lower part of the energy spectrum, the first mechanism we encounter is the so-called quasielastic interaction. This mechanism has an energy peak around  $E_\nu \simeq \mathcal{O}(1\text{ GeV})$ . In a QE event, the neutrino scatters off an entire nucleon rather than its constituent partons, converting the neutron to a proton and emitting a charged lepton

$$\nu_\ell + n \rightarrow \ell^- + p, \quad \bar{\nu}_\ell + p \rightarrow \ell^+ + n. \quad (1.4)$$

The diagrams corresponding to such processes are shown in Figure 1.2a. The QE neutrino cross-section can be accurately described by the V-A interaction theory,

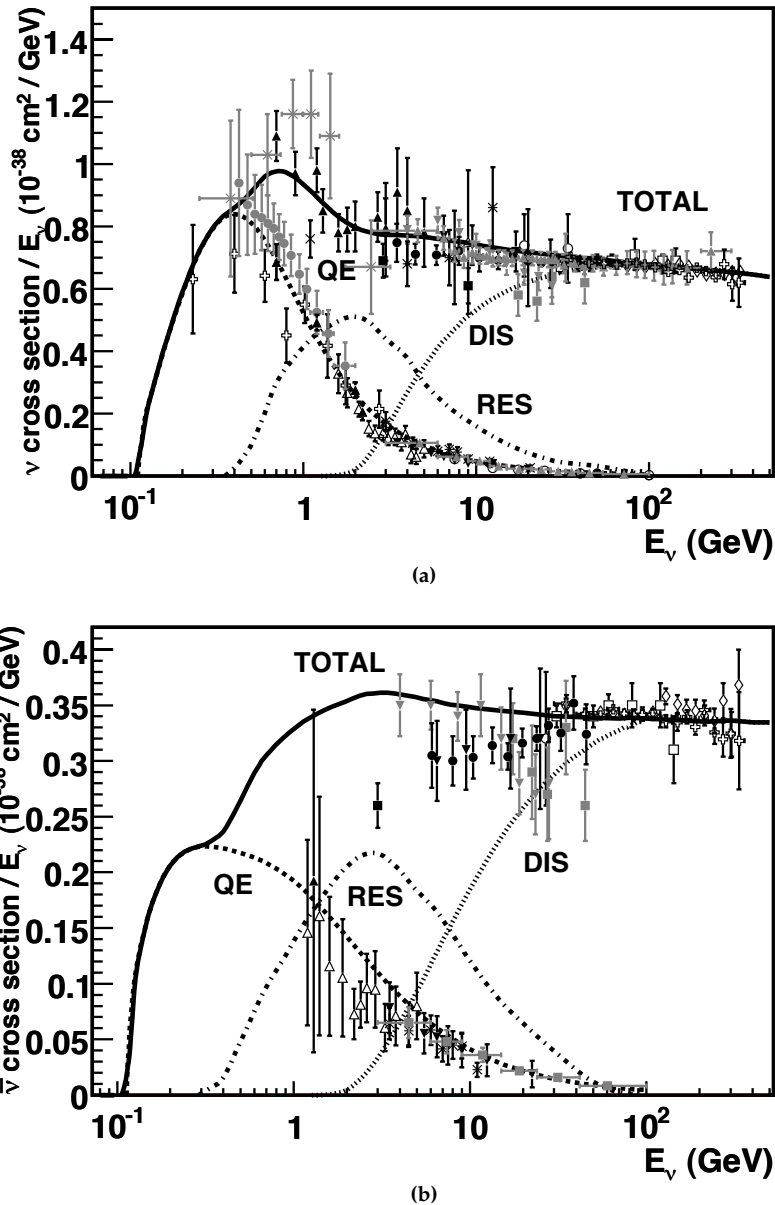


**Figure 1.1.** Cross-section measurements for (anti)neutrino-nucleon charged current interactions, showing the contributions of quasi-elastic, resonant, and deep-inelastic-scattering processes, both for neutrinos (a) and for antineutrinos (b). Figures adapted from Ref. [17].

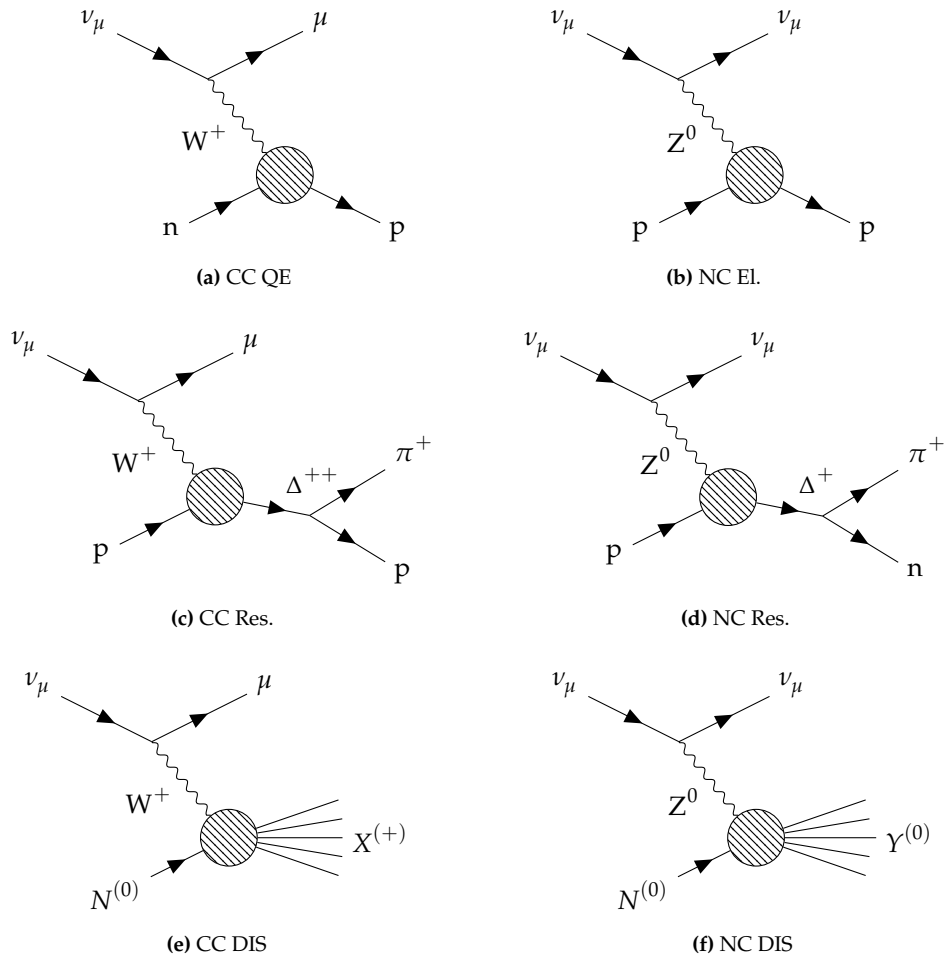


**Figure 1.2.** Diagrams of some interaction topologies for neutrinos in matter

being an effective theory between the Fermi four-point interaction and the SM [17].

- As we approach  $E_\nu \simeq \mathcal{O}(10\text{ GeV})$ , neutrinos can excite the struck nucleon to an excited state. In this case, the neutrino interaction produces a baryon resonance, which in most cases quickly decays to a nucleon and single pion final state, as illustrated in figure 1.2c, where the following resonance pion production process

is pictured

$$\nu_\ell + p \xrightarrow{\Delta^{++}} \ell^- + \pi^+ + p. \quad (1.5)$$

In addition to resonance production, neutrinos can also coherently produce single pion final states. In this case, the neutrino coherently scatters from the entire nucleus, transferring negligible energy to the target. These low- $Q^2$  interactions produce no nuclear recoil and a distinctly forward-scattered pion, compared to their resonance-mediated counterparts.

- When the neutrino energy exceeds 10 GeV, the interaction is entirely at the parton level [17], breaking the nucleons and producing a final state interaction with high multiplicity, i.e. a large number of final state particles,

$$\nu_\ell + N^{(0)} \rightarrow \ell^- + X^{(+)}, \quad \bar{\nu}_\ell + N^{(0)} \rightarrow \ell^+ + X^{(-)} \quad (1.6)$$

where  $X^{(\pm)}$  indicates the ensemble of the final state particles, with this notation highlighting that charge is still conserved, so an overall positive charge is expected. This kind of interaction is known as Deep Inelastic Scattering (DIS) [17]. This is exemplified in Figure 1.2e.

**Neutral current interactions** The possible interactions include neutral current topologies mediated by the exchange of a  $Z^0$  boson. Looking at the classification for CC events, we also have a similar classification for neutral current (NC) topologies.

- The lower part of the energy spectrum is populated by elastic scattering of neutrinos on nucleons, with each particle involved in the process not changing its nature,

$$\stackrel{(-)}{\nu_\ell} + N \rightarrow \ell^\pm + N, \quad \text{with } N = p, n. \quad (1.7)$$

One of these processes is presented in Figure 1.2b.

- NC Resonance (Res.) and Coherent (Coh.) single pion scattering processes are also possible, with a plethora of possible final state topologies; in Figure 1.2d as an example the single pion process mediated by the  $\Delta^+$  baryon is shown

$$\nu_\mu + p \xrightarrow{\Delta^+} \nu_\mu + \pi^+ + n. \quad (1.8)$$

- Finally, at high energy, the NC Deep Inelastic Scattering (DIS) processes are possible. Figure 1.2f shows an illustration of a DIS process,  $\nu_\mu + N^{(0)} \rightarrow \nu_\mu + Y^{(0)}$ .

The Gargamelle experiment [18] played a key role in the history of neutrino physics, being the first to actively detect signatures of neutral weak current events, thus confirming the validity of the weak interaction model [19, 20]. Full reviews of the neutrino interactions in matter (expanding more on the processes displayed in Figure 1.2) are found in Ref. [17, 21].

### 1.2.2. Flavour oscillations

Neutrinos are one of the most abundant “visible” particles in the universe. They are produced in multiple channels, many *natural*, some *artificial*. The production mechanism is correlated with their energy.

- Neutrinos in the MeV scale are generated in reactions inside the stars cores (such as the Sun) through the ppp-chain and the CNO cycle reactions [22];
- On the artificial side, neutrinos in the MeV region are those coming from nuclear fission reactors: electron antineutrinos originate as the  $\beta$ -decay products of unstable isotopes such as  $^{238}\text{U}$  and  $^{239}\text{Pu}$ . The energies peak at 3 MeV and extend up to 8 MeV [23];
- The central part of the energy spectrum, from some GeV to some TeV, is composed of atmospheric neutrinos, coming from cosmic rays interacting within the atmosphere. These also compose the highest part of the spectrum;
- In the core region, there are also accelerator-borne beams of neutrinos. These extend from some hundreds of MeV to some tens of GeV and constitute an interesting part of the spectrum: their power can be controlled, hence their flux, making it easier to study in greater detail the properties of neutrinos.

Up to this point, the description of neutrinos has been of massless neutral leptons. However, experimental observations suggested otherwise.

Dating back to the discovery of neutral mesons, the idea of flavour oscillation was established for massive particles. This was the case for the  $K^0/\bar{K}^0$  system oscillation, which was studied to get an explanation for the regeneration of short-lived neutral kaons,  $K_S^0$  [24]. This type of oscillatory behaviour is accurately explained by the weak interaction of quarks in the SM Lagrangian with the Higgs mechanism that gives masses to quarks themselves, hence to mesons.  $K^0/\bar{K}^0$  are both eigenstates of the weak interaction, which are different from the mass eigenstates that control the time evolution of the

particle. When looking at the time evolution of the eigenstate of the weak interaction, we get, thus, an oscillatory behaviour.

For neutrinos, based on experimental evidence, no flavour oscillation was expected. However, theoretical models of neutrino oscillation date back to the '60s. In 1957 Pontecorvo discussed  $\mu^+e^- \leftrightarrow \mu^-e^+$  [25], and proposed, with an analogy to the  $K^0/\bar{K}^0$  system, the oscillation of neutrinos. The two-flavour neutrino oscillation physics was worked out by Maki, Nakagawa and Sakata in 1962 [26]. In this model, the oscillation probability is found to be proportional to

$$P(\nu_\alpha \rightarrow \nu_\beta) = \sin^2(2\theta_{\alpha\beta}) \sin^2\left(\frac{\Delta m^2 E_\nu}{4L}\right), \quad (1.9)$$

where the probability of going from the flavour state  $\alpha$  to the flavour state  $\beta$  is dependent on the mixing angle  $\sin^2(2\theta)$ , the neutrino energy  $E_\nu$ , the neutrino flight length,  $L$  and the squared difference of the masses of the two neutrino flavours  $\Delta m^2 = m_\alpha^2 - m_\beta^2$ .

The first experimental evidence of neutrino oscillations came from the Homestake Mine solar neutrino experiment. Between the 1970s and 1990s this experiment, led by physicist R. Davis, used radiochemical technique to measure the flux of solar neutrinos [27].

Neutrinos from the Sun come from fusion reaction chains taking place inside the Sun's core. An energy spectrum of the neutrino flux is presented in Figure 1.3. The detection principle relied on the use of the capture process  $\nu_e + {}^{37}\text{Cl} \rightarrow {}^{37}\text{Ar} + e^-$ , with a threshold of 814 keV, making only  ${}^7\text{Be}$  and  ${}^8\text{B}$  flux detectable by the experiment. The produced  ${}^{37}\text{Ar}$  decayed with a half-life of 34.8 days and was measured by means of a proportional chamber. Despite the huge number of neutrinos from solar flux  $\sim 6 \times 10^{10} \text{ cm}^{-2} \text{ s}^{-1}$ , only 1.7 events were expected each day [29, 30]; however, the total flux collected by the Homestake Mine experiment amounted to an observed flux of  $0.48 \pm 0.04$  neutrino interactions per day [27]. To investigate the origin of this flux deficit, even in other components of the proton-proton (pp) and carbonnitrogenoxygen (CNO) processes in the Sun's core, multiple experiments were developed, with the aim of investigating the lower part of the energy spectrum. In particular, neutrinos from the pp chain are the most abundant, so they were targeted to clarify this problem. In order to measure this contribution, the threshold had to be lowered. The energy spectrum of the protons from the pp chain is, as pictured in Figure 1.3, lower than the minimum detectable energy of 814 keV, achieved with previous experiments. Using gallium, or gallium-doped targets, by means of the neutrino capture process  $\nu_e + {}^{71}\text{Ga} \rightarrow {}^{71}\text{Ge} + e^-$ , with a threshold

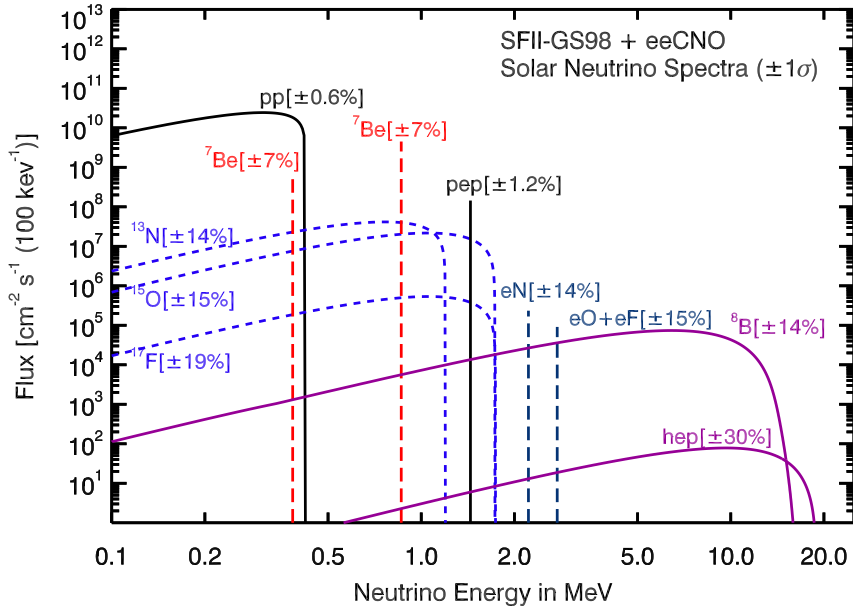


**Figure 1.3.** Solar neutrino flux produced by all the reactions inside the Sun’s core. Picture taken from [28].

energy of 233 keV it is possible to detect neutrinos from the pp chain. Four experiments followed this idea: the SAGE experiment at Baksan [31], using 50 t of liquid metallic gallium, and the GALLEX [32] experiment at *Laboratori Nazionali del Gran Sasso* (LNGS), using gallium chloride,  $\text{GaCl}_3$ , followed by the GNO experiment; their data were used for a combined analysis [32, 33]. These results highlighted that also for this lower region of the energy spectrum the model was inconsistent with the data. The same was shown by the results from the SAGE collaboration [31]. This set of anomalous measurements is referred to as the “solar neutrino problem”.

The landscape evolved in 1998 with the observation of atmospheric neutrinos by the Kamiokande and Super-Kamiokande experiments. While the radiochemical detectors measure the reaction rate integrated between extractions, the real-time measurement of solar neutrinos was possible with this type of detector. The Kamiokande detector was a 3000 t water-Cherenkov detector in the Kamioka mine. Super-Kamiokande (SK), the successor of Kamiokande, started operation in 1996. It is a large upright cylindrical water Cherenkov detector containing 50 kt of pure water. An inner volume of 32 kt of water

was surrounded by 11 000 photomultiplier tubes (PMT), detecting the Cherenkov radiation from the particles inside the volume. Both Kamiokande and Super-Kamiokande can detect solar neutrinos using neutrino-electron elastic scattering (ES),  $\nu_\ell e^- \rightarrow \nu_\ell e^-$ . The results of Kamiokande and SK for  $\nu_e$  ES events still showed a decrease of the observed flux [34]

$$(2.308 \pm 0.020 \text{ (stat.)}^{+0.039}_{-0.040} \text{ (syst.)}) \times 10^6 \text{ cm}^{-2} \text{ s}^{-1},$$

with respect to the expected flux of  $(5.46 \pm 0.66) \text{ cm}^{-2} \text{ s}^{-1}$ .

The Kamioka water Cherenkov detector, as well as the Irvine-Michigan-Brookhaven (IMB) water Cherenkov detector, was also able to detect, other than electrons and electron neutrinos coming from the Sun's core, muons and muon neutrinos. These contributions are predicted to be originating in Earth's atmosphere as a result of the interaction of primary cosmic rays. Both the Kamioka and the IMB experiments observed a deficit [35, 36] of neutrinos from what was expected. These anomalous measurements, among others, constitute the “atmospheric neutrino problem” [37]. Atmospheric neutrinos come from interactions between cosmic rays and nuclei in the atmosphere, leading to the production of charged mesons, which then decay. One of the leading channels of this chain is the pion decay,  $\pi^\pm \rightarrow \mu^\pm + \bar{\nu}_\mu^{(-)}$ , and the subsequent muon decay,  $\mu^\pm \rightarrow e^\pm + \bar{\nu}_\mu^{(-)} + \bar{\nu}_e^{(-)}$ , implying a flavour ratio  $(\nu_\mu + \bar{\nu}_\mu)/(\nu_e + \bar{\nu}_e) = 1/2$ . Both Kamiokande experiment as well as the IMB experiment measured the flavour ratio, loosely referred to as  $(\mu/e)_{\text{obs}}$ , which, compared to the theory calculation  $(\mu/e)_{\text{theory}}$ , yields the double ratio  $R$  [37]

$$\begin{aligned} R &= (\mu/e)_{\text{obs}} / (\mu/e)_{\text{theory}} = 0.57^{+0.08}_{-0.07} \text{ (stat.)} \pm 0.07 \text{ (syst.)} && \text{(Kamioka)} \\ &R = 0.54 \pm 0.02 \text{ (stat.)} \pm 0.07 \text{ (syst.)} && \text{(IMB-3)} \end{aligned} \quad (1.10)$$

The solution for this “atmospheric neutrino problem” came indeed from the analysis of SK atmospheric data, by following the hypothesis that neutrinos do oscillate, and hence that a deficit of muon neutrinos had to be found as an increase in the population of electron and tau neutrinos. The data collected by SK showed a good agreement for atmospheric neutrinos assuming a two-flavour oscillation [38], with  $\sin^2(2\theta) > 0.90$  and  $1.9 \times 10^{-3} \text{ eV}^2 < \Delta m^2 < 3 \times 10^{-3} \text{ eV}^2$  at 90 % confidence level. The confirmation of this result came from subsequent experimental efforts, especially from the OPERA experiment operating at the Laboratori Nazionali del Gran Sasso (LNGS), detecting neutrinos from the CERN Neutrinos to Gran Sasso (CNGS) beam — the experiment did, in fact, detect tau neutrinos [39] from the CNGS  $\nu_\mu$ -disappearance.

The solution for the “solar neutrino problem” came in the early 2000s, with the experimental results from the Sudbury Neutrino Observatory (SNO) [40]. The detector consisted of 1000 t of heavy water, D<sub>2</sub>O, contained in a spherical vessel surrounded by a H<sub>2</sub>O shield. An array of PMTs measured at the Cherenkov radiation produced in both D<sub>2</sub>O and H<sub>2</sub>O. This allowed the measurements of multiple signatures of <sup>8</sup>B neutrinos from the Sun’s core: in addition to ES scattering in water, heavy water allowed for the detection of other interaction channels, including CC scattering off of deuterium  $\nu_e + d \rightarrow e^- + p + p$ , and NC interaction  $\nu_\ell + d \rightarrow \nu_\ell + n + p$ , and includes equally all neutrino flavours. Therefore, the comparison of the three fluxes (ES, CC and NC), each sensible to one or more neutrino flavours, allowed scientists to measure the full neutrino solar flux. The results of the SNO collaboration, combined with the ES events collected by SK, allowed the extraction of the full flux of neutrinos from the Sun, highlighting that flavour conversion happened also for neutrinos [40–42]. The mass splitting reported by the SAGE [43] and GALLEX+GNO [44] experiments was of the order of  $\Delta m^2 \sim 10^{-5}$  eV<sup>2</sup>, with the oscillation amplitude  $\sin^2(2\theta) \sim 0.3$ .

### Flavour oscillation formalism

In the Standard Model of particle physics, flavour oscillation, as already mentioned, is a consequence of the fact that particles must have non-zero masses. This is the case for the hadronic sector, where flavour oscillation is regulated via the  $V_{CKM}$  matrix, which arises from the request that the mass matrix for quarks is indeed diagonal [13].

In the minimal SM, neutrinos are massless, and this allows their mass eigenstates to be the same as their flavour eigenstates. Flavour eigenstates are the ones involved in interactions and determine the interaction topology that can be detected. The fact that, in the minimal SM with massless neutrinos, flavour and mass eigenstates are equivalent leads to flavour not changing as neutrinos propagate through space and time.

As evidenced by multiple experiments in the previous sections, however, neutrinos display a very different behaviour to that predicted by the minimal SM. The observations presented before, however, do fit coherently within the framework of flavour oscillation. This framework, developed by analogy to that of flavour oscillation in the quark sector, implies that neutrinos, like quarks, must have mass. The mixing between mass and flavour eigenstates is steered by the Pontecorvo-Maki-Nakagawa-Sakata (PMNS) mixing matrix. We can define a flavour basis of eigenstates,  $\nu_\alpha = (\nu_e, \nu_\mu, \nu_\tau)$  and a mass basis of eigenstates,  $\nu_i = (\nu_1, \nu_2, \nu_3)$ . The flavour eigenstate basis of neutrinos is that

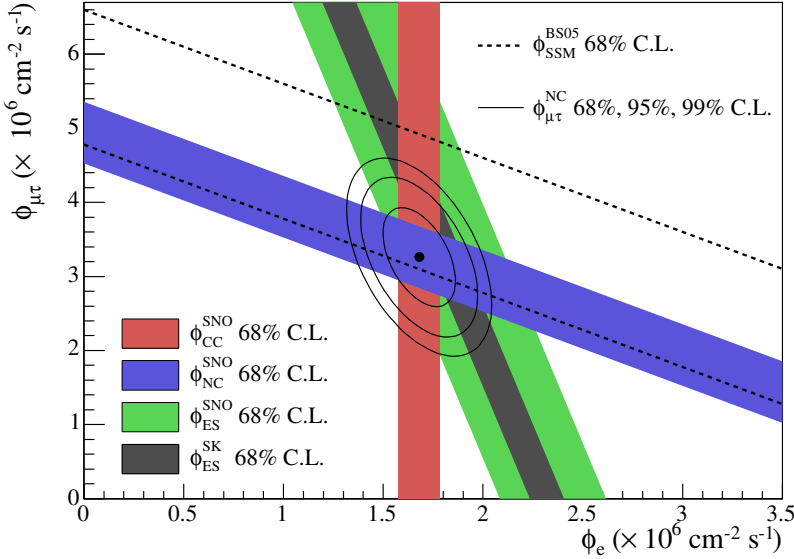


**Figure 1.4.** Fluxes of  ${}^8\text{B}$  solar neutrinos,  $\phi(\nu_e)$ , and  $\phi(\nu_{\mu,\tau})$ , deduced from the SNO CC, ES, and NC measurements. The standard solar model prediction [29, 30] is also shown. The bands represent the  $\pm 1\sigma$  region centred around the best fit. The contours show the 68 %, 95 %, and 99 % CL best-fit regions for the  $\phi(\nu_e)$  and  $\phi(\nu_{\mu,\tau})$  experimental results. Figure from [45].

which undergoes weak interaction; on the other hand, the mass eigenstate basis is that which undergoes time transformation, and the masses are their eigenvalues, dictating how each eigenstate evolves through time. We can express each base as a rotation of the other, using the complex-valued Pontecorvo-Maki-Nakagawa-Sakata (PMNS) matrix,

$$|\nu_\alpha\rangle = \sum_{i=1}^3 U_{\text{PMNS}, \alpha i}^* |\nu_i\rangle, \quad |\nu_i\rangle = \sum_{\alpha=1}^3 U_{\text{PMNS}, \alpha i} |\nu_\alpha\rangle, \quad (1.11)$$

where the Greek indices indicate the flavour eigenstate basis, and the Roman ones indicate the mass eigenstate basis.

The complex-valued  $U_{\text{PMNS}}$  matrix can be expressed as the product of three rotations

and a complex phase

$$U_{\text{PMNS}} = \begin{pmatrix} 1 & 0 & 0 \\ 0 & \cos \theta_{23} & \sin \theta_{23} \\ 0 & -\sin \theta_{23} & \cos \theta_{23} \end{pmatrix} \times \begin{pmatrix} \cos \theta_{13} & 0 & \sin \theta_{13} e^{-i\delta} \\ 0 & 1 & 0 \\ -\sin \theta_{23} e^{i\delta} & 0 & \cos \theta_{23} \end{pmatrix} \times \begin{pmatrix} \cos \theta_{12} & \sin \theta_{12} & 0 \\ -\sin \theta_{12} & \cos \theta_{12} & 0 \\ 0 & 0 & 1 \end{pmatrix} \quad (1.12)$$

where  $\theta_{ij}$  are the rotation angles, and  $\delta$  is the Charge-Parity (CP) violating phase, often referred to as  $\delta_{\text{CP}}$ . The theory, in the case neutrinos were Majorana particles, would require two additional phases,  $\alpha_1$  and  $\alpha_2$  [46]. This is obtained by multiplying the PMNS matrix by the term

$$\text{diag}\left(e^{i\alpha_1/2}, e^{i\alpha_2/2}, 1\right). \quad (1.13)$$

Given the rotations in (1.11), neutrino oscillations arise from the time evolution of the massive eigenstates  $\nu_i$ , in vacuum [46]

$$|\nu_i, t\rangle = e^{-ip \cdot x} |\nu_i, t=0\rangle = e^{-iE t + \mathbf{p} \cdot \mathbf{x}} |\nu_i, t=0\rangle. \quad (1.14)$$

Combining (1.11) and (1.14) leads the flavour basis to oscillate as the mass eigenstates evolve in time (hereafter,  $|\nu_i\rangle = |\nu_i, t=0\rangle$  and the same holds for the flavour eigenstates).

$$|\nu_\alpha, t\rangle = \sum_i U_{\alpha i}^* e^{-iE t + \mathbf{p} \cdot \mathbf{x}} |\nu_i\rangle = \sum_\beta \left( \sum_i U_{\alpha i}^* e^{-iE t + \mathbf{p} \cdot \mathbf{x}} U_{\beta i} \right) |\nu_\beta\rangle. \quad (1.15)$$

The probability of evolving from the initial state  $\alpha$  to the final state  $\beta$  at a given time  $t$  is thus given by

$$\begin{aligned} P(\nu_\alpha \rightarrow \nu_\beta) &= \left| \langle \nu_\beta | \nu_\alpha, t \rangle \right|^2 = \left| \sum_i \sum_j U_{\alpha i}^* U_{\beta j} \langle \nu_j | \nu_i, t \rangle \right|^2 = \\ &= \delta_{\alpha\beta} - 4 \sum_{i < j} \text{Re}[U_{\alpha i} U_{\beta i}^* U_{\alpha j}^* U_{\beta j}] \sin^2 \left( 1.26 \frac{\Delta m_{ij}^2}{\text{eV}^2} \frac{L/E}{\text{m/MeV}} \right) + \\ &\quad + 2 \sum_{i < j} \text{Im}[U_{\alpha i} U_{\beta i}^* U_{\alpha j}^* U_{\beta j}] \sin \left( 2 \times 1.26 \frac{\Delta m_{ij}^2}{\text{eV}^2} \frac{L/E}{\text{m/MeV}} \right). \end{aligned} \quad (1.16)$$

under the assumptions that, for  $m_i \ll p_i$ , since  $E_i = \sqrt{p_i^2 + m_i^2}$  in the relativistic limit,

$|\mathbf{p}_i|$  tends to  $E_i$ , and also

$$E = \sqrt{p_i^2 + m_i^2} \simeq p_i + \frac{m_i^2}{2p_i} \simeq p_i + \frac{m_i^2}{2E}.$$

In Eq. (1.16)  $L$  is the distance from the neutrino source to the point where neutrinos do interact (i.e. the detector), and  $E$  is the neutrino energy. It is important to highlight — especially for reasons that will be clarified in the following (see section 1.3) — that no hypothesis about the number of neutrinos has been made to obtain such oscillation probability. Thus, equation (1.16) is valid for any number  $N$  of neutrino families, as long as the mixing PMNS matrix is  $N \times N$ .

Looking closely at the contributions of Eq. (1.16), we highlight three components. The first term,  $\delta_{\alpha\beta}$ , correspond to the unoscillated case and is particularly important in disappearance studies. The second term, proportional to the real part of  $U_{\alpha i} U_{\beta i}^* U_{\alpha j}^* U_{\beta j}$  depends on the mixing angles but is not sensible to the  $\delta_{CP}$  CP-violating complex phase. The CP-violation in the leptonic sector can be probed by exploiting the second term, proportional to the imaginary part. This changes sign between particles and antiparticles, so by comparing the two cases (particle and antiparticle), it is possible to measure  $\delta_{CP}$ .

Finally, some additional remarks are necessary about Eq. (1.16). The first remark is regarding the Majorana phases, introduced briefly after Eq. (1.12). As it is clear, if we further develop the related math of Eq. (1.16), the  $N$ -flavour oscillation is not sensitive to the Majorana phases, for which a different type of search is required: this is still strictly related to the problem of neutrino masses and also to the CP violation problem [47, 48], but not dealt with in this thesis.

A second remark is that the oscillation probability that appears in Eq. (1.16) is valid only for neutrinos propagating through vacuum space. In the case of propagation through matter, it is important to consider how the interaction with electrons acts on the propagation. This effect was first hypothesised by Mikheyev-Smirnov-Wolfenstein, hence the name MSW effect, and later confirmed by the KamLAND experiment [49]. Briefly, starting from the hypothesis that neutrinos in matter interact coherently, the MSW effect shows how the difference between the electron neutrino flavour — which can interact both through CC and NC coherent scatter with the nuclei —, and the muon/tau neutrino flavours — interacting only through NC coherent scattering — results in a difference in their oscillation probability [50–52]. The MSW effect and its experimental confirmations by the KamLAND experiment allow the knowledge of the sign of the mass splitting measured in solar neutrinos. This effect, while not relevant for short baseline experiments such as the SBN programme, is instead crucial for long baseline experiments, like

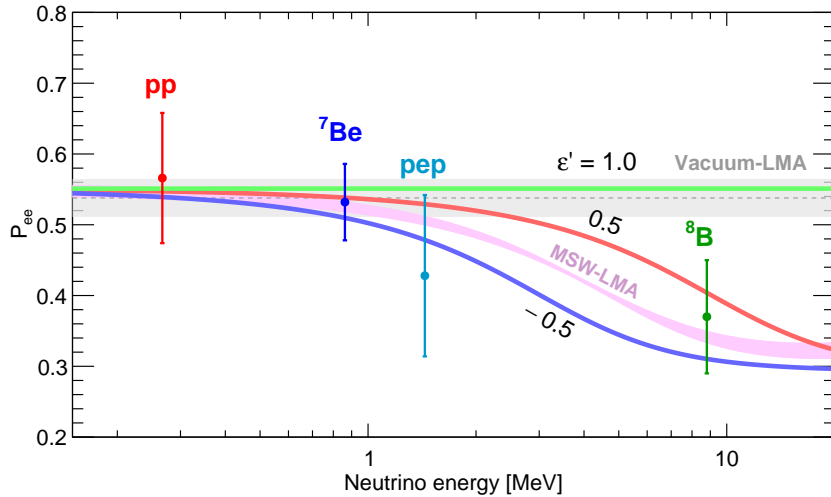


**Figure 1.5.** Effect of the MSW matter effect on solar neutrino oscillations, comparing the data with the vacuum-oscillated model and the MSW model. Picture taken from [54].

the Deep Underground Neutrino Experiment [53], and for solar neutrino experiments, which have to take into account how the oscillation probability changes as neutrinos produced in its core cross the Sun. Figure 1.5 shows the effects of matter oscillations for solar neutrinos, comparing the vacuum-oscillation model with the MSW effect, which does fit better with the data.

The final remark is about the experimental values of the mass splitting. With the current status of neutrino oscillation experiments, we have identified the absolute value of two mass splitting terms: one coming from the best fit of atmospheric neutrino oscillations ( $\nu_\mu \leftrightarrow \nu_\tau$  oscillations), which is regarded as  $|\Delta m_{\text{Atmospheric}}^2|$ , and the other from the best fit of solar neutrino oscillations (mainly  $\nu_e \leftrightarrow \nu_\mu$  oscillations), which is known as  $\Delta m_{\text{Solar}}^2$ . The peculiarity is that these values show two orders of magnitude of difference, i.e.

$$|\Delta m_{\text{Atmospheric}}^2| \simeq 10^{-3} \text{ eV}^2 \gg \Delta m_{\text{Solar}}^2 \simeq 10^{-5} \text{ eV}^2. \quad (1.17)$$

Since we cannot know, for the atmospheric oscillations, the sign of the mass splitting, there are two possible scenarios. The first, called normal ordering or normal hierarchy (NO/NH), assumes a positive sign for both, and so  $m_1 < m_2 < m_3$ . The alternative assumes a negative sign for the atmospheric mass splitting, and thus  $m_3 < m_1 < m_2$ . Figure 1.6 shows an illustration of both NO (left) and IO (right). This great difference

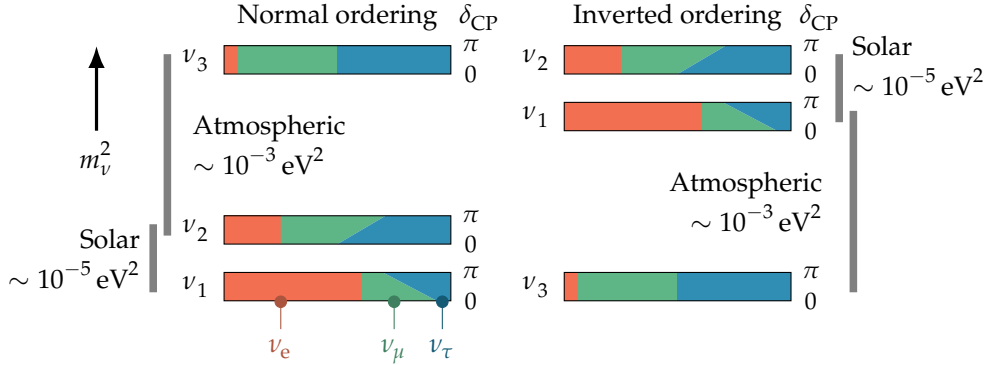


**Figure 1.6.** The two scenarios for neutrino mass ordering: the normal ordering (NO), on the left, and the inverted ordering (IO), on the right. The shaded area represents the mixing angles, or the fraction of each flavour contained in the mass eigenstates. Additionally, the dependence on the CP-violating phase effect is shown, with its value ranging from 0 to  $\pi$ . Figure adapted from [55].

between the two mass splitting values, shown in Eq. (1.17), can be exploited to simplify the experimental observations. By choosing accordingly both the neutrino energy and the baseline at which neutrinos are detected from their sources, many experiments can simplify the oscillation description and assume a two-neutrino oscillation framework.

### Present status

In order to assess the entity of neutrino oscillations, we need to measure the parameters of the PMNS matrix. As we can read from Eq. (1.12), it depends on three angles and a complex phase, so, in order to measure it correctly, multiple experimental measurements must be carried out. Additionally, one aims at knowing the precise value of the mass splittings. Each parameter can be accessed by exploiting different neutrino sources in order to vary the baseline and the energy or the  $L/E$  ratio of the measured interaction to pinpoint each parameter in the phase space. Additionally, oscillation measurements are classified either as “appearance” experiments, where the oscillation from a given flavour  $\alpha$  to another  $\beta$  is measured, or as “disappearance” measurements, where the probability  $P(\nu_\alpha \rightarrow \nu_\alpha) = 1 - \sum_{\beta \neq \alpha} P(\nu_\alpha \rightarrow \nu_\beta)$  of getting the same flavour at different distances from the sources is tested.

The distance of the detector from the experimental source is usually selected to max-

imise the sensitivity to a precise mass splitting,  $\Delta m^2 \sim E/L$ .

Recently, the precision with which these parameters are determined reached a percent value, allowing neutrino oscillation physics to move from the “discovery” to the “precision” era.

**Solar neutrino observations** Solar neutrinos were the first probe for neutrino oscillations and still are an interesting source with multiple search channels for both neutrino oscillations as well as precise measurements of the multiple components of the solar neutrino energy flux, shown in [Figure 1.3](#), down to a precision ranging from 2 to 15 % in all major channels (pp, CNO,  ${}^7\text{Be}$ ) [56, 57], with the only exception of the hep  ${}^3\text{He} + \text{p} \rightarrow {}^4\text{He} + \text{e}^+ + \nu_e$  process, which is expected to be studied by the JUNO detector with increased sensitivity [58]. Given that the energy range for solar neutrinos is  $233\text{ keV} \leq E_\nu \lesssim \text{MeV}$ , and the baseline  $L$  corresponding to the distance between the Sun and Earth, the  $E/L$  ratio allows the measurement of  $\Delta m_{\text{Solar}}^2 \sim 10^{-5}\text{ eV}^2$ . This implies that the measured neutrino flux can be described assuming a two-state mixing scheme and thus  $\sin^2 2\theta_{12}$  can be measured. Precise measurements are the result of multiple years of observations from multiple detectors, leading to an allowed region at  $3\sigma$  for the oscillation parameters  $\Delta m_{21}^2$  from  $6.92 \times 10^{-5}$  to  $8.05 \times 10^{-5}\text{ eV}^2$  and  $\sin^2 \theta_{12}$  from 0.275 to 0.345. These results are the combination of measurements from the Soviet-American Gallium Experiment (SAGE) [43], the GALLium EXperiment (GALLEX), the Gallium Neutrino Observatory (GNO) [44], the Kamiokande and SK experiments [59], the BOREXINO experiment [22] and the Kamioka Liquid scintillator ANtineutrino Detector (KamLAND) experiment [60].

**Atmospheric neutrinos** The  $L/E$  ratio for neutrinos, with an energy spectrum from 0.1 GeV to 10 TeV, and detected at baselines compatible with the thickness of the atmosphere from 15 to 12 700 km, generated mostly by pion decays in the atmosphere allows exploring the  $\nu_\mu \leftrightarrow \nu_\tau$  oscillation phase space that is characterised by a mass splitting  $|\Delta m_{32}^2| = |\Delta m_{\text{Atmospheric}}^2| \sim 10^{-3}\text{ eV}^2$ , and so allows for the determination of  $\sin \theta_{23}$ . Atmospheric neutrino oscillations have been studied by the Kamiokande experiment [35] and its successor, Super-Kamiokande [38], by the MACRO experiment [61], and also by neutrino telescopes, such as the ANTARES experiment and the IceCube experiment. Novel experiments will join this research, such as the KM3NeT-ORCA telescope, the successor of the ANTARES experiment, the Hyper-Kamiokande experiment, the JUNO experiment, and the DUNE experiment.

**Accelerator neutrinos** A phase space similar to that of atmospheric neutrino oscillations can be explored by the accelerator neutrino experiments, especially at long baselines. Conventional neutrino beams from accelerators are produced by colliding high-energy particles onto a target — usually p on a  ${}^7\text{Be}$  target — thereby producing  $\pi$  and K, which then decay into neutrinos. The branching ratio of  $\pi^+ \rightarrow \mu^+ \nu_\mu$  is  $\sim 100\%$ , and a minimal beam contamination from  $\nu_e/\bar{\nu}_e$  (less than 0.5% in the Booster Neutrino Beam operating at Fermilab, and similar  $< 1\%$  was also obtained by the CNGS beam) comes from kaon decays. The values of neutrino energy and baseline are chosen to maximise the oscillation probability, either for studying the atmospheric mass splitting  $|\Delta m_{21}^2| \simeq 2.5 \times 10^{-3} \text{ eV}^2$ , with the first oscillation maximum at  $L/E \simeq 500 \text{ GeV/km}$ , or for testing the  $\Delta m^2 \sim 1 \text{ eV}^2$  splitting at  $\sim 1 \text{ km}$  baselines.

The present landscape of the accelerator neutrino experiments is vast, from the first experiments being the K2K and MINOS experiments — exploring the values of  $\Delta m_{31}^2$  and  $\Delta m_{32}^2$ , by studying the  $\nu_\mu$ -disappearance channel — to their successors, the T2K experiment, building upon the K2K experiment, employing Super-Kamiokande as its far detector at 295 km, and the NOvA experiment, collecting neutrinos from the Neutrino at the Main Injector (NuMI) beam at a baseline of 810 km. Both T2K and NOvA measured  $\Delta m_{31}^2$ ,  $\Delta m_{32}^2$ , and  $\sin \theta_{23}$  by measuring both the  $\nu_e$ -appearance and  $\nu_\mu$ -disappearance channels from a pure  $\nu_\mu$  beam [62–64]. Additionally, both experiments performed a measurement of the  $\delta_{\text{CP}}$  violating phase of the PMNS matrix. The T2K experimental results showed a preference towards  $\delta_{\text{CP}} \sim \pi/2$  [63], whereas the NOvA data showed a preference towards  $\delta_{\text{CP}} \sim 3\pi/2$  [64].

**Reactor antineutrinos** Nuclear fission reactors give a substantial flux of electron antineutrinos in the MeV region, through  $\beta$ -decay of radioactive isotopes created during the fission process, primarily  ${}^{235}\text{U}$ ,  ${}^{238}\text{U}$ ,  ${}^{239}\text{Pu}$ , and  ${}^{241}\text{Pu}$ ;  $\bar{\nu}_e$  are then detected at different baselines  $\sim 1 \text{ km}$ . Charged current events cannot happen, given the available phase space, for  $\bar{\nu}_\mu$  or  $\bar{\nu}_\tau$  since they require more energy to produce  $\mu$  or  $\tau$  in the final state than what is accessible, so flavour oscillation for such experiments is only accessible through the  $\bar{\nu}_e$ -disappearance channel. The detection mechanism relies on the inverse beta decay  $p + \bar{\nu}_e \rightarrow e^+ + n$ , where the signal from the prompt  $e^+$  and the delayed  $\gamma$  (with the energy depending on the type of scintillator; 2.2 MeV for hydrogen, 8 MeV when it is loaded with gallium) from the thermalisation of the neutron helps separate it from the background.

The Kamioka Liquid scintillator ANtineutrino Detector (KamLAND) experiment was

a pioneer experiment, measured neutrinos from multiple nuclear reactors at  $\sim 180$  km from the source, observing a ratio of inverse  $\beta$  decay over the predicted flux of

$$0.611 \pm 0.085 \text{ (stat.)} \pm 0.041 \text{ (syst.)}, \quad (1.18)$$

showing evidence for  $\bar{\nu}_e$ -disappearance at 99.95 % confidence level [49].

Reactor antineutrino experiments also showed very high sensitivity to the  $\theta_{13}$  mixing angle. This is possible in the case of a short baseline  $\sim 1$  km, as in the case of the Double Chooz experiment [65], the Daya Bay experiment [66], and the RENO experiment [67], which found, respectively,

$$\begin{aligned} \sin^2 2\theta_{13} &= 0.086 \pm 0.041 \text{ (stat.)} \pm 0.030 \text{ (syst.)}, \\ &\text{or } 0.017 < \sin^2 2\theta_{13} < 0.16 \text{ at 90 \% CL} \end{aligned} \quad (\text{Double Chooz}) \quad (1.19)$$

$$\sin^2 2\theta_{13} = 0.092 \pm 0.016 \text{ (stat.)} \pm 0.005 \text{ (syst.)} \quad (\text{Daya Bay}) \quad (1.20)$$

$$\sin^2 2\theta_{13} = 0.113 \pm 0.013 \text{ (stat.)} \pm 0.019 \text{ (syst.)} \quad (\text{RENO}) \quad (1.21)$$

### 1.3. Short baseline anomalies

It is clear at this point that the three-state mixing scheme of neutrino flavour oscillation is well established, from the empirical point of view, leading to the clear necessity of a “minimal” extension of the standard model in order to introduce neutrino masses. Since the mass and size of neutrinos is very different from other particles of the standard model, generating their masses would require a novel mechanism. Multiple beyond SM physics (BSM) models have been developed [48, 68], all requiring the addition of particle content to the SM; however, in spite of the well established evidence for neutrino masses, no direct measurement has been made to date, and no model is currently preferred over the others [48].

In addition to these open questions, in the past twenty years the picture has been complicated by some anomalous observations. Multiple short-baseline experiments, operating at a baseline  $L$  with neutrino energy  $E$  such that  $L/E \sim \mathcal{O}(10 \text{ m/MeV})$ , observed either a deficit or an excess of events of neutrino interactions in multiple channels and with different neutrino sources [69]. The combination of these anomalies at short baselines of  $\sim 1$  km hints at the existence of a fourth neutrino flavour with a mass splitting  $\Delta m^2 \sim 1 \text{ eV}$ . This, combined with the fact that only three “active” (i.e. interacting) families of neutrinos are compatible with all the experimental results so far [11], lead to the

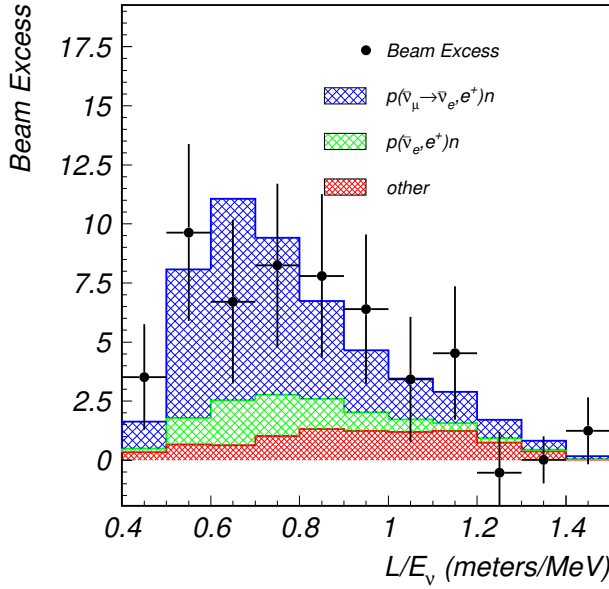


**Figure 1.7.** LSND anomalous events as a function of  $L/E_\nu$  for a subset of total events. The red and green shaded areas account for the the different parts of the beam flux, whereas the back dots show the overlayed data. The blue area shows the best fit under the hypothesis of a sterile-state mediated oscillation. More information can be found in Ref. [70], from which the figure was taken.

“sterile” neutrino hypothesis, i.e. a neutrino singlet in the SM that does not undergo weak interaction and is subject only to gravitational force. Here a more detailed picture of the different short baseline anomalies recorded is presented.

**Pion decay-at-rest accelerator experiments** Pion decay-at-rest generate a very pure muon antineutrino flux with a mean energy of  $E_{\bar{\nu}} \simeq 30$  MeV. As such, a detector placed at a relatively short baseline  $\sim 30$  m from the source is sensitive to oscillation with a mass splitting  $\sim 1$  eV<sup>2</sup>. Two major experiments employed this technology to produce neutrino beams, the LSND (Liquid Scintillator Neutrino Detector) and the KARMEN (KArlsruhe Rutherford Medium Energy Neutrino) experiments. Of the two, LSND had the highest sensitivity and observed the “LNSD anomaly”. The KARMEN experiment saw no evi-

dence of such an anomaly, and it is thus considered a “null” experiment for the sterile neutrino framework [71].

The LSND experiment at Los Alamos Laboratories measured  $\bar{\nu}_e$  produced by the oscillation of a  $\bar{\nu}_\mu$  beam using a liquid scintillator and observed an excess (shown in Figure 1.7) of electron antineutrinos, with a  $3.8\sigma$  tension from the three-flavour mixing scenario [70]. The LSND experiment consisted of a cylindrical tank of 8.3 m of height and a diameter of 5.7 m, placed horizontally, filled with 167 metric tons of mineral oil. LNSD detected electron antineutrinos from a beam of muon antineutrinos, produced by pions decaying at rest (DAR). The pions were produced by protons with  $E_p \simeq 798$  MeV hitting a water target that produced stopped pions. The signal selection relied on the measurement of both the scintillation light and the Cherenkov light cone produced by the positron (see figure 1.8a for a schematic illustration) correlated with a delayed 2.2 MeV photon signal produced by neutron capture. Scintillation and Cherenkov light were collected by means of 1220 PMTs. The LNSD data showed an excess of events of  $87.9 \pm 22.4$  (stat.)  $\pm 6.0$  (syst.), compatible with the hypothesis of a two-flavour oscillation  $\bar{\nu}_\mu \rightarrow \bar{\nu}_e$ . The fit pointed toward an oscillation amplitude of  $\sin^2 2\theta_{\mu e} \simeq 0.003$  and a mass splitting of  $\Delta m^2 \simeq 1.2$  eV $^2$ , resulting in the allowed regions at 90 % CL and 99 % CL shown in figure 1.8b [70].

**Pion decay-in-flight accelerator experiments** LNSD’s evidence for this oscillation prompted subsequent searches. This is why pion decay-in-flight (DIF) was selected as a valid production mechanism: it produces a pure  $\nu_\mu^{(-)}$  beam with higher energy, providing the opportunity for an independent test at a higher baseline. This was accomplished using the Booster Neutrino Beam (BNB), providing a 99.5 % pure muon neutrino beam with a mean energy of  $\sim 700$  MeV, in conjunction with the MiniBooNE Cherenkov detector at the Fermi National Accelerator Laboratories (Fermilab) in Illinois. The design of this experiment was adjusted to allow the phase space to align with that of the LNSD experiment:  $E/L \sim 30$  MeV/30 m for the LNSD experiment, so the same was accomplished by placing the MiniBooNE detector at 540 m. The MiniBooNE detector consisted of a single tank containing 818 t of mineral oil. The detection technique was based on the measurement of Cherenkov radiation that was possible thanks to 1520 PMTs located inside the detector tank. The Cherenkov light cone was used to separate between  $\nu_e$  CC and  $\nu_\mu$  CC events; the purity of the present selection was undermined by the presence of backgrounds coming mainly from NC interactions inside the tank and NC  $\pi^0$  interactions where one photon from the  $\pi^0$  decay is lost. The MiniBooNE experiment took data

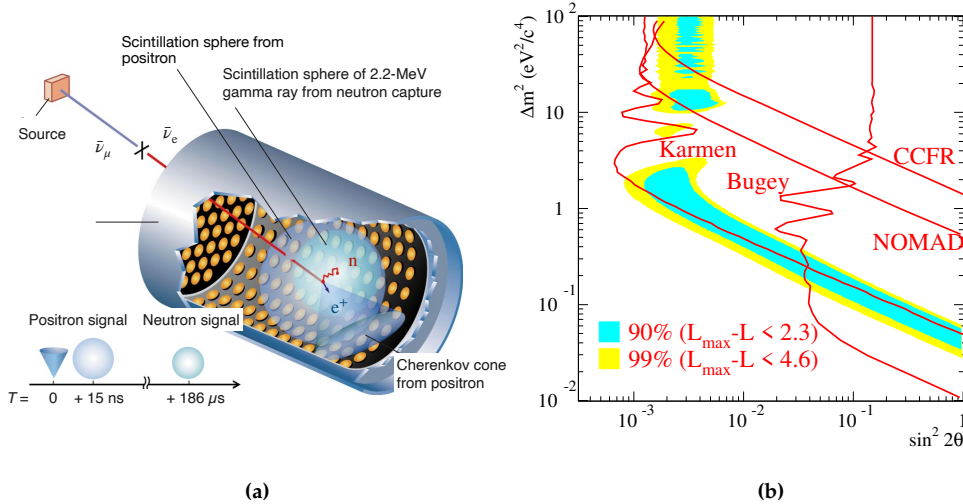


**Figure 1.8.** (a) Illustration of the LNSD detector at the Los Alamos Laboratories. In the illustration a typical electron antineutrino interaction is displayed, with both the prompt scintillation light and Cherenkov cone from the positron, as well as the light emitted by the subsequent neutron capture. Figure adapted from [72]. (b) Allowed regions from the LNSD fit to the sterile neutrino hypothesis in the oscillation parameter phase space. Figure taken from [70]

from 2002 to 2019, collecting a total of  $18.75 \times 10^{20}$  POT (protons-on-target) interactions with both a neutrino mode and an antineutrino mode, showing an excess of events in the signal region  $200 \text{ MeV} < E_\nu^{\text{QE}} < 475 \text{ MeV}$ , with a statistical significance of  $4.8\sigma$  [73]. This excess is known by the name of Low Energy Excess, LEE, and is shown in Figure 1.9.

**Reactor antineutrino experiments** Reactor antineutrinos played a central role in establishing the three-flavour oscillation paradigm. In the simplest sterile neutrino picture (more details are provided in subsection 1.3.1) where one additional sterile neutrino is assumed (3 + 1 scheme),  $\nu_e$  disappearance in neutrinos from reactors should be possible, with detectors placed  $< 100 \text{ m}$  from the neutrino source. In such experiments, respectively located at ILL-Grenoble, Goesgen, Rovno, Krasnoyarsk, Savannah River and Bugey [74], the measured rate of  $\nu_e$  was in reasonable agreement with that pre-

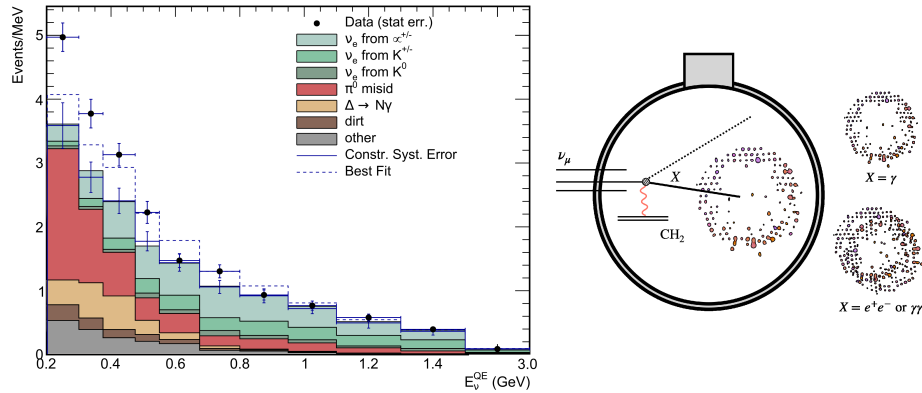


**Figure 1.9.** (left) Neutrino energy distribution of  $\nu_e$  CC QE events recorded by the Mini-BooNE detector with data acquisition in neutrino mode. The dashed histogram shows the best fit to the neutrino-mode data assuming two-neutrino oscillations. (right) An example of the typical interactions visible inside the detector, with different signatures for different final state interactions.

dicted from the reactor antineutrino spectra, though slightly lower than expected, with the measured/expected ratio at  $R = 0.976 \pm 0.024$ , representing a  $2.7\sigma$  deviation from the prediction. This is known as the “reactor antineutrino anomaly” (RAA). The additional measurements by the long-baseline detectors KamLAND and CHOOZ (the CHOOZ experiment is consistent with no oscillation) provided a stricter lower result of such ratio, at  $R = 0.943 \pm 0.023$ , deviating from the unity with a statistical significance of 98.6 % CL.

**Radioactive sources experiments** Radioactive sources are often used for the calibration of different types of detectors. This was the case for both the GALLEX and SAGE solar neutrinos detectors. Such experiments employed natural radioactive sources, either  $^{51}\text{Cr}$  or  $^{37}\text{Ar}$ , which both produce electron neutrinos through electron capture processes



placed inside the detector, to calibrate the flux of electron neutrinos with respect to the rate of electron capture processes  $\nu_e + {}^{71}\text{Ga} \rightarrow {}^{71}\text{Ge} + \text{e}^-$  observed. Both experiments, during the detector calibration, observed a deficit of counts with respect to

the well-known activities of the sources, with average ratios  $\bar{R}$  ranging from  $0.703 \pm 0.078$  to  $0.844 \pm 0.031$  [75], showing a statistical significance of  $2.2\sigma$ . A dedicated experiment was later planned, the Baksan Experiment on Sterile Transitions (BEST) to test such results, and a larger deficit was observed. Combining all radiochemical measurements increased significance of the so-called “Gallium Anomaly” (GA) to  $\sim 4\sigma$ , with  $\bar{R} = 0.80 \pm 0.04$  [76].

### 1.3.1. The sterile neutrino hypothesis

The picture presented so far seems to hint, from multiple perspectives, at the possibility of an additional sterile neutrino scenario. This requires the introduction of a fourth sterile — i.e. not weakly interacting — neutrino state, taking part in short baseline oscillation, with a mass splitting of  $\Delta m^2 \sim \mathcal{O}(1 \text{ eV}^2)$ . The need for this state to be “sterile” is required to minimally extend the SM, since the introduction of a massive weakly interacting particle with  $m < m_Z/2$  would not be possible.

The most general approach to introducing sterile particle content in the leptonic sector would be to add  $N$  sterile neutrinos and consider a  $(3 + N) \times (3 + N)$  PMNS matrix. This is the most general way of introducing sterile neutrinos in the model, but to keep the number of parameters as small as possible (occam’s razor), it is effectively interesting to look at a “simpler” one, where only one additional sterile family is introduced. This  $3 + 1$  paradigm, which is what will be considered in the following paragraphs, requires the introduction of a sterile state  $\nu_s$ , and a basis of four massive neutrinos  $\nu_1, \dots, \nu_4$ , with the additional assumption that the fraction of  $\nu_s$  is extremely small for the first three mass eigenstates and near 100% for the fourth, as illustrated in [Figure 1.10](#).

From the experimental evidence we can assign  $\Delta m_{4\ell}^2 \sim \mathcal{O}(1 \text{ eV}^2)$ , and since it is greater than the atmospheric and the solar mass splitting, the oscillation probability can be computed neglecting such terms — the so-called short-baseline approximation —, thereby

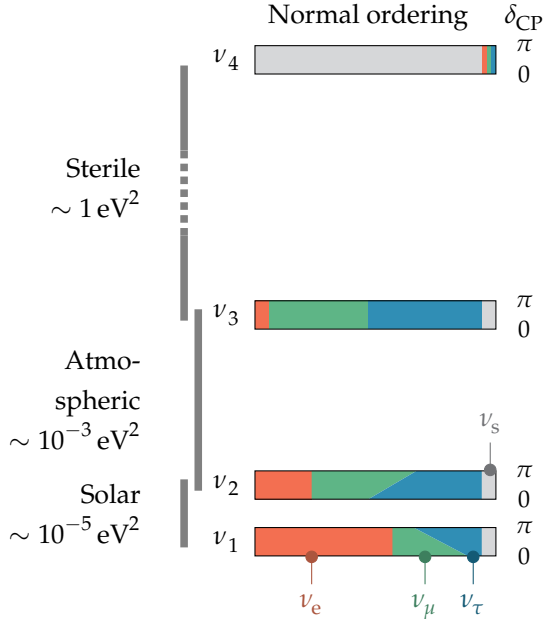


**Figure 1.10.** Representation of mass ordering, mixing, and splitting in the simplest  $3 + 1$  scenario. Normal ordering is assumed for the three active massive states. Figure expanded from [55].

giving rise to a new two-flavour oscillation probability that holds at small distances

$$\begin{aligned} P(\nu_\ell \rightarrow \nu_\ell) &\simeq 1 - 4|U_{\ell 4}|^2(1 - |U_{\ell 4}|^2) \sin^2 \left( \frac{\Delta m_{41}^2 L}{4E_\nu} \right) \\ &\equiv 1 - \sin^2(2\theta_{\ell\ell}) \sin^2 \left( \frac{\Delta m_{41}^2 L}{4E_\nu} \right), \quad \ell = e, \mu \end{aligned} \quad (1.24)$$

$$\begin{aligned} P(\nu_\mu \rightarrow \nu_e) &\simeq 4|U_{\mu 4}|^2|U_{e 4}|^2 \sin^2 \left( \frac{\Delta m_{41}^2 L}{4E_\nu} \right) \\ &\equiv \sin^2(2\theta_{\mu e}) \sin^2 \left( \frac{\Delta m_{41}^2 L}{4E_\nu} \right). \end{aligned} \quad (1.25)$$

where the first equation can be either the disappearance probability of electron or muon neutrinos, and the second controls the appearance probability of electron neutrinos from a beam of pure muon neutrinos. The “effective” mixing angles  $\theta_{\alpha\beta}$  are directly correlated with the elements of the extended PMNS matrix in the hypothesis of a  $3 + 1$  oscillation

scenario.

### 1.3.2. Experimental status and future perspectives

The experimental landscape of the sterile neutrino searches has broadened, over the years, with even more experiments adding limits to the phase space. To this day, no definitive picture has completely proved or discarded the existence of this fourth sterile neutrino state.

Different experiments can be distinguished based on the technique, target channel and the final result (evidence of a signal or data fit compatible with the null hypothesis). The experimental landscape can be classified by the channel where it is performing its research and by the result it found (i.e. *did it find any anomaly?*).

One of the most significant experimental anomalies comes from the LNSD experiment. The MiniBooNE LEE in  $\nu_e$ -appearance analysis is compatible with the results of the LNSD experiment, yet still preferring a higher mixing angle  $\sin^2 2\theta \sim 0.807$  and smaller mass splitting  $\Delta m^2 \simeq 0.043 \text{ eV}^2$ , compared to that of LNSD. It is interesting to note (for reference, see [Figure 1.9](#)) that the 3 + 1 sterile scenario did not fully explain the excess seen by the MiniBooNE experiment.

Similar to the LSND experiment was the KARMEN experiment, which, however, did not find any signature of  $\bar{\nu}_\mu \rightarrow \bar{\nu}_e$  oscillations [\[71\]](#). The KARMEN experiment operated in similar conditions to those of the LSND experiment, but at a shorter baseline of 17.7 m, thereby restricting its allowed parameter space. This posed some limits to the allowed parameter space compared to the one explored by the LSND experiment, thus not excluding its claim. Other “null-result” experiments were performed following the results of LSND and MiniBooNE, including the NOMAD experiment, which operated at a baseline of about 620 m from the source of neutrinos, produced using the SPS accelerator at CERN and with energies of  $\sim 20 \text{ GeV}$ . It excluded at 90 % CL the higher mass splitting values, adding the constraints  $\Delta m^2 < 0.4 \text{ eV}^2$  (with maximal mixing) and  $\sin^2 2\theta < 1.4 \times 10^{-3}$  for large mass splittings [\[77\]](#). MiniBooNE LEE was explored by many similar experiments; particularly interesting is the MicroBooNE experiment, MiniBooNE’s immediate successor, collecting data from BNB upstream of MiniBooNE at 472 m distance from the neutrino source. The technology is that of the Liquid Argon Time Projection Chamber [\[78\]](#), which will be described in detail in [chapter 2](#). The MicroBooNE experiment studied the individual channels of the MiniBooNE backgrounds to see whether the LEE could be created by a mismodeling of the backgrounds or whether an

oscillatory effect was really observed. Looking at multiple final state topologies in the  $\nu_e$  channel, MicroBooNE data indicated that no LEE-like signal was evident, and that background seen by MiniBooNE are coherent with the unoscillated hypothesis [79]. However, these findings were proved to not be definitive [80] since the exclusion area of the MicroBooNE experiment could not rule out the allowed parameter space of the best fit of the MiniBooNE experiment.

At long baseline multiple experiments also investigated LNSD and MiniBooNE LEE anomalies. This is, for example, the case of the ICARUS LNGS run and OPERA (CNGS1/2) experiments, collecting neutrinos produced from the Sp $\bar{p}$ S in the CNGS beam at an energy of  $\sim 17$  GeV and placed at baselines of 730 km. Both the ICARUS [81, 82] and the OPERA [83] experiments results excluded much of the parameter space of the MiniBooNE experiment, especially in the high mixing angle region, showing

$$\sin^2 2\theta < 6.8 \times 10^{-3} \quad (1.52 \times 10^{-2}) \text{ at } 90\% \text{ (99\%) CL,} \quad (\text{ICARUS}) \quad (1.26)$$

$$\sin^2 2\theta < 7.2 \times 10^{-3} \text{ at } 90\% \text{ CL.} \quad (\text{OPERA}) \quad (1.27)$$

A relevant tension is also found comparing results from very short baseline reactor experiments. The target searches are excess or deficits in the electron antineutrino flux, so it is clear that a correct evaluation of the expected flux of antineutrinos is key for such measurement. However, recent theoretical models are not in agreement with the experimental results, thereby affecting the systematic uncertainties related to the oscillation measurements. Reactor experiments are mostly not sensitive to the spectrum of energies but are considered “rate” experiments, counting the overall excess of the flux, or “spectral” experiments, looking at the energy — or  $E/L$  — spectrum. Particularly relevant are the results of the Bugey [84], NEOS [85], PROSPECT [86] and STEREO [87] experiments, which found no evidence of oscillation. NEOS was followed by the RENO experiment. The two experiments detected neutrinos produced by the same source thereby, suppressing many of the uncertainties in the flux model. The results of these experiments narrowed the parameter space with respect to the previous results [88].

In the reactor neutrino experiment landscape, an interesting result is that of the Neutrino-4 experiment. This experiment measures electron antineutrinos from a nuclear reactor SM-3 in Dimitrovgrad, Russia, using a movable detector with the ability to investigate the 6 to 10 m range of baseline distances from the reactor. This experiment reported evidence of  $L/E \simeq 1$  to 3 m/MeV oscillation, with a sensitivity of roughly  $3\sigma$ . This result is in great agreement with GA experiments such as GALLEX and SAGE. This is the sole case where this happens, since most of the RAA experiments are in tension with GA

experiments [89]. When combined with GALLEX, SAGE and BEST its statistical significance rises to  $5.8\sigma$  [90]. The result of the Neutrino-4 experiment fits well the  $3 + 1$  scenario, leading to a mass splitting of  $\Delta m_{41}^2 = 7.30 \pm 0.13$  (stat)  $\pm 1.16$  (syst) eV $^2$  =  $(7.30 \pm 1.17)$  eV $^2$  and an amplitude of  $\sin^2 2\theta = 0.36 \pm 0.12$  (stat.).

As previously mentioned, GA experiment results are in tension with most of the other experimental searches as they require a greater mixing angle. This anomaly leads to a best-fit point  $(\Delta m^2, \sin^2 2\theta) \simeq (1.25 \text{ eV}^2, 0.32)$  [75]. The overlap with the allowed regions of the LNSD and MiniBooNE LEE is negligible, and the overlap with RAA is possible with  $\sin^2 2\theta \sim 0.2$ .

Other experimental searches focus on the  $\nu_\mu$ -disappearance and  $\nu_e$ -appearance channels. These channels have been explored by NOvA [91], MINOS and MINOS+ [92]. Additional searches have also been performed with data from the IceCube detector, and interesting results will come from the JUNO neutrino experiment [93], which is now collecting its first data [94].

[Figure 1.12](#) shows a summary of all the experiments that provided exclusion areas in the parameter space, with the baseline at which they are detecting neutrinos and their energy range superimposed to the oscillation maxima in the hypothesis of a two-flavour oscillation scenario.

In this very complicated picture stands the Short-Baseline-Neutrino program [95], to which the next chapter is briefly devoted. In [Figure 1.11](#) are shown the updated allowed and excluded parameter regions from the combination of the multiple oscillation channels and multiple experimental inputs. This experiment will probe the sterile neutrino scenario with increased sensitivity up to  $5\sigma$ , exploiting a two-detector experimental search in both the  $\nu_e$ -appearance and  $\nu_\mu$ -disappearance channels.

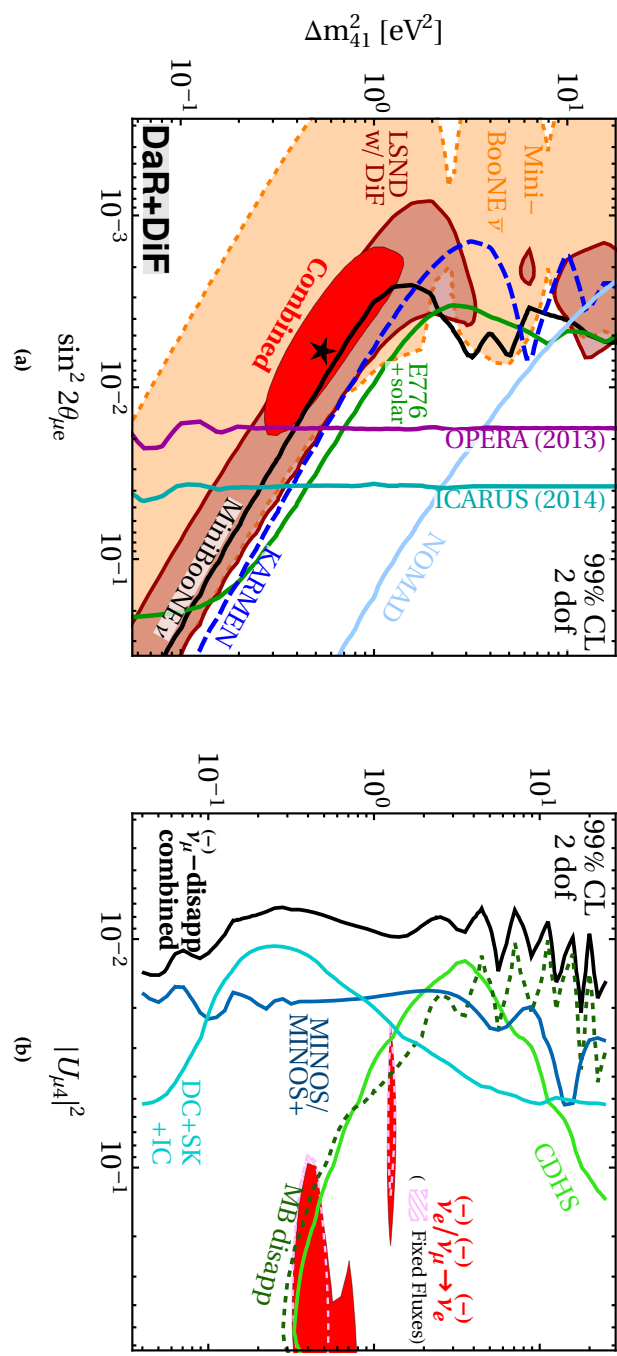


**Figure 1.11.** (a) Constraints on short-baseline  $\nu_\mu \rightarrow \nu_e$  and  $\bar{\nu}_\mu \rightarrow \bar{\nu}_e$  oscillations from the present experimental results in the presence of sterile neutrinos in 3 + 1 scenarios. (b) Constraints on the 3 + 1 scenario from  $\nu_\mu/\bar{\nu}_\mu$  disappearance. Picture taken from [93].

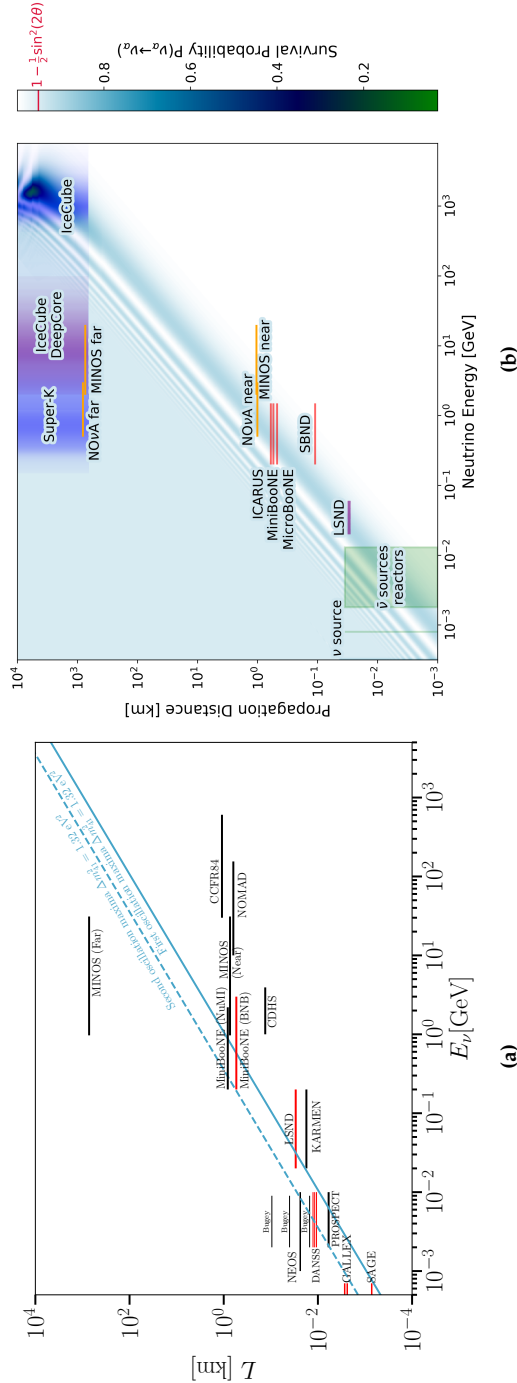


**Figure 1.12.** **(a)** (Incomplete) list of experiments searching for sterile neutrino oscillations, with baseline and energy range explored highlighted. The position of the first and second oscillation maxima for  $\Delta m^2 = 1.32 \text{ eV}^2$  is also highlighted. Experiments with results indicating a  $> 2\sigma$  preference for the 3 + 1 mixing scheme are shown in red. Picture taken from [96]. **(b)** Other, mostly new generation, experiments searching for sterile neutrino oscillations. The plot additionally show through shaded areas the survival probability  $P(\nu_\ell \rightarrow \nu_\ell)$ . Picture taken from [97].

1

# 2

2

## The SBN program at Fermilab and the ICARUS experiment

### 2.1. The Short Baseline Neutrino program at Fermilab

The Short Baseline Neutrino experimental program at the Fermi National Accelerator Laboratory (FNAL) aims to draw a complete and consistent picture of the sterile neutrino scenario, whose anomalies where described in detail in [chapter 1](#). To achieve a level of statistical significance greater than  $5\sigma$  for the LSND-allowed region (at 90% CL), SBN will carry out precision searches, recording a neutrino statistics corresponding to  $6.6 \times 10^{20}$  proton – on – target during four years of data taking. This is expected to produce approximately one million of neutrino interaction inside the SBN near and far detectors [95].

The key to such high sensitivity, other than the great statistic of events collected, is the design paradigm of the program. It employs the Liquid Argon Time Projection Chamber (LArTPC) technology [78], with two functionally identical detectors placed at different distances from the neutrino source. This allows to measure the oscillation pattern by comparing the neutrino flux registered at the far detector with the “control” flux recorded at the near detector, reducing the underlying systematic uncertainties related to neutrino production and neutrino interaction cross-sections in argon.

Albeit the original plan for a three-detector program [95], MicroBooNE collaboration anticipated data taking and the experiment was completed in 2020, two years prior to ICARUS starting its data collection campaign and four prior to SBND, so the SBN program will perform a search for the sterile neutrino as a two-detector experiment [95, 100].

Both experiments, ICARUS and SBND, collect data from the common Booster Neutrino Beam (BNB) [101]; additionally, the ICARUS detector position makes it sensitive to  $\sim 6^\circ$  off-axis neutrinos coming from the Neutrino at the Main Injector (NuMI) beam

[102].

ICARUS [103] is the far detector for the SBN program, employing an active mass of 476 t of liquid argon (LAr), at a distance of 600 m from the neutrino source; its position was chosen so as to maximise the oscillation probability (see Figure 2.1; further context is in the next paragraph). ICARUS started its data taking in June of 2022, after the initial commissioning phase. It has now finished the fourth data collection campaign, collecting  $\sim 7.54 \times 10^{20}$  POT (proton-on-target) in total, corresponding to about  $10^6$  neutrino events.

Located at a distance of 110 m, SBND [104] is the near detector of the SBN program, with an active LAr mass of 112 t. After commissioning, it started data taking in December of 2024, jointly with the far detector, thereby allowing the possibility to reduce flux- and cross-section-related systematics.

**Oscillation measurements with a two-detector experiment** The main physics goal of the SBN program is the search for a fourth sterile neutrino state assuming the 3 + 1 model. Using multiple LArTPC detectors, a high-sensitivity search for a high- $\Delta m^2$  splitting is possible by studying muon-neutrino oscillations in the  $\nu_\mu \rightarrow \nu_\mu$  disappearance and  $\nu_\mu \rightarrow \nu_e$  appearance channels [95].

The oscillation probability for both channels is presented in Eq. (1.24) and Eq. (1.25) for the disappearance and appearance channels, respectively, within the assumption of the 3 + 1 model. Looking at the data in the  $\nu_\mu \rightarrow \nu_e$  appearance channel, from the experimental results shown in Figure 1.12, the allowed parameter space lies in

$$\sin^2 2\theta_{\mu e} \in (10^{-3}, 10^{-1}) \quad \text{and} \quad \Delta m^2 \in (10^{-1}, 10^1) \text{ eV}^2; \quad (2.1)$$

the location of the near and far detector has been optimised to maximise the oscillation probability in this region of parameters. Figure 2.1 shows  $P(\nu_\mu \rightarrow \nu_e)$  for two benchmark values of  $(\sin^2 2\theta_{\mu e}, \Delta m^2)$ , assuming a neutrino energy of  $\sim 700$  MeV. The choice for a two-detector configuration arises from the need to reduce the impact of systematic uncertainties. The strong correlation between the fluxes collected in the near and far detectors is key to reducing the impact of some of the major sources of systematic uncertainties, coming from the difficulty in modelling the production mechanism and the  $\nu$ -Ar interaction cross-sections.

With a planned exposure of  $6.6 \times 10^{20}$  POT, both the  $\nu_e \rightarrow \nu_e$  and  $\nu_\mu \rightarrow \nu_\mu$  disappearance channels can also be probed to search for neutrino oscillation mediated by a sterile state. The unitarity of the 3 + 1 PMNS matrix has to be preserved so that in the event of

## 2.1. The Short Baseline Neutrino program at Fermilab 39

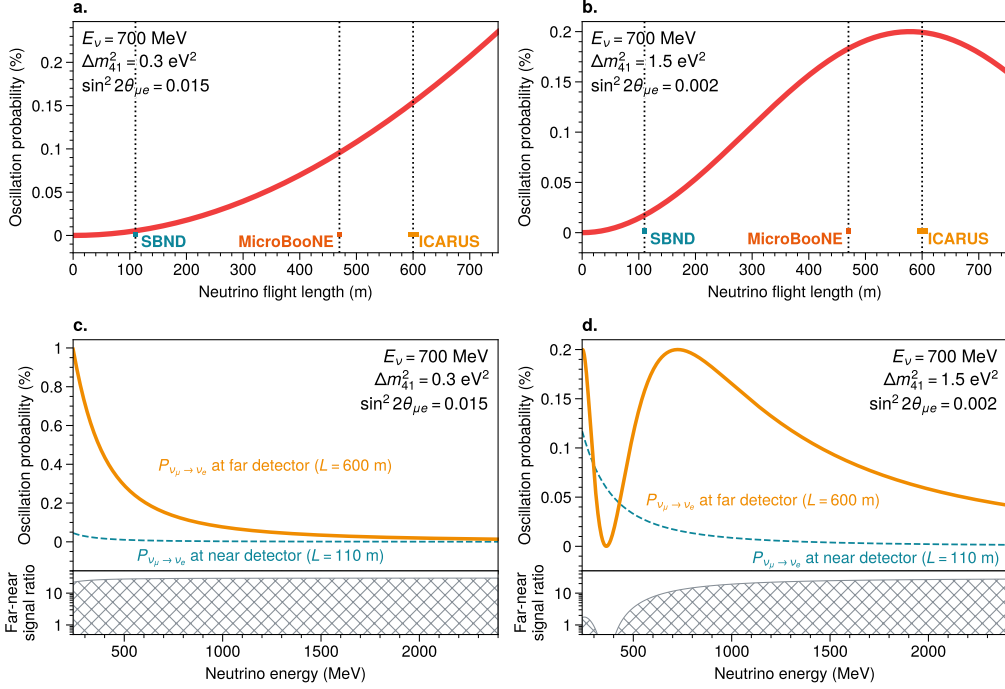


**Figure 2.1.** (a) and (b) show the oscillation probability for a 700 MeV muon neutrino into an electron neutrino as a function of the length of the neutrino flight using two benchmark values of  $(\sin^2 2\theta_{\mu e}, \Delta m^2)$ . (c) and (d) show the same oscillation probability as a function of the neutrino energy. Additionally, the bottom panels show the far-over-near event ratio. Figure adapted from [100].

$\nu_\mu \rightarrow \nu_e$  appearance, meaning a nonzero value of  $\sin^2 2\theta_{\mu e}$ , a nonzero value of  $\sin^2 2\theta_{\mu\mu}$ , or a  $\nu_\mu \rightarrow \nu_\mu$  disappearance signature, should be observed.

All three channels will be studied to either pinpoint the correct  $(\sin^2 2\theta, \Delta m^2)$  values driving short-baseline oscillations or exclude further regions in the parameter space. Figure 2.2 shows the projected excluded and allowed regions of the parameter space in both the (a)  $\nu_e$ -appearance and (b)  $\nu_\mu$ -disappearance channels of the two-detector operation of the SBN experiment. It should be noted that the projected  $6.6 \times 10^{20}$  POT exposure represents the statistics anticipated in the SBN program proposal [95]; however, BNB will operate until 2027, allowing the ICARUS detector to collect three times the statistics in standalone operation.

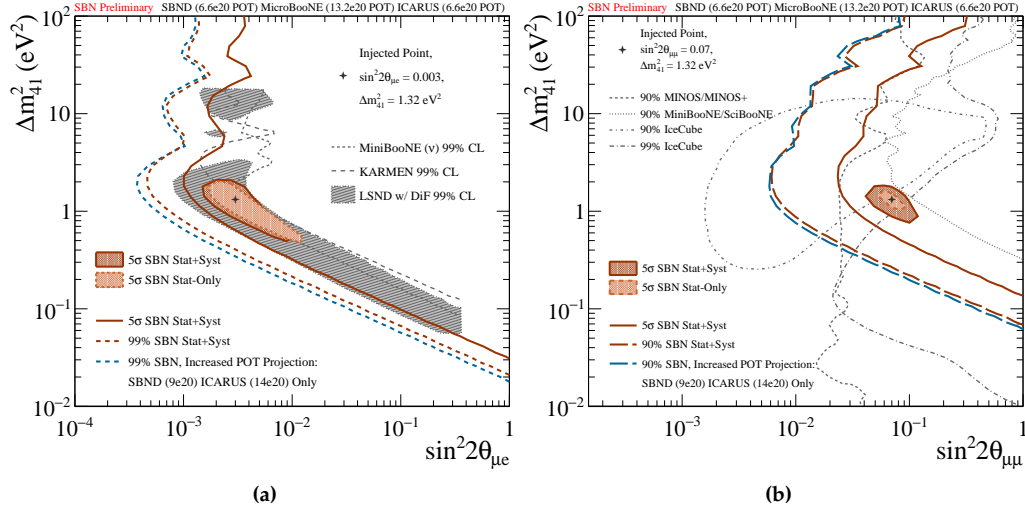


**Figure 2.2.** (a) and (b) show, respectively, the expected sensitivity exclusion (solid and dashed lines, respectively at 5 $\sigma$  and 99 % CL) and discovery (filled regions) areas in the  $\nu_e$ -appearance and  $\nu_\mu$ -disappearance channels. These projections account for an exposure of  $6.6 \times 10^{20}$  POT and a two-detector configuration.

Additionally, since a nonzero value of both  $\sin^2 2\theta_{\mu e}$  and  $\sin^2 2\theta_{\mu \mu}$  leads to a nonzero value of  $\sin^2 2\theta_{ee}$ , both the ICARUS detector, making use of the Booster and NuMI neutrino beams, and the SBND detector, only with data from the Booster beam, will explore the  $\nu_e$ -disappearance channel  $\nu_e \rightarrow \nu_e$ . The combined result of this multi-channel search will provide strong evidence in favour of or against the 3 + 1 sterile neutrino scenario.

**Cross-sections and BSM physics** In addition to the primary physics goals, the SBN program, with its two LArTPC detectors, represents a rich opportunity for neutrino physics in general.

Starting from particle interactions in liquid argon, both SBND and ICARUS detectors will use the Booster and NuMI (ICARUS-only) neutrino beams to perform cross-section measurements, exploiting the great amount of collected data with both detectors. For SBND, the proximity with respect to the neutrino source leads to a very large flux collected by the detector — each run approximately of  $2.2 \times 10^{20}$  POT corresponds to 1.5M  $\nu_\mu$  and 12 000  $\nu_e$ s; the same events will be measured by ICARUS, which at the

moment benefits from a longer data collection period and an accumulated statistic of  $7.5 \times 10^{20}$  POT in standalone operation. The larger 476 t active LAr mass of the ICARUS detector, compared to the smaller 112 t of total LAr mass for the SBND detector, also allows for a larger statistics of fully contained events, where all the final state interactions (FSI) are contained inside the detector active volume, allowing for a better particle identification (PID). Additionally, the position of the ICARUS detector allows the collection of neutrinos from the NuMI beam at an off-axis angle of  $6^\circ$  with respect to BNB direction. The added value of the NuMI beam comes from the energy range it covers. Using protons from the Main Injector at an energy of 120 GeV [102], it is able to cover the 1 to 3 GeV energy range, which overlaps greatly with the DUNE operational energy range. Neutrinos from the NuMI beam will also feature an enriched electronic component from the three-body decay of the kaon component, allowing for precise  $\nu_e$  cross-section measurements. At the moment of writing, two  $\nu_\mu$  charged current mesonless cross-section analyses,  $\nu_\mu \text{CCN} > 1\text{p}0\pi$  and  $\nu_\mu \text{CCNp}0\pi$ , are ongoing.

Finally, exploiting the tracking and calorimetric power of liquid argon TPCs, with exceptional precision and high-performance event reconstruction capabilities, the SBN program opens up invaluable opportunities for new physics searches [95, 100]. Using the off-axis NuMI beam (more information can be found in later paragraphs), it is possible to probe the decay of high-energy mesons at high angles with respect to the beam direction, hence opening up to BSM physics searches. This is the case, for example, for the first physics paper published by the ICARUS collaboration at Fermilab, looking at di-muon final state topologies to probe the existence of long-lived particles (LLPs) in kaon decays involving a di-muon FSI,  $K \rightarrow \pi + \text{LLP} (\rightarrow \mu\mu)$  [105]. This search was performed using both a selection of fully contained events and non-fully contained events, this latter motivated by the sensitivity to an extra production mode for heavy QCD axions (“ALPs”).

### 2.1.1. Neutrino beam

The location for the SBN program was selected to make use of the already existing accelerator infrastructure at Fermilab. [Figure 2.3](#) shows the FNAL accelerator complex schematic overview. This complex provides a powerful beam of neutrinos using protons extracted from the Booster accelerator, core to the operation of the SBN experiment, as well as multiple other particle beams (neutrinos and muons, as well as protons) which are employed in other experiments, such as the NuMI beam, whose main users are the

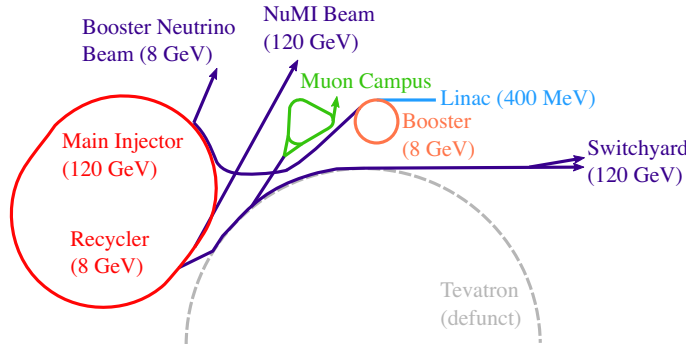


**Figure 2.3.** Schematic representation of the accelerator complex at Fermilab. Both the Booster and NuMI neutrino beams serve the ICARUS detector, covering different energy ranges, the peak being 700 MeV for BNB and 2.5 GeV for NuMI. Picture taken from [106].

NOvA and the MINOS experiments.

The common starting point is the Linac (linear accelerator), boosting protons up to 400 MeV of energy (or  $\sim 954$  MeV/c of momentum) using radiofrequency (RF) cavities. Accelerated protons are extracted and boosted to an energy of 8 GeV within the Booster ring.

From the Booster ring, a fraction of protons is extracted to be used for the Booster Neutrino Beam, whereas the remaining fraction is sent into the Main Injector accelerator. From there a second Neutrino beam is extracted, the Neutrinos at the Main Injector (NuMI) beam.

**Booster Neutrino Beam** Protons accelerated up to 8 GeV inside the Booster ring are extracted in groups of 81 bunches, each wide  $\sim 2$  ns and 19 ns apart. The repetition rate for the extraction, mainly limited by the focusing horn power supply, is of 5 Hz. Each pulse results in the collision of  $5 \times 10^{12}$  p onto a beryllium target, during a beam spill time of 1.6  $\mu$ s. The target is embedded within a pulsed electromagnet (the “horn”) that produces a toroidal magnetic field to focus positive secondary particles and defocus negative secondary particles emerging from proton-beryllium interactions. Charged mesons, which constitute the majority of the secondary particles emerging from p-Be interaction, decay in a 50-meter-long decay region. Within the decay region, charged pions undergo weak

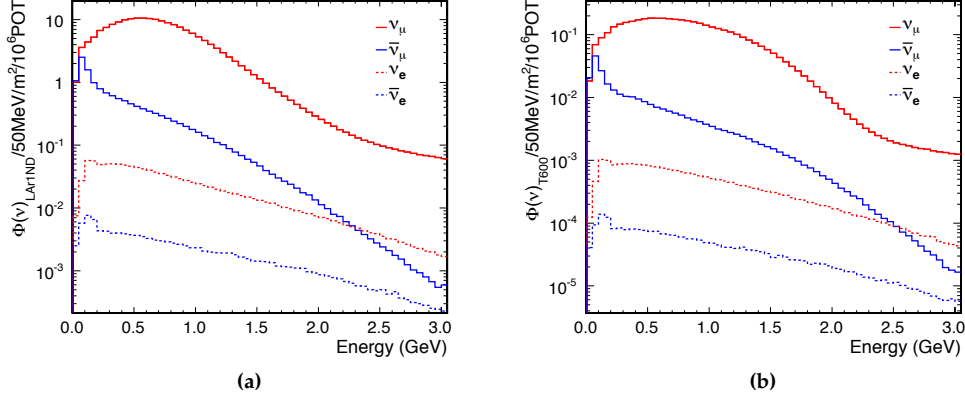


**Figure 2.4.** Predictions of the neutrino flux as computed by the MicroBooNE collaboration [107] at distances of 110 m (a) and 600 m (b) from the beryllium target, i.e., for the SBND and ICARUS detectors, respectively. Picture taken from [95].

decay

$$\pi^\pm \rightarrow \mu^\pm + \nu_\mu^{(-)}, \quad (2.2)$$

resulting in an (anti)neutrino beam. The length of the decay pipe was chosen so as to maximise the muon (anti)neutrino content and minimise the electron (anti)neutrino content coming from the decay of secondary muons

$$\mu^\pm \rightarrow e^\pm + \nu_e^{(-)} + \bar{\nu}_e^{(-)} \quad (2.3)$$

at  $\sim 0.5\%$  level. Neutrinos produced by BNB have a most probable value for the energy at  $E_\nu \simeq 700$  MeV, and a maximum energy around 2.5 GeV. When the beam is in FHC (forward horn current, selecting primarily positive mesons) mode, its composition is dominated by muon neutrinos  $\sim 93.6\%$ ; the second major component is given by  $\bar{\nu}_\mu$  coming mainly from non-defocused  $\pi^-$  (2.2) and decaying muons (2.3); the same decay accounts for, together with neutral kaon decays  $K_L^0 \rightarrow \pi^\mp + e^\pm + \nu_e^{(-)}$ , an intrinsic  $\sim 0.5\%$  fraction of  $\nu_e + \bar{\nu}_e$ .

A detailed study of the beam profile and composition, to allow for its precise simulations, was performed by the MiniBooNE collaboration [107], and experimentally verified using the Hadron Production Experiment (HARP). Figure 2.4 shows the beam fractional composition as a function of the energy of the neutrino.

**Neutrinos at the Main Injector off-axis beam** Once protons are accelerated within the Booster ring, they are then transferred inside the Main Injector ring. There protons are accelerated up to an energy of 120 GeV. The MI circumference is roughly seven times larger than that of the Booster ring, so it can hold up to seven entire Booster cycles in it. However, to make space for the pulse kicker rise time, only six are filled, adding up the spill time to 9.5  $\mu$ s: in such time window, NuMI is able to provide a flux of  $6.5 \times 10^{13}$  POT. Protons then collide against a graphite target, and produce mesons that decay inside a 675 m long decay tunnel. As for BNB, the main decay products are (2.2) muons and muon neutrinos, with a small fraction of muon antineutrinos and electron neutrinos.

ICARUS is, however, detecting neutrinos from NuMI at an off-axis angle of  $\sim 6^\circ$  with respect to the detector  $z$  coordinate, corresponding to BNB direction. This changes the composition of the beam detected by ICARUS, as off-axis neutrinos and antineutrinos have pretty much the same flux, and overall the fraction of electron (anti)neutrinos is larger. This different beam composition, added to the fact that the energy range is higher than BNB energy range, peaking at 1.5 GeV and extending up to 4 GeV, allows NuMI to be crucial for ICARUS operations: higher energies overlap better with the expected energy spectrum of future experiments, as for example the DUNE experiment, whilst a greater fraction of electron neutrinos allows for the study of both muon- and electron-neutrino argon interaction cross-sections.

## 2.2. Liquid Argon Time Projection Chambers

Core to the high sensitivity of the SBN program is the shared Liquid Argon Time Projection Chamber technology between the two functionally identical near and far detectors. The Time Projection Chamber technology was first proposed by David R. Nygren [108]. This technology, whose working principle (in this case, of a Liquid Argon TPC, which is the technology employed in the ICARUS experiment) is pictured in Figure 2.5, allows both 3D reconstruction as well as calorimetric capabilities. The basic idea of a TPC detector is that of a large volume, filled with gas or liquid, acting as the interaction medium. Charged particles interact inside this volume, producing ionisation pairs. Free electrons produced in the ionisation process are drifted by means of a strong electric field from the cathode toward the anode, where the ionisation electron charge information is collected by a position-sensitive plane, providing one or more 2D projections of the interaction. The drifting time is used as the third missing component to perform 3D event reconstruction inside the detector.

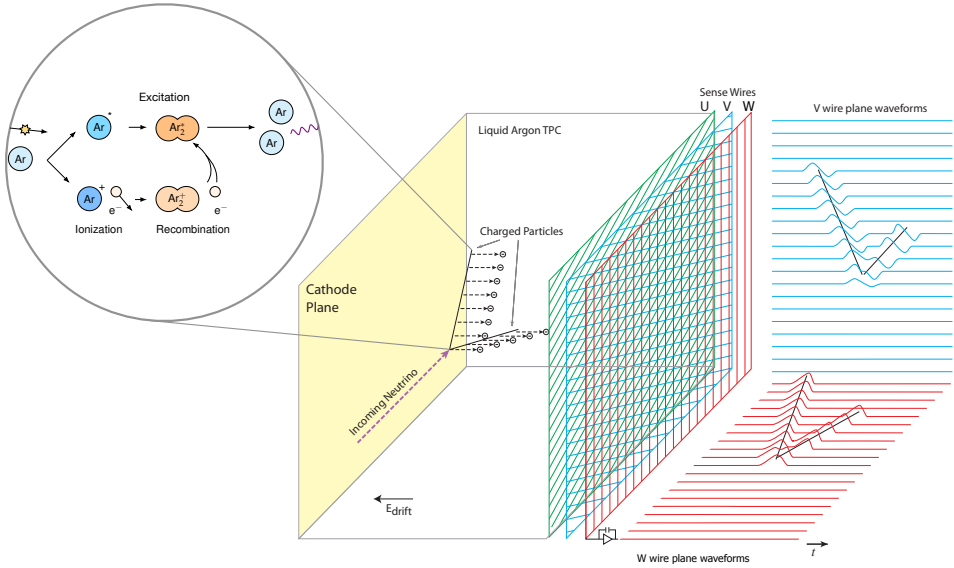


**Figure 2.5.** Illustration of the working principle of a LArTPC detector. Once neutrinos undergo weak interaction, they ionise the material, producing a large quantity of free electrons that are drifted towards the wire planes. Image adapted from [98].

The first TPCs were built primarily for high energy physics (HEP) applications, and many are still in use for major experiments, such as the ALICE tracker [109]. Carlo Rubbia proposed using liquid argon (LAr) as an interaction target for a TPC, thereby inventing the LArTPC concept for neutrino detection [78]. Liquid argon is an attractive material for particle detection, especially for neutrino physics, given its physical properties

1. LAr has a high density of  $1.39 \text{ g/cm}^3$  and a high atomic mass, which, combined with the small cross-section of  $\nu$ -Ar interaction, allows for more probable detection than most gases.
2. Being argon a noble gas, it does not attach free electrons, allowing for a longer drift lifetime.
3. It has high electron mobility,  $\mu \simeq 320 \text{ cm}^2/(\text{V s})$  for  $E \simeq 0.5 \text{ kV/cm}$  and  $T = 87 \text{ K}$ , allowing for fast drift velocity  $v = \mu E \simeq 1.6 \text{ m/ms}$ .

4. The LAr radiation length  $X_0 \simeq 14$  cm allows mm-scale calorimetry sampling of neutrino events while having a precise discrimination between electron- and photo-induced electromagnetic showers. Photons produced at the primary vertex usually show a greater conversion gap between the interaction and the starting points of the EM shower; additionally, photo-induced electromagnetic showers display an ionisation pattern in the first centimetres of the shower development compatible with two minimum ionising particles (MIP), whereas electron-induced showers show a pattern compatible with a single MIP [110].
5. At the same time, Ar is both easy and cheap to extract. In Earth’s atmosphere, it is the third most abundant gas, and can be liquified using nitrogen: this allows for great scalability required to use it for large-scale detectors.
6. LAr boiling temperature of 87.3 K causes most organic impurities to be frozen out to very low levels. This increases the drift electron lifetime.

Inside a LArTPC, once the neutrino undergoes weak interaction, it produces secondary charged ionising particles. These in turn ionise LAr nuclei, creating  $\text{Ar}^+$ ,  $e^-$  ionisation pairs and producing scintillation light. Roughly 42 000 e are produced for each MeV of deposited energy<sup>1</sup>, which are then drifted by means of an electric field toward the anodes. At the anode three planes of wires are placed in sequence, referred to as induction-1 (I-1), induction-2 (I-2) and collection (C) planes. The planes are properly voltage biased to achieve a nearly perfect transparency of the first two wire planes (I-1 and I-2) with respect to the drift electrons, enabling them to induce a charge signal on the first two planes and only be collected by the third plane. Given a nominal electric field inside the detector  $E$ , a good “transparency” of the successive wire planes to the drifting electrons is obtained by requiring that  $E_2 \geq F \times E_1$ , and  $E_1 \geq F \times E$  — where  $E_1$  and  $E_2$  are respectively the field values in the I-1 to I-2 gap and I-2 to C gap — with the scaling factor  $F \in (1.2, 1.5)$ . Due to the ionisation charge inducing a current on the first two planes and depositing the charge only on the third, the signal collected by the three sets of wires is intrinsically different: on the first two, the signal is bipolar, whereas on the third plane, the signal is unipolar.

The three planes have their wires oriented at different angles to be able to collect different “projections” of the same interaction happening inside the detector. Using this information, it is possible, in the reconstruction stage, to obtain a  $\mathcal{O}(\text{mm}^2)$ -precision ( $y, z$ )

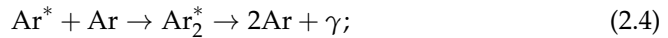
---

<sup>1</sup>This number is dependent on the electric field strength inside the detector. This value is the reference with a nominal electric field of  $\sim 500$  V/cm.

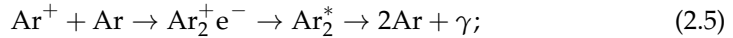
image of the interaction. The third  $x$  coordinate is reconstructed using the timing information. In fact, when charged particles cross LAr, aside from creating ionisation pairs, they produce scintillation light, which constitutes a prompt signal used to assign the  $t_0$  information. Therefore, the missing coordinate is reconstructed by comparing the time at which the electron is recorded on the wire with the prompt scintillation reference time  $t_0$ , and knowing the drift velocity of ionisation electrons inside LAr,  $x = v_d \times (t - t_0)$ .

Contributing to the formation of scintillation light within LAr are two processes, pictured in the inset of [Figure 2.5](#)

- excitation of Ar followed by the formation of the excimer state  $\text{Ar}_2^*$ , which decay with the production of scintillation photons,



- recombination of ionized argon atoms with a free electron, especially frequent with clouds of  $e^-$  around ionized  $\text{Ar}^+$  nuclei,



These two processes combined at cryogenic temperature produce 20 000 monochromatic vacuum ultraviolet (VUV) photons per MeV of deposited energy, with a wavelength of  $\lambda = 128\text{ nm}$ . This light presents two components, one so-called “fast”, with a characteristic time  $\tau \sim 6\text{ ns}$ , and one “slow”,  $\tau \sim 1.5\text{ }\mu\text{s}$  components. Scintillation light is crucial, as already mentioned, for precise determination of the interaction time, required for the trigger system to operate and to reconstruct the third coordinate. Additionally, as will be briefly discussed in [chapter 3](#), scintillation light is core for double-checking the  $(y, z)$  positioning of the interaction, providing the so-called “light barycenter”.

It should be noted, however, that aside from all the aforementioned LAr properties, there are some drawbacks to the use of LAr for particle detection. First and foremost, a complete understanding of the  $\nu$ -Ar interaction has not been reached yet, so there are large systematic uncertainties related to the parametrisation of the interaction cross-section. Secondly, in order to keep argon in its liquid phase and minimise the organic impurities, a huge effort is required for the design of the cryogenic infrastructure. Impurities lower the lifetime of drifting electrons in the TPC, making difficult to reconstruct the full charge deposited by the particles in the interaction. ICARUS, during its data taking period at LNGS, reached a record high purity of 20 ppb equivalent of  $\text{O}_2$  impurities, corresponding to a lifetime of the electron of 16 ms [[111](#)].

Whilst this latter problem is intrinsic to the LArTPC design and requires ad hoc designs and implementations of the cryogenic infrastructure to be optimised, the former problem is addressed in the SBN program by using two functionally identical LArTPC detectors, which allows the cancellation of many systematic uncertainties when performing a joint oscillation analysis [95].

Finally, even though LAr was chosen for its large electron mobility, LArTPCs are intrinsically slow detectors, with drift times of the order of milliseconds. Hence, detectors operating at shallow depth, like ICARUS and SBND, during the readout time window record significant cosmic activity. This reason led both the SBND and ICARUS collaborations to design the detectors to include an external cosmic ray tagger detector system (CRT) with nearly complete  $4\pi$  coverage to veto most of the cosmic activity. The cosmic activity during a spill gate of 1.6 ms is expected to be of 8 to 12 cosmic-rays for the ICARUS experiment and 1 to 3 for the SBND experiment.

### 2.3. The SBN near detector: SBND

The Short Baseline Near Detector (SBND) is the near detector of the SBN program at Fermilab. Located 110 m from the proton-beryllium interaction target and containing 112 t of liquid argon, SBND data will provide precise measurements of unoscillated neutrinos spectrum. As a “flux monitor”, SBND will greatly reduce the impact of systematic uncertainties related to neutrino interactions in argon and also, due to the two detectors being functionally identical, the systematic uncertainties related to the event reconstruction. Following nearly a decade of design, construction, and installation, SBND began its commissioning phase in July 2024, commencing the collection of stable BNB data at an unprecedented rate of approximately 7000 neutrino events per day in December 2024 [104].

As for the ICARUS experiment, the physics goals of the SBND collaboration extend beyond the search for eV-scale sterile neutrinos; making use of its huge statistics, due to its proximity to the beam source point, SBND will allow for extremely precise  $\nu$ -Ar interaction cross-section measurements in both the sub-GeV and GeV energy ranges. Additionally, the proximity to the neutrino source point allows the detector to cover both the on-axis as well as the off-axis phase space for BNB, expanding its capabilities to BSM physics studies similar to the ones performed by ICARUS collaboration using NuMI beam data.

SBND’s LarTPC consists of a single module, with dimensions of  $5 \times 4 \times 4 \text{ m}^3$ , hold-

ing a total mass of 112 t of LAr. The structure contains two TPCs sharing two common cathode plane assemblies (CPAs) positioned at the centre and parallel to the beam direction, and four anode plane assemblies (APAs) at the other two ends. The maximum drift length for the SBND detector is 2 m which, for the nominal electric field of 500 V/cm, leads to a maximum drift time of 1.3 ms. Each APA holds three planes of wires spaced 3 mm apart from each other, each hosting 2816 wires oriented at  $\pm 60^\circ$  (I-1/ $u$  and I-2/ $v$ , respectively) and  $0^\circ$  with respect to the vertical  $y$  axis.

The photon detection system (PDS) of SBND was developed to enhance the light collection and at the same time test relevant technologies for future generation experiments such as DUNE. The first task is addressed by making the cathode reflective and also coated in TPB, thereby allowing the light shifted from VUV to  $\sim$ 400 nm where PMTs operate to be collected with increased efficiency. The second item for SBND’s PDS was addressed by adopting two different light collection systems, PMTs, as for many other LArTPCs, and X-ARAPUCA. These are new innovative light collection technologies developed for the present and future detectors like ProtoDUNE and DUNE, adopting the silicon photomultiplier technology for light collection [112].

The SBND detector finished its commissioning phase last summer and since then has started collecting physics data alongside the ICARUS detector for use in the SBN program.

## 2.4. The ICARUS-T600 detector

The ICARUS (Imaging Cosmic And Rare Underground Signals) detector, the far detector for the SBN program, with an active mass of 476 t of liquid argon, is the first ever large-scale operating LArTPC detector [113]. It consists of two identical adjacent T300 modules with internal dimensions  $3.6 \times 3.9 \times 19.6$  m $^3$ . Each T300 module houses two adjacent LArTPCs separated by a common cathode, with a maximum drift distance of  $\sim$ 1.5 m, equivalent to a drift time of  $\sim$ 1 ms for a nominal 500 V/cm electric drift field.

The cathode is built up by an array of nine panels made of punched stainless steel, allowing for a 58 % optical transparency between the two drift regions. The anode plane assemblies are made of three parallel wire planes, spaced 3 mm apart; each plane holds 150  $\mu$ m thick stainless steel wires oriented on each plane at different angles with respect to the horizontal direction. The wire orientation for the planes in the ICARUS detector is quite unique with respect to other operational LArTPCs. For both TPCs in a T300 module, the Induction-1 wires are at  $0^\circ$ . The orientation of the Induction-2 and Col-

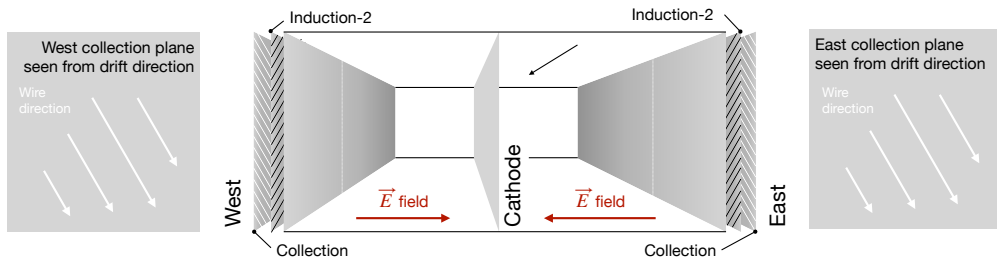


**Figure 2.6.** Illustration of the wire direction for the I-2 and C planes for the East and West anode wire planes for each T300 module. The two side panels show the wire direction as seen by an observer located at the central cathode plane and pointing to the drift direction in both TPCs.

lection planes is different for the East and West TPC in each T300 module as shown in Figure 2.6. For the East anode planes in both East and West cryostats, Induction-2 is oriented at  $60^\circ$  and Collection at  $-60^\circ$ , whereas for the West anode planes, their orientation is reversed, with I-2 at  $-60^\circ$  and C at  $60^\circ$ . With this design, as illustrated in the images on both sides of Figure 2.6, electrons drifting from either TPC “see” the wires in both the I-2 and C planes as identically oriented [113].

In total 53 248 wires spaced 3 mm apart with lengths up to 9 m across the three planes are installed inside the detector. By appropriately voltage biasing the first two planes (Induction-1 and Induction-2), a non-destructive charge measurement is provided, whereas the full ionisation charge gets collected by the Collection plane. The three planes are kept at  $-250\text{ V}$  (I-1),  $-30\text{ V}$  (I-2) and  $+250\text{ V}$  respectively. The scintillation light is collected by a set of 360 PMTs located behind the wireplanes in the APAs. Photos of the installed planes of wires and PMT mounting are shown in Figure 2.7.

The two T300 adjacent modules making up the ICARUS detector are housed inside a warm vessel, in which  $\text{LN}_2$  is circulated, acting as a cold shield and preventing heat from external thermal insulation from reaching the LAr containers. The external warm vessel uses 60 cm of polyurethane foam to keep argon at its liquid phase just below the boiling point at 87 K. A schematic of the ICARUS detector and the positioning of the two T300 modules is provided in Figure 2.8.

The ICARUS collaboration successfully collected neutrino interactions during a three-year run at the deep underground laboratories beneath the Gran Sasso Mountains, LNGS (Laboratori Nazionali del Gran Sasso) from 2010 to 2013 [113]. The nearly 3000 neutrinos

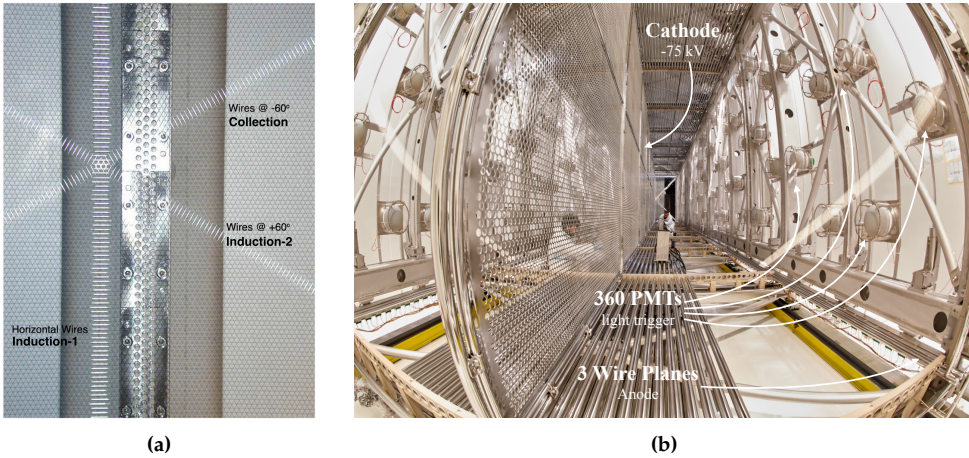


**Figure 2.7.** (a) shows the three planes of wires as installed in the ICARUS detector. (b) shows an inner view of one of the TPCs, with the common central cathode on the left and the anode plane assembly on the right, with the PMTs installed. Figures taken from [103, 113].

collected by the ICARUS detector at LNGS were produced by the CERN to Gran Sasso Neutrinos beam (CNGS) with energy of 10 to 30 GeV using protons from the Sp $\bar{p}$ S accelerator at CERN.

The ICARUS detector operating at LNGS demonstrated the superior detection capabilities of the liquid argon TPC design: the detector showed a remarkable e/ $\gamma$  separation and particle identification exploiting the measurement of  $dE/dx$  versus range. The momentum of escaping muons was measured by studying the multiple Coulomb scattering with  $\sim 15\%$  average resolution in the 0.4 to 4 GeV energy range [114].

LNGS operations demonstrated the feasibility of achieving an exceptionally high level of LAr purity, with a <50 ppt O<sub>2</sub>-equivalent level of impurities. In 2013 the low-point record of 20 ppt O<sub>2</sub>-equivalent level of impurities was reached [111], corresponding to an exceptionally high electron drift lifetime of 16 ms, marking a milestone for many future experiments, such as the Deep Underground Neutrino Experiment (DUNE). Furthermore, during this period of activity, the ICARUS detector probed the sterile neutrino picture alongside the OPERA detector, providing essential limits toward a better — though not definitive — understanding of the short-baseline neutrino anomaly [81–83].

From 2015 to 2017 the ICARUS detector underwent a thorough overhaul, first at Lab-

52      Chapter 2. The SBN program at Fermilab and the ICARUS experiment

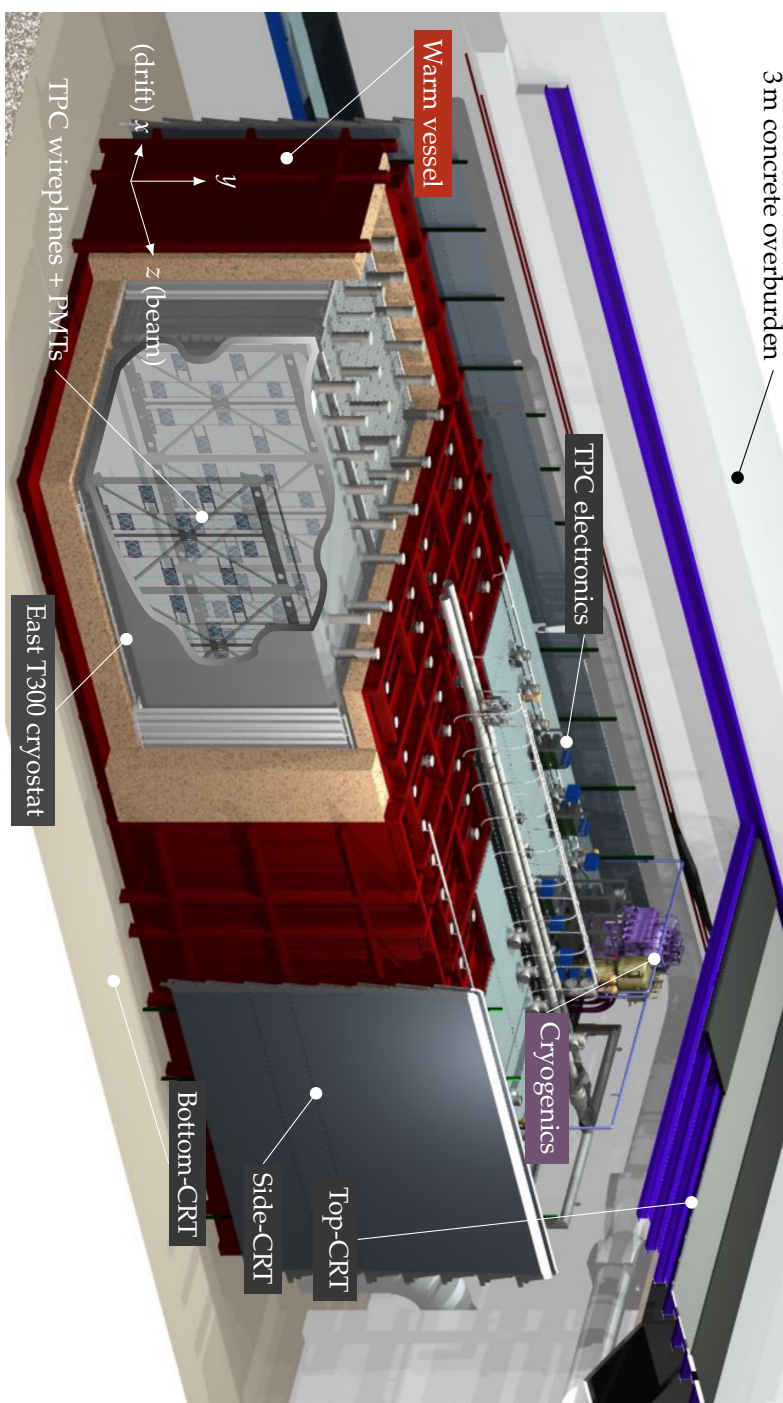


**Figure 2.8.** Illustration of the ICARUS T600 detector at Fermilab. Surrounding the warm vessel is the  $4\pi$  coverage CRT. Above the warm vessel, the TPC readout warm electronics are placed, alongside the proximity cryogenics. Inside the warm vessel two identical (east and west) T300 modules are hosted, each containing two TPCs sharing a common cathode at the centre and two anode plane assemblies, one on each side.

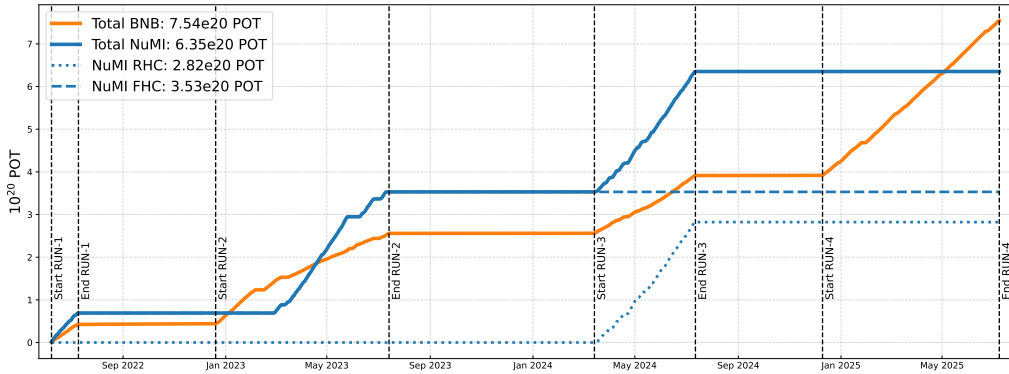


**Figure 2.9.** Booster Neutrino Beam and NuMI beam proton-on-target collected with ICARUS detector. Courtesy of the run-coordination ICARUS group.

oratori Nazionali di Legnano, Padova (Italy) and then at CERN in the Nutrino Platform framework (WA104/NP01 project), where the TPC electronics were updated to withstand the higher throughput a shallow-depth operation could require, as well as the light collection system and the cryogenic infrastructure. It was then moved in 2018 at Fermilab, where it was placed on the BNB baseline at a distance of 600 m from the source target, operating as the far detector for the SBN program, collecting data from the Booster Neutrino Beam and from the NuMI beam.

All the ICARUS detector subsystems — TPC, PMT and CRT — were commissioned from early 2021 to June 2022, when also the deployment of the concrete overburden was completed [103]. This avoids heavy neutral particles entering the TPC volume, resulting in a reduced background activity.

After the commissioning phase, the first physics data collection run started, lasting until the summer shutdown. Following Run-1, and until the moment of writing, we collected three more physics runs until the recent summer shutdown. The collected/delivered efficiency is estimated to be greater than 95 %, with a collected exposure of  $7.54 \times 10^{20}$  POT for BNB using the FHC mode and a total of  $6.35 \times 10^{20}$  POT for the NuMI beam, split between  $3.53 \times 10^{20}$  POT in FHC mode and  $2.82 \times 10^{20}$  POT in RHC mode. Figure 2.9 shows the cumulative POT collected from the start of the ICARUS operations to the present day.

### 2.4.1. The ICARUS detector subsystems

All three components (sub-detectors or sub-systems) of the ICARUS detector, upgraded during the detector overhauling process at CERN, are essential for the detector operation and to accomplish its physics goal.

**TPC** One of the largest overhauls performed at CERN was the complete redesign of the TPC electronics. During operation at LNGS, the wires were grouped in bunches of 576 wires, read out and filtered to achieve a unipolar signal from all planes. This was convenient in terms of post-processing but showed strong limitations in the case of intense showers [115]. Such an approach was incompatible with the high rates foreseen for the ICARUS shallow-depth operations at FNAL. The new system combines the previous architecture, which allows for a continuous triggerable multi-buffered waveform recorder for each wire of the detector, with a more advanced design.

TPC wires are grouped together in bundles of 18 cables and feed through the 96 chimneys positioned above the TPC cryostats. At the other end of the chimneys, the signal is read by the front-end electronics, that are hosted in custom-designed mini-crates mounted on the ultra-high vacuum feedthrough on top of the chimneys. The interface between the TPC wires and the front-end electronics is given by the Decoupling and Biasing Boards (DBBs); each DBB is designed to house two isolated 32-channel banks, allowing each TPC wire to be biased at the proper voltage, enabling proper transparency to ionisation charges, and at the same time preventing parallel noise contributions to wire signal from leakage currents. DBBs are designed to operate in GAr (gaseous argon) and can provide a maximum of 400 V of voltage bias. The 53 248 TPC wires are bundled in 1664 32-channel bunches and fed to 856 DBBs on the 96 chimneys: on each chimney flange are installed 9 DBBs, serving 576 TPC wires. It is important to note that, while both MicroBooNE and SBND have the TPC readout electronic cold to allow for lower noise RMS, ICARUS has opted to keep its TPC electronic partially warm and thus positioned outside of the TPC cryostat, allowing for easy serviceability.

The analogue signal is then fed to custom-designed CAEN A2795 boards, housing eight amplifier boards each and capable of integrating and digitising eight channels, for a total of 64 channels for each CAEN board. High throughput is accomplished by employing optical fibre connections in a serial link with a bandwidth of 1.25 Gb/s. The digital signal is expressed in units of ADC counts, with the overall TPC electronic giving 1 ADC count per  $\sim 65$  e (or equivalently,  $dQ/dx \simeq 1000$  ADC/cm for a MIP, for which

$dE/dx \simeq 2.1 \text{ MeV/cm}$ .

**Light collection system** As mentioned before, once a charged ionising particle crosses liquid argon, ionising it, scintillation light, or VUV photons, is produced from the deexcitation of argon dimers. The light information is crucial for the operation of the ICARUS LArTPC, providing essential information to the event trigger, identifying the interaction occurring in the BNB and NuMI spill gates, as well as calorimetric and position information, useful to complement the 3D track reconstruction by providing absolute timing for each track.

The ICARUS Light Detection System, or LDS, consists of 360 Hamamatsu 8" R5912-MOD PMTs deployed behind the plane of wires (see figure 2.7b). Being the PMT glass opaque to the VUV 128 nm light produced by LAr scintillation, they need to be coated with a  $200 \mu\text{m}/\text{cm}^2$  layer of tetraphenyl butadiene (commonly known as TPB) to convert the VUV light into visible light.

All PMTs are mounted onto the TPC mechanical frames using a supporting system that allows the PMT to be positioned 5 mm behind the collection plane. A stainless steel grid cage is mounted around each PMT to mitigate the induction of fake signals on the nearby wire planes by the relatively large PMT signals. The PMTs can be calibrated in time with a laser system based on a Hamamatsu PLP10 laser diode, emitting laser pulses with  $\lambda = 405 \text{ nm}$  and an FWHM of 60 ps, delivered to single PMTs via optical fibres [116].

**Cosmic ray tagger** Due to its installation at a very shallow depth at the Fermilab BNB baseline, the ICARUS detector is subject to a high rate of cosmic ray-induced interactions,  $\sim 10 \mu$  tracks per neutrino candidate inside the detector volume. These particles are one of the primary background components of multiple neutrino physics analyses, as a muon inside the detector volume could be misidentified as the result of a neutrino interaction. The Cosmic Ray Tagger (CRT) is therefore designed to actively address this problem. It fully encloses the detector, covering it from all sides, tagging cosmic muons to clearly identify neutrino interactions.

It is divided into three parts: the top, side and bottom modules. Each of these modules consists of six smaller components to allow for some granularity in the detector, employing the plastic scintillator technology.

The top CRT is designed to cover the top part of the ICARUS detector; placed just below the 3 m concrete overburden, it intercepts almost 80 % of the overall cosmic muon

flux. It is comprised of 123 detector modules, each with an area of  $1.86\text{ m} \times 1.86\text{ m}$ . Each module is made of two orthogonal layers of 8 plastic scintillator bars in which the light is collected by wavelength-shifting optical fibres and read out on both sides by Hamamatsu silicon photomultipliers, enclosed in an aluminium box. The 32 SiPM signals of each Top-CRT module are connected to a CAEN DT5702 Front End Board (FEB) to produce trigger logic based on the coincidence between two SiPMs on the same bar and between two layers in a module.

The side CRT is made using the recovered modules from the MINOS experiment, refurbished with the addition of the SiPM technology to read out the scintillation light.

Finally, the bottom CRT, placed under the detector, is made of 14 modules. Each module was retrieved from Double Chooz experiment and is made of polystyrene strips, and the scintillation light is read out by Hamamatsu PMTs.

In both side and bottom CRTs, the scintillation light is collected by wavelength-shifter optical fibres that are read out by light-sensitive detectors.

More detailed information about the CRT system can be found in Refs. [117–119].

# 3

## ICARUS data processing and event reconstruction

3

The description of the ICARUS detector and all its subsystems clearly hints at the complexity of such a detector and the large amount of data that it produces. This chapter is devoted to describing the process of data acquisition, from the time a “trigger” signal tells the detector subsystems to collect data to what offline processes are applied to the data streams coming from all subdetectors in order to transform the raw data into physics-informed outputs.

### 3.1. Data acquisition

**ICARUS trigger** In a few words, the ICARUS trigger employs the coincidence between the signal from the beam (BNB and NuMI) spill gates and the scintillation light to provide a global signal that activates the acquisition windows for the TPC and PMT subsystems [120]. For TPC, the choice of the acquisition window is driven by the distance between the cathode and the anode. This is the maximum drift distance an ionisation electron produced in time (during the beam spill gate, triggering the event) can travel. With a nominal electric drift field of 500 V/cm, and a half-width of  $\sim 1.5$  m, the maximum drift time is 1.6 ms. The acquisition window for PMTs is driven by the mean lifetime of LAr excited states. De-excitation of LAr produces scintillation light in two components, one fast  $\tau \simeq 6$  ns and one slow  $\tau \simeq 1.6$   $\mu$ s [121]. To collect the entire scintillation light signal, the time window has to be thus greater than the BNB (NuMI) beam gate 2.2  $\mu$ s (10.1  $\mu$ s). The PMT signal is read in primitives (short buffers of readout signal) of 10  $\mu$ s, with 3  $\mu$ s (7  $\mu$ s) of pre-(post-)trigger buffer. Additionally, in the case of a second light trigger in the 10  $\mu$ s immediate subsequent window, the readout is extended by 7  $\mu$ s. In the case a global trigger is issued, three primitives are recorded without the

first pre-trigger buffer, so a 26  $\mu\text{s}$  window is read out [120].

The ICARUS trigger architecture allows for multiple configurations, i.e., the acquisition of different types of events [120]. The main ICARUS trigger physics configuration (on-beam majority) is based on the multiplicity of PMT signals in coincidence with the beam “open” spill gate. This configuration maximises the probability of collecting neutrino interactions and reduces the rate of cosmic-triggered events. To perform detector calibration, it is, however, useful to have a few runs with collected cosmic interactions. To achieve this, minimum bias configurations are created, bypassing the need of a scintillation light signal to perform a global trigger and instead capturing all the detector subsystem data at the maximum rate possible with the DAQ capabilities, around 4 Hz. Additionally, any mentioned global trigger configuration can be issued on- and off-beam by adjusting a delay. The on-beam configuration has no delay with respect to the used configuration (either majority or minimum-bias), whereas the off-beam trigger has a delay of 33 ms.

**Collection of the triggered events.** Once a global trigger is issued, the data acquisition system (DAQ), which communicates via TCP/IP protocol with the trigger system [120], activates the readout of the whole detector, opening 1.6 ms and 26  $\mu\text{s}$  acquisition windows for the TPC and PMTs, respectively. The ICARUS DAQ system is based on the *artdaq* data acquisition software development kit (SDK) developed and maintained at Fermilab for use in several accelerator-based experiments [122].

The *artdaq* SDK provides customisable applications for reading data fragments (buffered pieces of data from each of the ICARUS subdetector modules) from detector elements identified as *BoardReader* objects. Each *BoardReader* acquires the data stream for a part of one of the ICARUS subdetectors: TPC, PMT and CRT readout electronics, and from trigger and White Rabbit. The White Rabbit hardware, employed in the ICARUS detector, allows precise (sub-nanosecond) scale timing across the multiple subsystems using a network interface. Event counters and timestamps are assigned accordingly to each data fragment, which are then queued for data transfer. When a global trigger is issued, the trigger *BoardReader* stream is passed to the *EventBuilder*, which are computers aimed at collecting the buffers from all the ICARUS subsystems and compacting them into a single event. Once the *EventBuilder* reads a trigger signal, it also collects the streams from the other *BoardReaders*. Figure 3.1 shows a simplified illustration of the flow of the data signals from the ICARUS components to the creation of the full event. Once the events are created by the *EventBuilder*, they are distributed for monitoring the data quality and

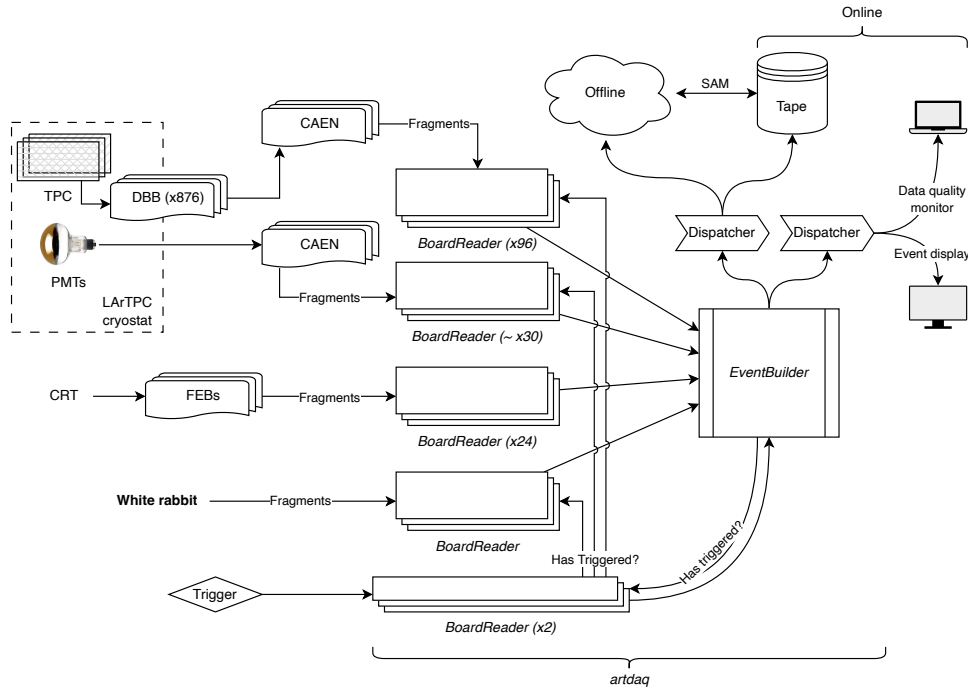


**Figure 3.1.** Simplified illustration of the ICARUS DAQ system. Further information is found in [section 3.1](#).

for long-term storage.

**TPC data** The TPC data input to the DAQ EventBuilder corresponds to the digitised waveforms from each TPC readout channel, representing the charge signal (as a function of time) induced by the motion of ionisation electrons drifted by the electric field inside the detector.

**PMT data** Similarly to the TPC data, the data from the PMTs correspond to the digitised waveforms of the readout of every PMT inside the detector. For any event triggered in coincidence with the beam spill, the digitised signals of all 360 PMTs are recorded in 26  $\mu$ s long time intervals, sampled at 500 MHz. In addition to this data, whenever an off-time cosmic ray event crosses the volume, triggering scintillation light acquired by the

PMTs in the  $\pm 1$  ms around the beam gate, all 180 PMTs belonging to the T300 module containing the interaction are recorded in 10  $\mu$ s long time intervals.

**CRT data** For the CRT system the DAQ acquisition and processing are slightly different [117–119]. The ICARUS CRT components operate in self-trigger mode [99, 117], whenever a CRT SiPM exceeds the threshold, the data from all 32 SiPM channels for each FEB (Front End Board, see section 2.4) is stored in internal buffers, holding up to 40 to 80 ms depending on which CRT sub-part is considered. The data from the top, bottom and side CRTs, which count as a function of time the number of photons readout by the SiPM at the ends of the scintillating strips, is aggregated within 10  $\mu$ s data fragments in the BoardReaders instances; once the global trigger is activated,  $\pm 25$  ms of CRT data fragments are sent from the BoardReader to the EventBuilder instance.

**Saved data** Downstream of the DAQ interface, events are written using the *art* event-processing framework [123], on which the *artdaq* SDK is built. This allows interoperability between the DAQ interface and the offline analysis, without the need to convert the events saved from the DAQ interface into a format compatible with the high-level offline analysis. *art* files are essentially ROOT files [124] with custom data types stored in them. The data collected by the ICARUS DAQ system are written in different file streams based on their specific acquisition mode, including the beam source (if on-beam), the specific trigger configuration active and its specific setting.

After a period of dedicated tests and effort to validate the setup, the DAQ system granted stable acquisition of high data rates up to 5 Hz [103]. This is, however, larger than the amount of data input foreseen for the system with both BNB and NuMI beams and with the majority-based trigger configuration: the data throughput corresponds to  $\sim 1$  Hz.

## 3.2. ICARUS Data processing

The output of all ICARUS sub-detectors is common across LArTPC detectors, which might have different TPC geometry and light collection configurations but share the same underlying technology. The *art*-based *LArSoft* framework [125–127] is the common software development kit providing software infrastructure and algorithms for processing the collected data and additionally providing tools that enable the simulation of the

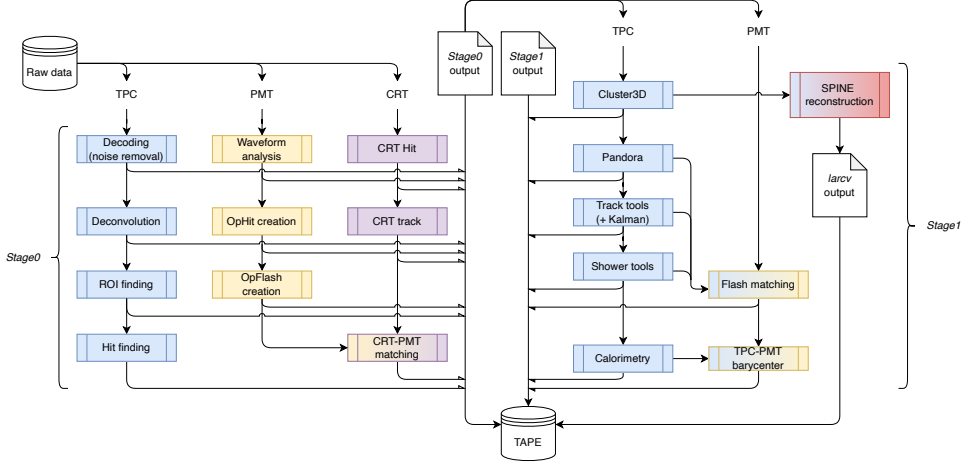


**Figure 3.2.** Illustration of the data processing pipeline used for ICARUS data showing the steps involved in both *Stage0* and *Stage1*. Further details on the processing chain are given in the text.

physics events and the response of the detectors, as well as the downstream event reconstruction.

LArSoft allows processing the data by applying different algorithms, called modules, to the data stored in the *art*/ROOT files. The modules are steered by configuration files that allow a great degree of flexibility.

The data processing and event reconstruction proceed in two steps. First the raw data collected by the ICARUS DAQ is processed to produce a simpler representation of the signal, so from the raw digitised waveforms, *hit* objects are created. Hits are objects containing only the “signal-related” part of the raw waveform, therefore allowing more manageable data files. Inside this step of the processing, the signal on the wires and the signal from the PMTs and from the CRTs are analysed and translated into different hit types, depending on the subsystem. This step is commonly referred to as *Stage0*. Once the data is processed, a second stage, referred to as *Stage1*, deals with the high-level event reconstruction and aims at building a complete picture of the physics interaction happening inside the detector. This encompasses, for example, the creation of the reconstructed interaction and its identification from the hits reconstructed from the TPC wires. Further details are provided in [section 3.3](#) and [chapter 4](#).

[Figure 3.2](#) pictures the overall *Stage0/Stage1* chain which is applied to the data files produced by the ICARUS DAQ. A detailed description of these steps follows in the next paragraphs.

### 3.2.1. Light reconstruction

One of the first steps in *Stage0* reconstruction addresses the reconstruction of the light signal. Reconstruction of the light signal associated with the event of interest is based on the recorded PMT signals in the events.

Light reconstruction starts from the identification of the PMT signal, using a threshold-based approach. To do so, a “pedestal” is defined: this step is performed using a sliding window and mediating the photoelectron counts to define the central value. The pedestal is subtracted from the raw signal, and the pedestal-subtracted waveform is used to identify when the signal is above threshold, using three thresholds defining the start, tail and end time points of the PMT hit, called *OpHit*. Once the three time values are identified, an *OpHit* is created. In an *OpHit*, the start, end and tail timestamps are saved, and the area under the curve between these three points is computed. The integral of the waveform is proportional to the integral of the collected charge of the PMT that is in turn proportional to the collected light. If a start threshold is reached before the end of a previous *OpHit* the hit is truncated. [Figure 3.3\(a\)](#) shows the example of a PMT with a clear single *OpHit*.

After individual optical hits are reconstructed, they are clustered together into higher-level objects, called *OpFlashes*, corresponding to multiple optical hits happening in proximity inside the detector, likely originating from the same physical event inside the volume. [Figure 3.3\(b\)](#) shows the signal from multiple PMTs whose *OpHit* are clustered into a single *OpFlash*.

All data products created in the *Stage0* PMT processing are saved using the same *LArSoft*-based structure to ROOT files.

### 3.2.2. Cosmic ray tagger reconstruction

The first step in the reconstruction of the CRT signal is the extraction of the number of photoelectrons  $n_{\text{pe}}$ . This is done starting from the raw ADC counts, subtracting the pedestal and correcting for the amplification gain

$$n_{\text{pe}} = \frac{\# \text{ADC} - \text{ped}}{G}. \quad (3.1)$$

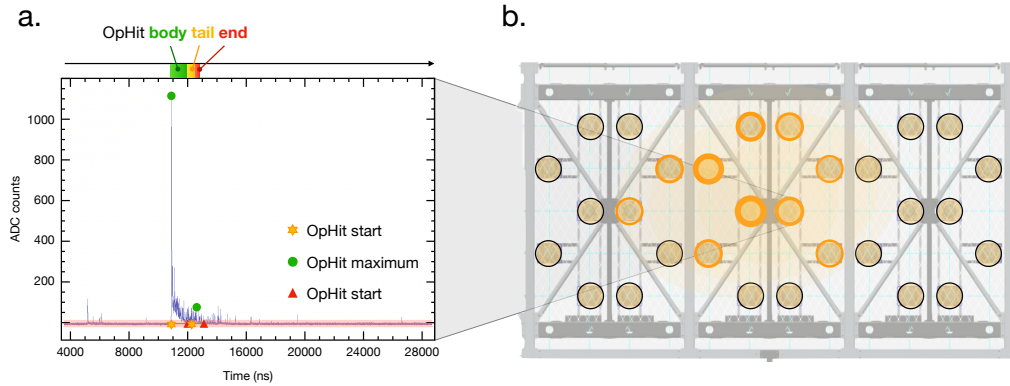


**Figure 3.3.** Illustration of an interaction as seen by the PMTs inside the detector volume. (a) shows the pedestal-subtracted waveform produced by a single fired PMT, where the *OpHit* information is marked on top, with the three regions (body, tail and end) highlighted. (b) shows all the PMTs activated during an event in the TPC volume; the PMTs collecting a light signal above the defined threshold are indicated in yellow. Their signal is used to build the so-called *OpFlash* object.

A preliminary selection for the side CRT data is performed, requiring each signal to be above a 7.5 pe threshold. Top CRT data are instead selected with a different requirement, i.e., a “quadruple” signal coincidence is necessary to generate a hit as shown in [Figure 3.4\(a\)](#). At this point it is possible to create the *CRT Hit* objects for side and top CRTs. Two timestamps are associated with each hit:  $T_0$  which identifies the global timing of the recorded hit and is provided by the White Rabbit switch system, and  $T_1$  which identifies the relative timing of the hit with respect to the trigger. Additionally, each CRT hit object has its position in the detector reference frame associated. Due to the differences in the CRT modules between the side and top CRTs, the position computation is slightly different.

By using the quadruple coincidence, the position of top CRT hits in each module is known with a granularity of  $23 \times 23 \text{ cm}^2$ . [Figure 3.4\(b\)](#) shows the distribution of the CRT hits using a collected calibration run.

For the side CRT modules the position in the detector (reference) frame is reconstructed with a slightly different approach. The coincidence of adjacent layers is reconstructed offline via software because the same modules are being read by multiple FEBs. Hit scintillator strips are identified by selecting in each FEB the channel that generated

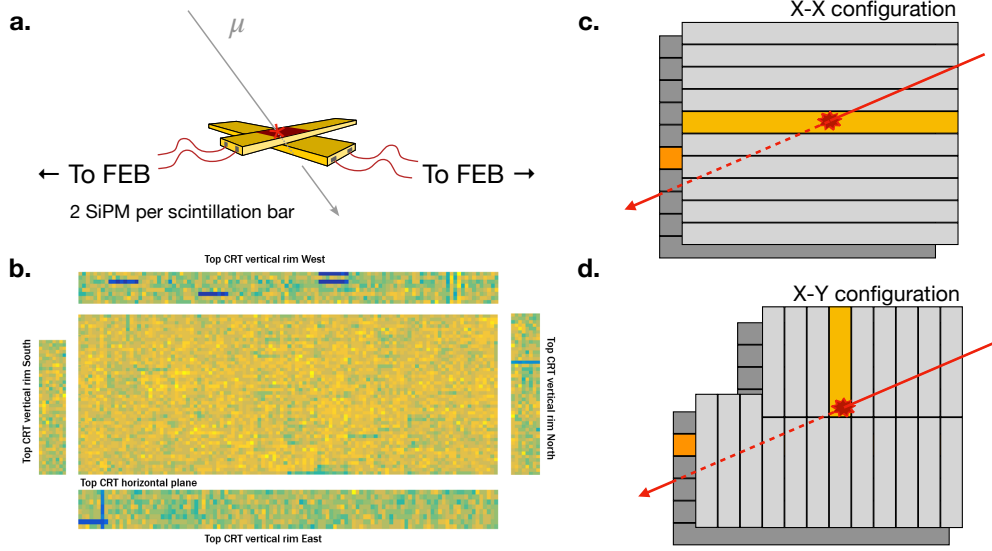


**Figure 3.4.** Illustration of CRT hit position reconstruction. (a) shows the reconstruction for the top CRT modules, where the quadruple coincidence between two scintillation bars is required. (b) shows the distribution of the CRT hits reconstructed in the different regions of the Top CRT. Blue regions correspond to malfunctioning channels. (c) and (d) show, respectively, the configuration of the east, west and north side CRT and south CRT modules. (b) is taken from [118], (a), (c) and (d) are adapted from [99].

the FEB trigger signal, which is the one with the highest charge amplitude. Figure 3.4(c) and (d) show two of the configurations of the CRT side module strips. The triggering strip is shown in yellow, and the red star shows the interaction point. The north, east and west side CRTs have the X-X configuration shown in Figure 3.4(c). For these components, if two opposite SiPM signals are collected within 150 ns, and read out by two FEBs, the longitudinal position (across the strip) can be computed with respect to the centre position of the strip by comparing the timestamps recorded by each FEB:

$$z = (T_B - T_A)/2 \cdot v_{\text{wls}}, \quad (3.2)$$

where  $T_A$  and  $T_B$  are, respectively, the two timestamps recorded by the FEBs and  $v_{\text{wls}}$  is the group velocity of the light signal inside the wavelength shifter fibre. The south CRT wall instead was built with the X-Y configuration shown in Figure 3.4(d). In this case, a coincidence offline software-based approach similar to that used for the top CRT

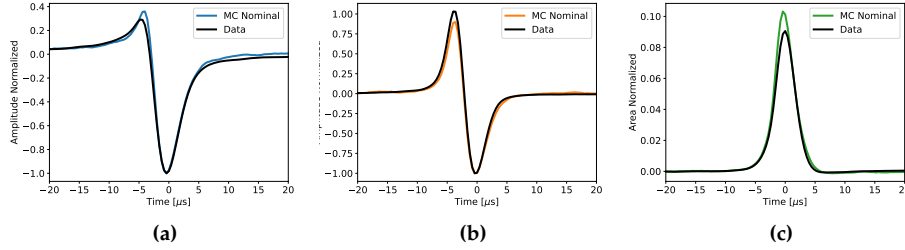


**Figure 3.5.** Typical raw signal captured by the three planes (induction-1 (a), induction-2 (b) and collection (c)) and showing the characteristic bipolar signal for the two induction planes and the unipolar shape for the collection plane. The signal is averaged in the  $\theta_{xw}$  angle, where  $x$  is the drift coordinate, and  $w$  is the orientation of the wires in the  $w$  plane. Picture taken from [129].

3

component is employed by exploiting the orthogonal relative position of the outer and the inner strips.

The last step performed in *Stage0* concerns the temporal matching of the light and CRT information. This step is important, especially for higher-level processing, where it can be exploited to improve the efficiency by which correct interactions are selected inside the detector, rejecting out-of-time activity using the CRT-PMT match.

### 3.2.3. Wireplanes signal reconstruction

The TPC wire data is the waveform readout of the 53 248 individual wires. The first step of the wire signal processing happens online directly on the readout cards installed in the TPC online computers and aims at removing the coherent noise from the wires [128]. Only minimal further processing is performed online, which leaves more scope for reprocessing the raw data using improved signal processing tools. The recorded waveforms are in ADC count/tick units, where the amplitude of the signal is expressed in ADC counts and the time information in ticks, each corresponding to 0.4  $\mu$ s in the ICARUS TPC timing. Figure 3.5 shows a sample of the data collected by the three planes, exhibiting the characteristic bipolar shape for the two induction wire planes and a unipolar signal for the collection plane.

In order to deconvolve the TPC wire signal from the deformation induced on the true signal by the electric field effects and shaping effects coming from the front end elec-

tronics, three major steps are addressed in *Stage0*: 1. the wire signals are deconvolved from the TPC electronic response functions, so that all three wire signal are also unipolar in shape; 2. the signal is analysed in order to define the region-of-interest (ROI) with a threshold-based algorithm; 3. each ROI is finally fit using a Gaussian function, whose area is proportional to the number of drift electrons generating the signal. Given the relevance of these steps of the processing chains, we will briefly describe them in the next paragraphs.

**Wire signal deconvolution** The wire signal shape can provide information on the deposited charge of drift electrons and thus on the deposited energy of the particle interacting in LAr. However, in order to extract the true signal from spurious effects, the effects related to the distortion of the true signal, due to the drifting electric field and the electronic response, must be deconvolved from the readout signal. The readout signal  $R(t)$  can be expressed as the convolution of serial effects of signal formation, electron propagation, electrostatic field response around the wires and processing by the DAQ to the true electronic signal, so that each wire channel response function can be factorised as

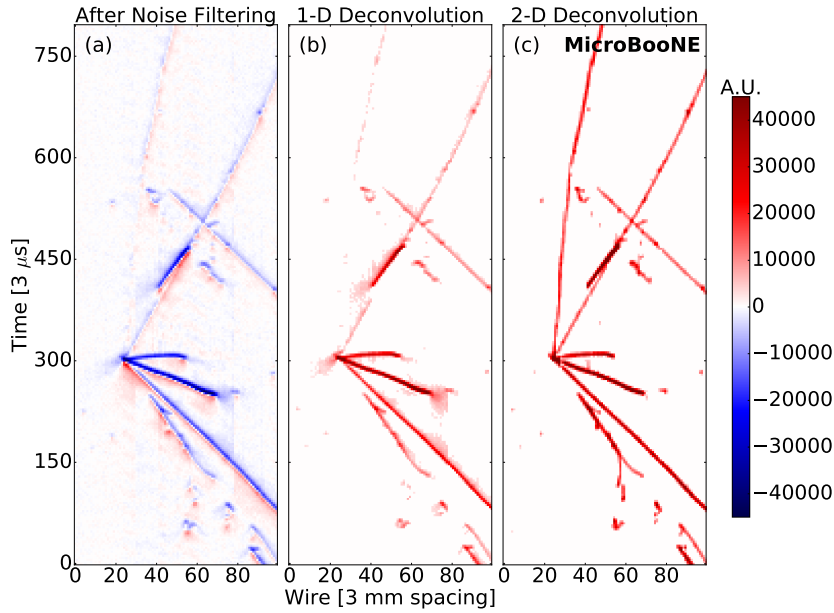
$$R(t, t') = \text{Ionization} \otimes \text{Recombination} \otimes \text{Diffusion and Attachment} \\ \otimes \text{Field response} \otimes \text{Electronic response} \otimes \text{Electronic noise} \quad (3.3)$$

In order to recover the desired ionisation electron yield, which is useful to measure the deposited energy per wire inside the detector as a function of time, it is necessary to unfold these effects.

The ICARUS experiment exploits a signal processing chain similar to other LArTPC experiments, performing a deconvolution in time of the signal waveforms. Ideally, after the deconvolution step, the signal pulse produced by a charged track on the wire would be Gaussian-shaped, with an integral area proportional to the deposited charge, i.e., a proxy of the energy, inside LAr. The signal recorded on the wires is the convolution of the response function  $R$  with the “true”  $S$  signal,

$$M(t') = \int_{-\infty}^{+\infty} R(t, t') S(t) dt; \quad (3.4)$$

Using the properties of the Fourier transforms, this can be written in the frequency domain as  $\mathcal{M}(\omega) = \mathcal{R}(\omega) \cdot \mathcal{S}(\omega)$ , which can be inverted to extract the true wire signal  $S(\omega)$ . This deconvolution, referred to as “one-dimensional” deconvolution, is currently employed in most of LArTPC detectors. This assumes that the charge distribution on



3

**Figure 3.6.** Example of the effect of signal processing using the one-dimensional deconvolution approach employed in ICARUS (b) with respect to the noise-filtered data (a). Figure (c) shows the same event using a two-dimensional deconvolution approach, i.e., performing the deconvolution both in the time direction as well as in the direction of the wires. Picture taken from [130].

each wire is independent from the charge distribution on the wires in its vicinity. However, as shown in [130, 131], it was demonstrated that this is not always true. Furthermore, while in general accounting for this effect implies small additional corrections to the overall deposited charge, there are cases where wire channel correlations are non-negligible. For example, for isochronous tracks (i.e., tracks lying parallel to the wires, which is frequent for the induction-1 wires given the specific ICARUS geometry), nearby wire channel correlation effects can create destructive interference patterns.

In [130, 131] a solution to this issue is presented: it consists in the application of two-dimensional deconvolution techniques where both time and wire channel are taken into account. This provides a strong and computationally efficient method to better extract the distribution of ionisation electrons. Figure 3.6 shows the result of the 1D and 2D approaches as tested by the MicroBooNE experiment. Efforts aimed at adapting two-

dimensional deconvolution techniques to ICARUS TPC raw data and testing their impact on the reconstruction performance are currently ongoing. Preliminary results indicate a remarkable enhancement in reconstruction efficiency specifically for track-like particle trajectories.

**ROI finding** After the deconvolution, we need to identify interesting regions of the TPC wire signals as a function of time. With a threshold-based algorithm we find the interesting regions (ROIs) to look for the signal hits, i.e., segments of waveform corresponding to the signal. ROIs can be actually relevant to iteratively improve the performances of the 1D/2D deconvolution steps by minimising the time-domain region over which the deconvolution is performed. Once ROIs are identified, a baseline value in ADC counts can be assigned to all the remaining times in the waveform, thereby drastically reducing the size of these data products inside the data files.

**Gaussian Hit creation** Upon the identification of ROIs, the final step is the creation of the *Hits* objects. A *Hit* is a two-dimensional object representing a cluster of electric drift charges, arriving at a certain time on a certain wire. The hit-finding algorithm runs under the assumption the distribution of the drift charges is Gaussian. Operating on the deconvolved ROI segments of the waveforms, it tries to fit one or multiple Gaussian distributions onto the signal shape. The parameters derived from the Gaussian fit are properties of the hits and include the area under the Gaussian(s), its mean and FWHM of the distribution and its multiplicity, i.e., the number of gaussians fitted to the signal. The area corresponds to the cumulative charge deposited by the electrons and is proportional to the deposited energy inside the detector; the mean and the FWHM represent the hit peak time and its width.

At this point, a collection of 2D hits for each plane of wires is available. For each reconstructed event, the three 2D views of the planes are stored and used as input for the event reconstruction taking place inside *Stage1*.

### 3.3. TPC event reconstruction

*Stage1* is dedicated to performing the high-level event reconstruction, taking the so-called *hit* objects created by the modules of *Stage0* and transforming them to build the full interaction picture. This part of the event reconstruction interests primarily the information extracted from TPC and PMT sub-detectors, since it is expected for most neu-

trino interactions ( $\sim 80\%$ ) to be contained inside the LAr volume, hence not expected to generate a CRT signal.

To perform the event reconstruction inside the TPC, the starting point is given by the three collections of 2D hits created in *Stage0*.

The hit-finding algorithm, providing the collections of 2D hits, is optimised to prefer efficiency over purity, reaching an efficiency greater than 99%; this might, however, lead to the creation of non-physical hits, especially in very noisy regions, that might cause failures in the pattern recognition steps that follow. To prevent such problems, the collection of 2D hits produced by the hitfinding algorithm are filtered using the *Cluster3D* algorithm. This preliminary step of the *Stage1* reconstruction runs over the set of wires of the three planes and, exploiting the common  $x$  drift coordinate, looks for time-correlated hits across the three planes. If matches are not found, or hits are isolated, then they are filtered out. The resulting filtered collection of hits is used as the input for the subsequent high-level reconstruction tools that include, in the context of the ICARUS experiment, Pandora topological reconstruction [132] and SPINE machine-learning-based reconstruction [133].

Pandora has been the baseline for the event reconstruction within the SBN program since the beginning of the activities. Pandora reconstruction chain takes the three 2D hits produced by the hit-finding algorithm as input, filtered by the cluster3D tool, performing a topological reconstruction of the tracks and showers taking part in the interaction to allow a hierarchical reconstruction of the neutrino candidate events. It specifically promotes the idea of a multi-algorithm approach to solving pattern-recognition problems. In this approach, the input building blocks (hits) of the processed events are considered by large numbers of decoupled algorithms. Each algorithm targets a specific event topology and controls operations such as collecting hits together in clusters, merging or splitting clusters, or collecting clusters in order to build a representation of reconstructed particles in the detector. The algorithms gradually build up a picture of the underlying events and collectively provide a robust reconstruction [132].

Recent inroads in Computer Vision (CV) and Machine Learning (ML) have motivated a new approach to the analysis of particle imaging detector data, and efforts within the ICARUS collaboration have been made to develop a machine-learning-based approach to the event reconstruction. SPINE (Scalable Particle Identification with Neural Embeddings) project serves this purpose. Unlike Pandora reconstruction, which starts from the 2D collection of hits on the readout planes, the SPINE reconstruction leverages a fully three-dimensional reconstruction starting from the 3D space points created by the clus-

ter3D algorithm. This way ambiguities that might arise in Pandora reconstruction are not present.

This thesis has the aim of performing a detailed validation study of Pandora-based event reconstruction, and so a more detailed description is given in the sections following subsection 3.3.2. SPINE approach to the event reconstruction is briefly presented and discussed in section 3.5.

### 3.3.1. Geometry of the ICARUS detector

Pandora reconstruction — as any reconstruction paradigm for LArTPCs would do — heavily exploits the geometry of the detector. Newer LArTPC detectors employ a common geometry to make it effortless to transition the software codebase from one to another. Being the first of its kind, and since its original physical scope extended beyond that of the SBN program, the ICARUS detector TPC geometry is unique. As already mentioned in section 2.4, and illustrated in Figure 2.6, ICARUS wire planes have some peculiarities. First, the wire orientation is different from other LArTPCs currently in use for neutrino experiments, including SBND and ProtoDUNE: for reasons related both to mechanical constraints and topological reconstruction, it is customary to build TPC wire planes with wires oriented  $\pm 60^\circ$  with respect to the vertical direction for the first two induction planes ( $u/v$ ), and have the collection ( $w$ ) plane wires vertical, whereas in the ICARUS detector the first induction plane features horizontal wires, and the second induction and collection planes are oriented  $\pm 60^\circ$  with respect to the horizontal. The reason for the horizontal wires was dictated by the target physics analyses for the ICARUS experiment at LNGS, especially for the detection of cosmic-induced particles. Due to mechanical limitations, however, it was not possible to have 18 m long wires kept at the tension needed for the detector operation, so they had to be split into two 9-metre-long sections [113].

The reference geometric parameter utilized by Pandora software during the 3D reconstruction of wire planes 2D projections is the orientation angle of the wire planes. This information is used to perform the spatial reconstruction of the hits collected in the different planes, using projective geometry. In Pandora each plane is associated with a so-called view, and each view has associated with it the angle at which wires are oriented. In most LArTPCs the mapping between views and planes is univocal. In the ICARUS TPC, however, the requirement to have the induction-2 and collection plane's wire angle oriented in the same direction if seen in the drifting direction (see, for refer-

ence, [Figure 2.6](#)) means that the mapping is not unique and depends on which TPC of each T300 module is being considered. As the association between the readout plane and view is not guaranteed in the ICARUS geometry, except for the induction-1 plane, there are some caveats with Pandora reconstruction. This is the case, for example, when the reconstruction assumes that the  $w$  view is the collection plane. For some steps of the current reconstruction, this does make handling the three different views inside the reconstruction harder; however, some preliminary solutions have been developed.

### 3.3.2. Pandora approach to the event reconstruction

As already anticipated, Pandora takes an innovative approach to the topological event reconstruction, splitting the problem of pattern recognition among the action of smaller, decoupled algorithms. Pandora framework is embedded inside *LArSoft* and accessed via the *LArPandora* module, which handles Pandora event reconstruction. The ICARUS detector consists of two separated T300 modules; thus, two parallel instances of Pandora reconstruction are run on each event, corresponding to the east and west cryostats. Each Pandora instance runs the full list of algorithms on the corresponding T300 module.

The inputs are the collections of 2D hits in the  $x$ -wire number plane, with  $x$  representing the drift time and the second coordinate being the wire number. The  $x$  coordinate is common across the views and thus is exploited to match the hits from different planes. The output of the pattern recognition algorithms are the Particle Flow Particles, or PF-Particles, objects; each PFParticle corresponds to a distinct track or shower and, through the action of subsequent algorithms, is associated with a list of 2D clusters, which are groups of hits on the same plane belonging to the same reconstructed object. Each PF-Particle is also associated with a set of 3D positions (named SpacePoints) corresponding to the reconstructed 3D trajectory and with a vertex position, defining its interaction point or its first energy deposition. Reconstructed PFParticles are finally arranged in a hierarchy, which identifies parent-daughter relationships for a given interaction candidate. For each interaction defined as neutrino-like, one empty PFParticle is created, identifying the neutrino PFParticle, and thus associated with the primary interaction vertex. [Figure 3.7](#) shows all data products produced by Pandora and their interdependency.

Three Pandora multi-algorithm reconstruction paths have been created for use in the analysis of ICARUS data: PandoraFastReco, PandoraCosmic and PandoraNeutrino. The last two are, as the names suggest, aimed at the reconstruction of precise interaction topologies; namely, PandoraCosmic is optimised for the reconstruction of cosmic-ray

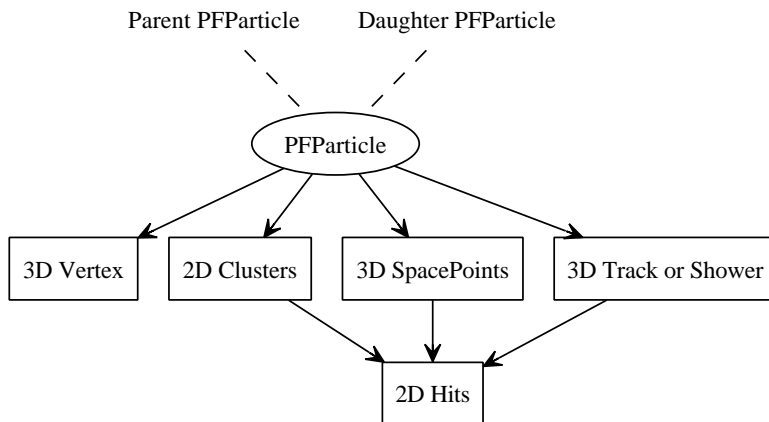


**Figure 3.7.** Pandora outputs data products. Navigation along particle hierarchies is achieved using the PFParticle interface, represented by dashed lines. Navigation from PFParticles to their associated objects is represented by solid arrows. Picture taken from [132].

muons and their daughter delta-rays, whereas PandoraNeutrino is optimised for the reconstruction of neutrino interactions. The PandoraFastReco path is run prior to both PandoraNeutrino and PandoraCosmic, with the precise aim of identifying and excluding from further processing steps *unambiguous* cosmic-ray muons, employing a faster reconstruction pipeline. The output of the PandoraFastReco path corresponds to a list of candidate cosmic rays. This list is then examined by a tagging module which identifies unambiguous cosmic-ray muons, based on their topological features, and removes their hits from the list. This enables an initial coarse separation of candidate signal events from background, thereby restricting the use of complex topological reconstruction algorithms to the most interesting events and reducing the overall computational cost of the reconstruction chain. Figure 3.8 illustrates the subsequent steps applied to each event by Pandora reconstruction.

### 3.3.3. PandoraFastReco: *unambiguous* cosmic hits removal

The first Pandora reconstruction path applied to the events consists of a set of tools aimed at performing a coarse reconstruction of all the hits identified during the read-out window. This way, long straight tracks coming from muons crossing the detector volume are identified. A list of “*unambiguous*” cosmic-ray particles is created, using

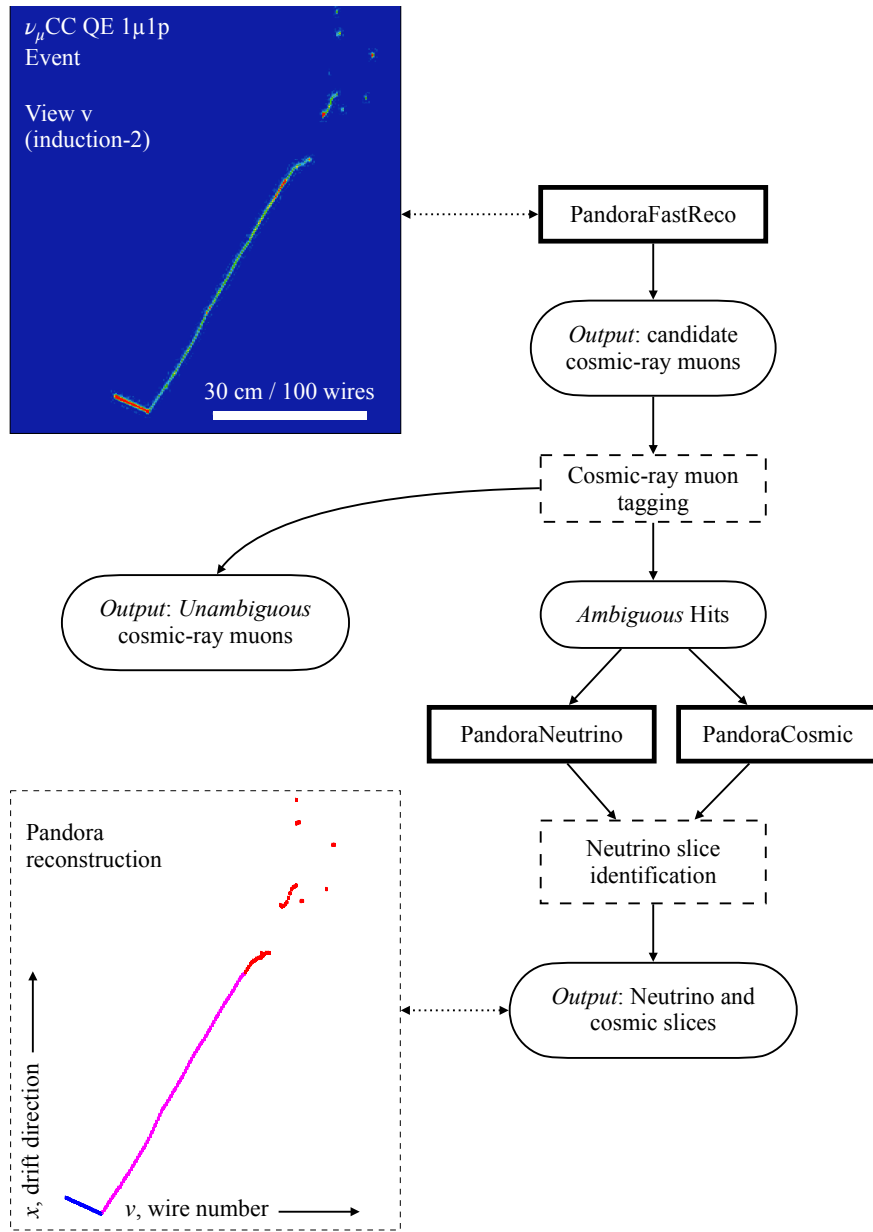


**Figure 3.8.** Illustration of Pandora reconstruction chain. Starting from a set of image-like collections of 2D hits, as shown in the event display in the top panel, the approach is to first address a fast and rough reconstruction (PandoraFastReco), aimed at removing the particles that are clearly cosmic-ray muons. Then each interaction inside the detector is passed through both PandoraCosmic and PandoraNeutrino chains to refine its reconstruction.

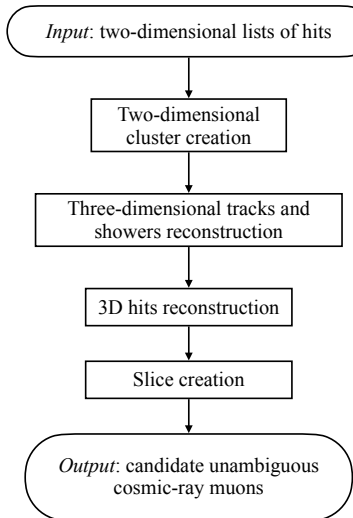


**Figure 3.9.** Illustration of the main steps of the PandoraFastReco path, which is applied as a first coarse reconstruction. This path aims at creating unambiguous cosmic-ray muon candidates that are then flagged and whose hits are excluded from further processing. Figure adapted from [132]

a classification of these reconstructed objects on the basis of topological considerations. The PandoraFastReco step shares most of the algorithms with the PandoraCosmic reconstruction path, since the goal is similar and entails the reconstruction of interactions characterised by a long straight track, usually crossing the full detector volume. The path, illustrated in Figure 3.9, is composed of four main stages, which are the subject of the next paragraphs.

### Two-dimensional reconstruction

The first step takes as input the three separate lists of two-dimensional hits, corresponding to the three views or wire planes. For each, the TrackClusterCreation algorithm creates bidimensional clusters of hits, representing continuous lines of hits. Bifurcations, kinks or any topological branch-like feature stop the creation of a cluster and start the creation of another cluster. This approach ensures that clusters of hits created at this level have high purity, meaning a high number of correctly associated hits at the expense of completeness, meaning that a single true particle could be split into multiple clusters.

At this point, cluster-merging algorithms identify associations between different 2D algorithms, improving the track completeness and affecting its purity in a minor way. Additionally, algorithms aimed at stitching together clusters that are split due to unresponsive wires or hits under the reconstruction threshold (that are not reconstructed) come into play at this level.

To improve purity, cluster splitting algorithms refine the selection by breaking simple clusters if topological features indicate that there are “spurious” hits inside the cluster.

### Three-dimensional reconstruction

After 2D clusters are created, they are collected together with the aim of creating groups of 2D clusters that represent the same individual track particle. The challenge these algorithms need to address is to identify consistent groupings of clusters from the different views. The 3D track reconstruction is performed by three main algorithms: the ThreeDTransverseTracks algorithm, the ThreeDLongitudinalTracks algorithm and the ThreeDTrackFragments. The former algorithm has the biggest impact on three-dimensional track reconstruction.

The ThreeDTransverseTracks algorithm identifies all the suitable combinations of clusters from the three readout planes and inspects these combinations to identify cluster-matching ambiguities. These ambiguities are then used to improve the 2D cluster iteratively and remove them. The groupings of three clusters from the three readout planes are created by exploiting the common  $x$  drift coordinate. On each view sliding fits are performed on the clusters; given a point on the  $x$  coordinate, then the position of the sliding fit on two of the three views can be extracted, for example, the position on the  $u$  and  $v$  views. These positions, together with the coordinate transformation plugin, can be used to predict the position of the third cluster (in the example shown in [Figure 3.10](#), in the  $w$  view) at the same  $x$  drift coordinate. This prediction can be compared to the sliding fit position on the third view, and the same can be done with all possible combinations ( $u, v \rightarrow w; v, w \rightarrow u$  and  $w, u \rightarrow v$ ). By performing such fits, and therefore checking the possible groupings of clusters across the three views, connections between them are created. The goal is to make these connections unambiguous, i.e., no two unique clusters from the same view are associated with the same unique cluster on another view. As described in [\[132\]](#), multiple tools query the different connection types across the views. Once no ambiguities are observed in the sets of clusters, the algorithm passes a list of sets of two (or three) clusters from different views to the following algorithms. Two

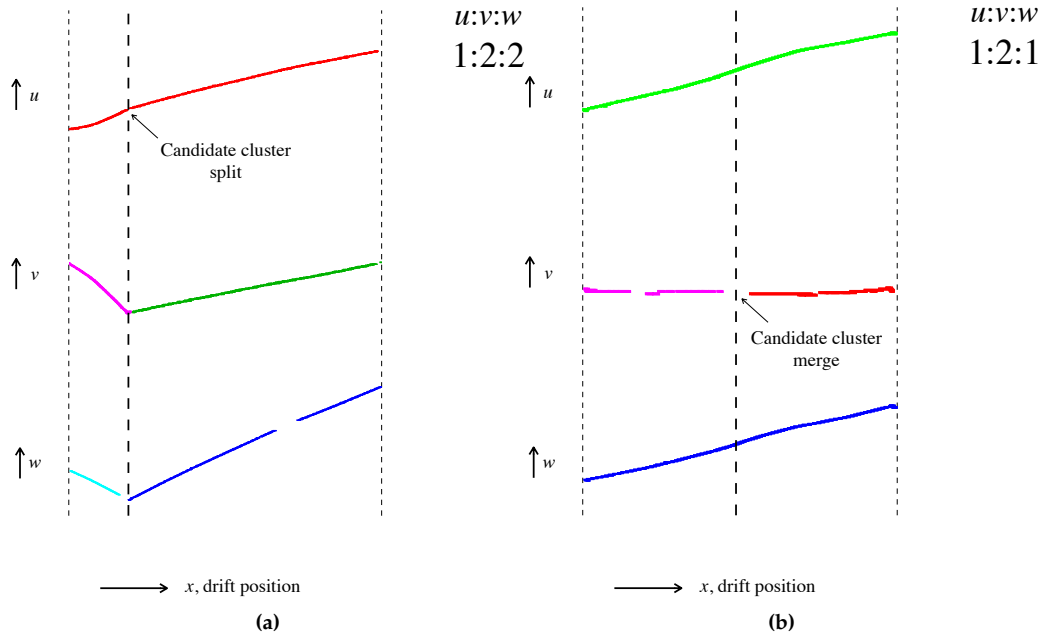


**Figure 3.10.** Example of two of the tools querying the 2D clusters' connections. (a) aims at resolving the ambiguities that arise from one view having two clusters merged into one. This ambiguity is resolved by splitting the cluster with the information from the other two views. (b) has the opposite role and has the goal of merging clusters erroneously split into multiple pieces at previous stages.

examples showing how these tools operate on the 2D clusters are shown in Figure 3.10.

### Three-dimensional hit reconstruction

At this point, the assignment of hits to reconstructed particles is complete, each particle containing hits from two or usually three views. For each 2D hit, a 3D point is created, with multiple approaches depending on the cluster topology. In all cases, the common step is the minimisation of a  $\chi^2$ -like value to get the best  $y, z$  values for a given  $x$  coordinate.

After the 3D hit creation, candidate muon cosmic-ray particles are created, and they are tagged to filter out hits belonging to the unambiguously cosmic-ray particles. The remaining filtered hits are passed to subsequent paths of the reconstruction, namely

PandoraCosmic and PandoraNeutrino.

### 3.3.4. PandoraNeutrino: topological neutrino event reconstruction

A key requirement for the PandoraNeutrino reconstruction path is that it should be able to deal with the presence of cosmic-ray muon remnants. The approach to address this problem is therefore to run the same 2D clustering, 3D cluster matching and 3D hit reconstruction described in subsection 3.3.3. After this path is run, 3D hits are divided into *slices*, which are separate lists of clusters of lists, using proximity-based metrics. For a given event, the idea is to isolate the candidate neutrino interaction from any leftover cosmic-ray-induced tracks. The original 2D hits associated with each slice are then used as an input to the dedicated neutrino reconstruction, which is described in this section.

The PandoraNeutrino dedicated reconstruction (shown in its entirety in Figure 3.11(b)) begins with a track-oriented clustering algorithm and a series of topological algorithms. Before processing the 2D clusters, the interaction vertex is reconstructed.

#### Three-dimensional vertex reconstruction

The reconstruction of the neutrino interaction vertex proceeds via two steps. Firstly, the CandidateVertexCreation algorithm creates a list of possible vertices. Comparing pairs of 2D clusters and ensuring that they belong to different views and have a certain overlap as far as  $x$  coordinate is concerned, the algorithm creates up to four neutrino vertex candidates for each 2D cluster pair, one for each endpoint of the 2D clusters.

After the identification of the candidate neutrino vertices, it is necessary to identify the most probable vertex candidate. This step is achieved by means of a BDT algorithm, which assigns each vertex a score. The vertex candidate with the highest score is finally selected as the correct neutrino interaction vertex.

The variables used to perform the classification and identify the most suitable vertex candidate include both properties of the reconstructed event and features of the candidate vertices. The former variables include the total number of hits, clusters and vertex candidates associated with the event; the fraction of hits likely originating from an electromagnetic shower based on cluster length and true associated particle; an estimate of the energy and of the 2D extent of the event, extracted from the total clusters span along  $x$  and  $z$  directions and an estimate of how longitudinal the event is with respect to the beam direction.

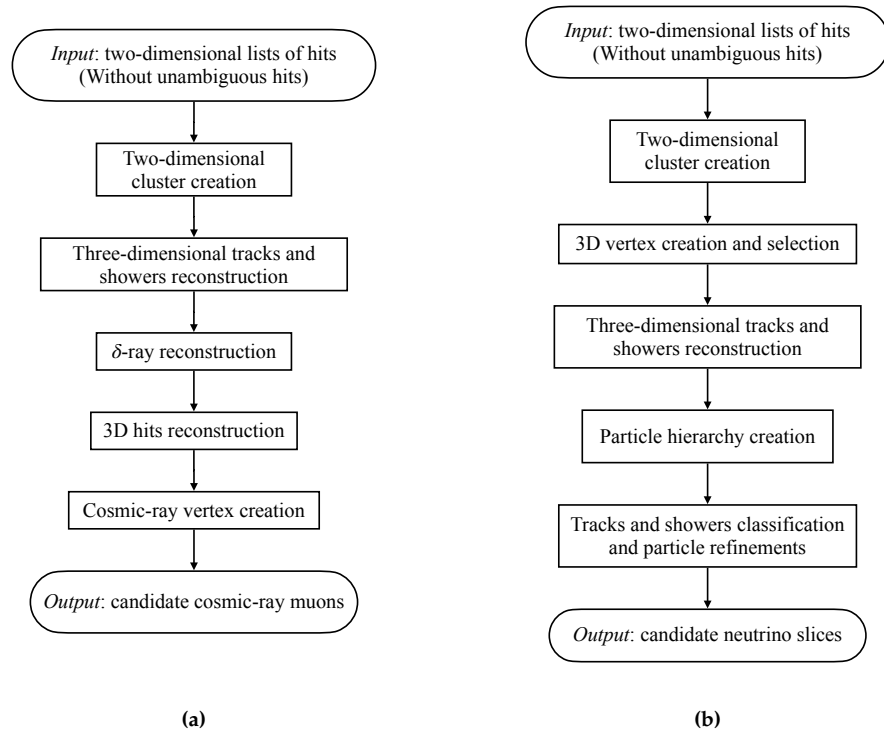


**Figure 3.11.** (a) illustrates the PandoraCosmic path, applied after the first fast reco pass, in parallel with the neutrino path. (b) illustration of the PandoraNeutrino reconstruction steps, applied to each slice in the event not tagged as cosmic-induced interaction. Figure adapted from [132]

This is the first of the three stages where machine learning techniques are employed within Pandora-based event reconstruction.

### Three-dimensional track and shower reconstruction

The PandoraNeutrino reconstruction, after the vertex creation stage, proceeds to reconstruct the three-dimensional tracks in the same way as described in previous sections. PandoraNeutrino, however, attempts also to reconstruct primary electromagnetic showers, arising from electrons and photons interacting in LAr.

Using a set of topological cuts, 2D clusters are first classified either as track-like or

shower-like. Existing track particles that are now deemed to be shower-like are dissolved to allow assessment of the cluster as a shower candidate. At this point, on each view, clusters representing shower branch candidates are merged. Showers are grown from the candidate shower spines, adding shower branches where association is plausible.

Following the 2D shower reconstruction, the ThreeDShowers algorithm builds the 3D hits in a similar way as for track-like particles.

After the 3D showers are finally built, a second pass of the 3D track reconstruction is applied to recover any inefficiencies associated with dissolving track particles to examine their potential as showers. Once both 3D tracks and 3D showers are consolidated, particle refinement algorithms try to improve on both hit completeness and purity, dissolving unassociated 2D clusters or, especially in the case of showers, adding 2D clusters that were left from previous steps of the reconstruction.

### Particle hierarchy reconstruction

After the 3D reconstruction, the next step in the PandoraNeutrino reconstruction is to organise the reconstructed particles into a hierarchy. This follows some subsequent steps, namely

- An object associated with the neutrino particle is created and associated with the 3D interaction vertex.
- The 3D reconstructed particles deemed to be associated with the interaction vertex are added as primary daughters of the neutrino particle.
- Further event ramification takes place by associating secondary particles (if any) to the existing primary daughters of the neutrino, e.g., a decay electron could be associated with a primary muon particle decaying in the active detector volume.
- 3D vertex position and particle trajectory endpoints are calculated for each of the particles in the neutrino hierarchy. This is the neutrino interaction vertex for primary particles, and the point of closest approach to their parents for secondaries

The last step of the PandoraNeutrino reconstruction handles the classification, by means of a BDT algorithm, of reconstructed particles as tracks or showers. The classification is performed relying on a set of topological and calorimetric variables. Dedicated work on this step of the event reconstruction was performed as part of a summer internship at Fermilab, and details are in Ref. [134].

### 3.3.5. PandoraCosmic: cosmic-ray muon reconstruction

In parallel with the neutrino-interaction reconstruction path, PandoraNeutrino, the PandoraCosmic path is also run, on the same set of hits, with the precise aim to reconstruct the remaining cosmic-ray interactions with greater detail compared to previous steps of the chain.

The PandoraCosmic path is very similar to the PandoraFastReco path since it aims as well at the reconstruction of clear cosmic-ray muon particles. The only differences are the lack of the slice creation step, unique to the PandoraFastReco path, and the addition of the delta-ray reconstruction stage. This specific reconstruction path is illustrated in [Figure 3.11\(a\)](#).

#### Delta-ray reconstruction

Unique to the PandoraCosmic path, before actually performing the creation of the 3D position inside the detector volume (see, for reference, [Figure 3.11\(a\)](#)), a delta-ray reconstruction step deals with any 2D clusters that have not been assigned to any reconstructed particle. The assumption for these algorithms is that these clusters likely represent fragments of delta-ray showers. The hits leftover from previous reconstruction steps are reclustered, and the between-views match is performed primarily exploiting the common  $x$  coordinate. Parent cosmic ray particles are identified via comparisons of intra-cluster distances.

## 3.4. Calorimetry and particle identification

Following the topological event reconstruction performed by Pandora’s set of algorithms, calorimetric information is computed with the use of multiple LArSoft modules.

Once 3D trajectories, made of 3D space-points, have been reconstructed, using the relevant quantities associated with the hits — hit area, hit time, and the track pitch length — the target is reconstructing the energy loss as a function of residual range, i.e.  $dE/dx$ , which is core to the subsequent particle identification. The energy loss is computed for each hit from the  $dQ/dx$ , expressed in ADC counts per centimetre. This in turn is obtained from the ratio of the area under the hit ( $dQ$ ) and the track pitch ( $dx$ ). The latter is computed using the direction of the track, taking into account that the wire pitch for the ICARUS detector is of 3 mm and thus  $dx = 3 \text{ mm} / \cos \gamma$ , where  $\gamma$  is the three-dimensional angle between the local direction of the track and the wire direction.

Calorimetry measurements require an accurate understanding of the charge response of the wires inside a LArTPC. The  $dQ/dx$  measured on the wires might substantially differ from the original  $dQ/dx$  at the location where the ionisation occurred; hence, it needs to be corrected before charge deposition is converted into energy loss. The process consisting in removing these charge response effects takes the name of “charge equalisation”. This process is done in three separate steps:

1. charge equalisation in the drift direction  $x$ ;
2. the equalisation on the wireplane direction  $y$  and  $z$ ; and
3. the equalisation across the four TPCs in the ICARUS detector.

Charge equalisation is performed using a dataset containing cosmic rays from off-beam events with muons crossing the LAr volume and leaving a signal in the CRT system.

The main effects that affect the  $dQ/dx$  in the ICARUS detector are

- Argon impurities: when electrons drift toward the anode, they can be captured by the electronegative impurities (mainly  $O_2$  and  $H_2O$ ). Since the electron attachment is modelled as an exponential decay, the measured  $dQ/dx$  is corrected as

$$\left. \frac{dQ}{dx} \right|_{\text{corrected}} = \left. \frac{dQ}{dx} \right|_{\text{measured}} \exp\left(\frac{t_{\text{hit}} - t_0}{\tau}\right), \quad (3.5)$$

where  $\tau$  is the electron lifetime. The electron lifetime measured in the ICARUS detector is in a range between 4 and 8 ms. For example, for the second ICARUS data-taking run, the electron lifetime was measured  $\sim 4$  ms for the East and  $\sim 7$  ms for the West cryostats.

- Drift field distortions: the ionisation process inside liquid argon, other than producing a plethora of free electrons, gives rise to Ar ions. They in turn contribute to the disuniformities of the drift electric field. Additionally, the ICARUS cathode plane is not completely flat, and this also produces disuniformities of the field. Absolute variations were found to vary from  $-6$  to  $13$  mm in the East cryostat, while the West cryostat reported values between  $\pm 9$  mm [99]. This impacts the electric field uniformity and results in a difference in the drift time of about  $\sim 8$   $\mu$ s.
- Diffusion: electrons do not drift following perfectly linear trajectories to the anodes but get diffused by elastic interaction in LAr.

Details on the countermeasures adopted to account for such effects are provided in [99].

As part of the calibration steps, to convert the  $dQ/dx$  into a deposited energy value, we need to take into account the fraction of electrons that survive the recombination process,  $\mathcal{R}$ , the amount of energy that is required to ionise an argon atom,  $W_{\text{ion}} = 23.6 \text{ eV}$  [48] and the electronic gain  $\mathcal{G}$  that converts ADC counts into the number of drifted electrons collected on the readout planes. With these details, it is possible to compute the  $dE/dx$  like

$$\frac{dE}{dx} = \frac{W_{\text{ion}}}{\mathcal{R} \cdot \mathcal{G}} \frac{dQ}{dx}. \quad (3.6)$$

From the reconstructed energy deposition per centimeter, it is possible to compute the full deposited energy like

$$E = \sum_i^{\text{all hits}} \left( \frac{dE}{dx} \right)_i \cdot dx_i. \quad (3.7)$$

Using the calorimetric information, it is possible to develop a  $\chi^2$ -like score that helps us identify the particle species. The underlying assumption is that, if the particle stops inside the TPC active volume, the  $dE/dx$  energy loss versus the residual range<sup>1</sup> is a means to distinguish charged particles. In the  $\chi^2$  score definition, the measured  $dE/dx$  for a given reconstructed track is compared, on a hit basis, with the average response predicted under different particle hypotheses from the Bethe formula, including protons, charged kaons, charged pions and muons as viable options. The PID score is defined as this value, divided by the number of hits in the track [99]

$$\text{PID} = \chi^2/\text{ndof} = \sum_{\text{hit}} \left( \frac{dE/dx_{\text{measured}} - dE/dx_{\text{theory}}}{\sigma_{dE/dx}} \right)^2 / n_{\text{hits}}. \quad (3.8)$$

where  $\sigma_{dE/dx}$  is an estimate of the resolution on the measured  $dE/dx$  per hit ( $\sim 3\%$ ) and was evaluated in dedicated studies by ArgoNeuT [135].

### 3.5. SPINE: machine learning particle identification

Inside the ICARUS collaboration, an effort to develop an ML-based end-to-end reconstruction chain started and has now reached a mature stage, at which the performances and the robustness of the tools allow for analyses to be performed. This approach, named SPINE (Scalable Particle Imaging with Neural Embedding) [133], consists of a

---

<sup>1</sup>Residual range is defined as the distance of an energy deposition within a track from the track's endpoint.

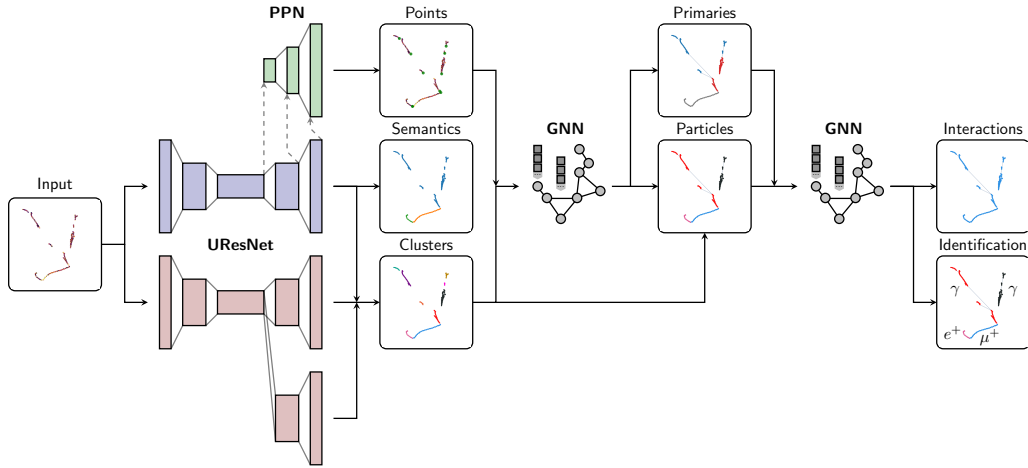


**Figure 3.12.** Schematic architecture of the end-to-end, ML-based reconstruction chain for LArTPCs. Picture taken from [133].

3

hierarchical set of neural networks that are part of an optimisable end-to-end reconstruction chain.

A schematic representation of the SPINE sequence is shown in Figure 3.12.

The starting point for the reconstruction are the three-dimensional space points processed by the Cluster3D algorithm. The hits that come out of the Cluster3D algorithm are passed through a UResNet architecture that aims at removing the so-called ghost hits. These are 3D hits resulting from an incorrect combination of 2D hits. Filtered positions are referred to as “deghosted” 3D space points.

The next step in the reconstruction chain is the classification of the deghosted 3D hits into categories based on the activity that produced them — tracks, electromagnetic showers, Michel electrons, delta rays and low-energy depositions. This algorithm (shown in blue in Figure 3.12) uses the same UResNet architecture as the previous step. In parallel with this (shown in red in Figure 3.12) is a similar algorithm that aims at identifying and building dense particle clusters. The two outputs are aggregated and then passed as input to the next steps of the reconstruction.

At this point of the SPINE reconstruction chain, groups of spacepoints corresponding to particle fragments have been identified, with semantic labels assigned to them. Then, a Graph Neural Network (GNN) aims at clustering these groups of hits into particles. Two functionally identical GNNs are employed, called GrapPA-Track and GrapPA-

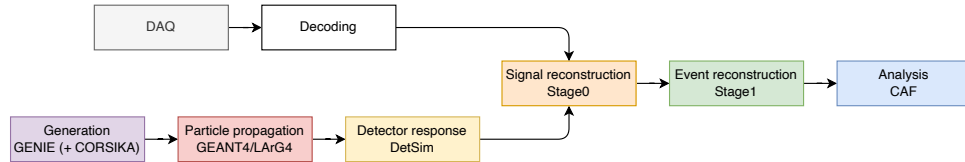


**Figure 3.13.** Complete processing flow for both data and simulation, from the collection/simulation to the final analysis.

Shower, targeting specific interaction topologies, namely tracks and showers. Details on the implementation and working principle of these algorithms are given in [133].

The final stage of the SPINE reconstruction is to cluster particles into interactions. A given interaction (equivalent to a Pandora slice) is a collection of particles originating from the same interaction vertex. Particles directly associated with the interaction vertex are called primary particles, whereas other particles are labelled as secondaries. In addition to the interaction clustering, the network is also tasked with predicting the particle type (photon, electron, muon, proton, or pion; see [136]). The architecture is still that of a GNN. The output of this network is represented by all the interaction primary particles, each with a list of secondary particles, all with their types.

### 3.6. Simulation of the full detector

The LArSoft framework that runs the full event reconstruction is also used to perform event simulation, from the generation of the interaction, performed using the GENIE Monte Carlo neutrino generator [137], to particle propagation inside the LAr volume, performed using the GEANT4 package, accessed through the LArG4 framework, to detector simulation, covering all the individual subsystems of the ICARUS detector. The output of the simulation is identical to the real acquired data collected by the detector and therefore can be used to perform Monte Carlo studies on the reconstruction pipeline. Details of the full event simulation are in [99], and Figure 3.13 shows a full overview of the entire pipeline both for real data, starting from the DAQ (above), to decoding and then signal processing and event reconstruction, as well as for simulated data (below).

# 4

## Validation and evaluation of the efficiency of the Pandora reconstruction for track-like event topologies

Pandora-based event reconstruction pipeline, as described in section 3.3, is central to the physics analyses conducted within the ICARUS and SBN collaborations. Its use across the LArTPC community ensures it is a set of tools that is actively maintained, improved and updated as new algorithms suitable for the event reconstruction are developed. Any improvement made by each collaboration sharing this tool is thus an improvement that can be exploited for analyses by other collaborations that rely on the same reconstruction tools.

Pandora framework in ICARUS employs the same structure inherited from the MicroBooNE collaboration, shared also with the SBND experiment. Especially important for the success of the SBN program is to have the same reconstruction infrastructure for both experiments in order to make systematic uncertainties related to the reconstruction as less relevant as possible. Recent efforts were made to better align Pandora reconstruction paths between ICARUS and SBND, with the inclusion of shower-targeted algorithms, aiming at increasing efficiency in the reconstruction of shower-like particle clusters.

Moving in the direction of improving the reconstruction performance for the ICARUS detector, this work focuses on the implementation of a set of tools that enable the use of true Monte Carlo information to alter the reconstruction output of the different stages. This comprehensive set of tools has already been tested and used in the context of the SBND reconstruction, as well as for other Pandora-based reconstruction pipelines

[138, 139]. These tools allow to investigate the impact of each step of Pandora reconstruction by altering the reconstructed objects using simulated events, where the true information derived from Monte Carlo is available. Using these altered reconstruction tools provides a strategy to validate the contribution of each algorithm to the entire reconstruction chain.

However, developing reconstruction improvements in isolation is difficult and does not always provide clear quantification of the impact made. Therefore, I focused my studies on a precise analysis in order to identify the pain points in the reconstruction process.

The ICARUS collaboration, using the collected data of the second physics data-taking campaign, performed as a standalone one-detector campaign, is moving towards a first oscillation analysis, preliminary to the two-detector oscillation analysis expected with the data collected by the SBN programme. This first analysis is targeted at studying the muon neutrino disappearance channel. The goals of this analysis are to contribute to world knowledge of potential eV-scale sterile neutrino oscillation in a timely way and to demonstrate the capability of ICARUS to produce high-quality physics results.

The  $\nu_\mu$ -disappearance analysis the collaboration is now conducting uses a precise event topology, namely the muon neutrino charged current quasi-elastic topology, with a single muon in the final state, any positive number of protons, zero visible electromagnetic showers (both from electrons and from photons) and zero charged pions. This selection is referred to as  $\nu_\mu$  CC Np QE [99, 140].

The chapter articulates as follows. The first section (section 4.1) is devoted to describing in detail the event selection and the data sample used to perform this work. The second section (section 4.2) delves into the details of the tools used for this work: what it means to “cheat” Pandora reconstruction and how it is performed for all the stages involved in the event reconstruction; this section is also devoted to validating the tools performance. The two final sections (section 4.3 and section 4.4) describe the methods followed to exploit the tools introduced in the previous sections to extract the performance of all the steps in the reconstruction and pinpoint the stages that require the most action.

## 4.1. Data sample and selection

The  $1\mu Np$  event topologies used in the muon neutrino disappearance study are selected automatically using a thoroughly tuned and tested selection procedure [140]. This sec-

tion provides a comprehensive description of the event selection procedure adopted for the present analysis, highlighting the decisions behind all the specific selection cuts.

**CRT-PMT match** Exploiting the CRT-PMT match [141] performed in the event reconstruction, non-contained neutrino interactions or cosmic-ray particles are rejected. The cut searches for coincidences in the 150 ns gate between CRT hits and an optical flash. Only optical flashes in the beam spill gate window [0, 1.6]  $\mu\text{s}$ , i.e. compatible with neutrino/beam-induced events, are considered. This first selection contributes to reducing the huge amount of cosmic ray interactions in the detector, thus slightly improving on the selection purity (+0.1 %)

**Optical flash barycenter match** The light information coming from the PMTs is also used to improve the selection by exploiting the 3D event reconstruction they allow. Using the light from the triggering PMT flash, the barycenter of the light hit is computed. The barycenter is computed as the mean of optical hits, weighted by the integral of the signal on each optical hit,

$$\vec{x} = \frac{\sum_i \vec{x}_i \times \text{PE}_i}{\sum_i \text{PE}_i}. \quad (4.1)$$

Here  $\vec{x}_i$  represents the position of the PMT producing the  $i$ -th hit, with a signal integral of  $\text{PE}_i$  photoelectrons collected by the  $i$ -th photomultiplier. Similarly is defined also the charge barycenter of a slice. Considering all the hits in one slice and weighting their position on the integral of the signal on each TPC hit, it is possible, with similar math to Eq. (4.1), to get the charge barycenter. This position information is used to reject from the event reconstruction all the slices, i.e. interactions, whose charge barycenter along  $z$  was more than 1 m away from the light barycenter along  $z$ . This cut was made to check compatibility between the event reconstructed in the TPC and the triggering flash in the PMT system; visual scanning efforts demonstrated that this choice very efficiently selected the neutrino interaction slice, while rejecting by a factor of 20 the contamination from cosmic rays crossing the detector outside the spill gate of the beam (“out-of-time” cosmic interactions).

**Vertex and tracks containment** Two basic selection cuts are then applied to the interaction vertex and tracks in the interaction selected by the former cuts. The vertex is required to be inside the fiducial volume (requiring more than 25 cm apart from the lateral TPC walls and 30/50 cm from the upstream/downstream walls, and an additional cut

to go around a dangling cable in the TPC volume) of the ICARUS detector, as outlined in detail in [99], whereas all the tracks inside the interaction are required to be contained in the active volume of the TPC within 5 cm from all the sides. This request ensures that the PID score described in Eq. (3.8) is correctly computed: for outgoing particles, the  $dE/dx$  versus residual range is not the same as for contained particles, since it is not defined where the track ends and thus the residual range is shifted; therefore a selection involving outgoing particles would require different metrics for computing the energy loss.

The interactions that pass these preliminary selection cuts are then analysed in terms of particle content, so each particle in the interaction is classified as such, and interactions with one muon,  $N$  protons (with  $N \geq 1$ ), zero charged pions and zero showers are selected. I will now define the variable cuts applied to identify each particle species.

**Muon identification** The muon candidate track is identified as the longest reconstructed particle fulfilling the following set of requirements

- It has to be tagged as a primary particle, so its parent has to be the neutrino associated with the interaction vertex.
- It has to be identified as a track-like object. The BDT implemented at the end of Pandora reconstruction chain [142] performs a topological classification of each object inside the interaction, assigning a “trackscore” value between zero and one. The more an object is “track-like”, the closer to one this score has to be. The requirement for muons is a trackscore  $\geq 0.5$ .
- The reconstructed muon length has to be greater than 50 cm (or equivalently to  $\sim 105$  MeV of energy).
- The track starting point has to be at a distance from the reconstructed vertex smaller than 10 cm.
- Finally, the PID information is considered (see section 3.4 and Eq. (3.8)). This sets the simultaneous requirement to have  $\chi_{\mu}^2 < 30$  (using the  $dE/dx$  energy loss under the hypothesis that the object is a muon) and  $\chi_p^2 > 60$  (using the  $dE/dx$  energy loss under the hypothesis that the object is a proton).

In the reconstructed interaction, only one muon is required, passing this selection.

**Proton identification** The identification of the proton follows similar cuts as for the muon

- The requirement to be tagged as a primary particle.
- Based on the track score distribution for protons, which, compared to muons, is slightly shifted towards lower values, a track score cut of 0.4 was set [142, 143].
- In order to select only events with visible protons where reconstruction is expected to succeed, a threshold of 2.3 cm is set on the candidate proton track length. This corresponds to an energy threshold of  $\sim 50$  MeV.
- The track starting point has to be at a lower than 10 cm distance from the reconstructed interaction vertex.
- PID is then considered, requiring that  $\chi_p^2 < 100$ .

Any positive number of protons is required in the present  $\nu_\mu$  CC Np QE selection.

**Pion identification** Pions are identified using very similar selection cuts as protons, with the only exception of requiring  $\chi_p^2 > 100$ , and a deposited energy of 25 MeV. Since pionless signatures are considered for the present analysis, if one or more pions are identified within a certain slice, the slice gets rejected.

**Electromagnetic shower identification** Electromagnetic showers produced by photons are identified by means of track score: everything with a value lower than 0.5, which is not classified as a proton (so  $\chi_p^2 > 100$ , among other cuts), is identified as an electromagnetic shower. If more than zero showers are reconstructed and identified in a given slice, the slice gets rejected.

The performance of the aforementioned selection have been evaluated [140, 144] by computing the selection efficiency and selection purity, respectively defined as

$$\begin{aligned} \text{Efficiency} &= \frac{\text{Selected signal}}{\text{True signal}} = 49\% \\ \text{Purity} &= \frac{\text{Selected signal}}{\text{All selected events}} = 84\% \end{aligned} \tag{4.2}$$

Here the “selected signal” are the reconstructed events that pass the event selection that are also selected as  $1\mu Np$  with the true signal definition, “true signal” the events that

meet the true signal definition, and “all selected events” the reconstructed events that pass the event selection.

The same selection, with minor changes related to the differences in the reconstruction paradigm, is applied also to data reconstructed with the SPINE framework, described in section 3.5. Using this reconstruction paradigm, the efficiency and purity values obtained are, respectively, of  $\sim 75\%$  and  $\sim 80\%$ .

In parallel with the progress of the analysis, as part of the validation of the tools employed, the efficiencies and purities listed before were tested by using the visual scan technique on a small subsample of the available data. This study confirmed the aforementioned values for both reconstruction frameworks.

## 4.2. Cheating Pandora reconstruction

The modular structure of Pandora reconstruction chain allows for great flexibility in the choice and hierarchical arrangement of the tools and algorithms involved in the reconstruction. As described in section 3.3, and pictured in Figure 3.9, 3.11a and 3.11b, a sequence of multiple algorithms is applied to the reconstructed hits, resulting in reconstructed objects. The steering of Pandora reconstruction chain is performed by XML configuration files where each algorithm is declared and configured. The typical implementation of a single reconstruction algorithm inside Pandora reconstruction framework (described in greater detail in section 3.3) is illustrated by the example of the TrackClusterCreation as shown below.

```

1 <pandora>
2 ...
3 <!-- TwoDReconstruction -->
4 <algorithm type = "LArClusteringParent">
5   <algorithm type = "LArTrackClusterCreation" description = "ClusterFormation"
6     ...
7   <InputCaloHitListName>CaloHitListU</InputCaloHitListName>
8   <ClusterListName>ClustersU</ClusterListName>
9 ...
10 ...
11 </algorithm>
12 ...
13 </pandora>
```

This modular approach of Pandora topological event reconstruction can be exploited to allow an algorithm to be replaced with a functionally identical algorithm performing the task with a different approach. This modularity is exploited also to develop tools, which are the core of this work, that, instead of relying on the actual tools to perform the reconstruction task, use the underlying Monte Carlo information. This approach, developed as part of Pandora reconstruction framework, is in this work referred to as “*cheating*” of the reconstruction. The powerfulness of this concept has been shown already with reconstruction studies in other experiments, where it is employed to pinpoint the “failure points” of the topological event reconstruction and understand the ceiling performance of Pandora reconstruction [138, 139, 145].

In practical terms, cheating one or multiple algorithms involves replacing the corresponding algorithm in the steering XML configuration file with the respective cheating counterpart [139]. For example, the configuration shown above, guiding the creation of two-dimensional clusters on the *u* view, is replaced by the `CheatingClusterCreation` algorithm, which performs the cheating of the cluster creation (which is the first step of both `PandoraCosmic` and `PandoraNeutrino` paths; see Figure 3.11), and is listed below

```

1 <pandora>
2 ...
3   <algorithm type = "LArClusteringParent">
4     <algorithm type = "LArCheatingClusterCreation" description =
5       "ClusterFormation">
6       ...
7     </algorithm>
8     <InputCaloHitListName>CaloHitListU</InputCaloHitListName>
9     <ClusterListName>ClustersU</ClusterListName>
10    ...
11  </algorithm>
12 ...
</pandora>
```

The action of cheating an algorithm can be regarded as ensuring the cheated reconstruction step has a 100 % success rate. Cheating different steps takes into account the action of each step of the reconstruction. For example, referring to the algorithm listed before, its cheated version ensures a flawless reconstruction of two-dimensional clusters on view *u* with a perfect match between truly generated and reconstructed hits. The

next paragraphs are entirely dedicated to delving into the details of how each of the algorithms acts upon the event and thus how cheating is applied specifically to them.

Given the  $\nu_\mu$  CC QE Np sample of events used for this study, the following sections are focused on cheating specifically the PandoraNeutrino reconstruction path. However, it should be noted that most of the algorithms that will be addressed in this section are also implemented in the PandoraFastReco and PandoraCosmic reconstruction paths: this highlights the true power of Pandora-based reconstruction pipeline, which allows for a large degree of flexibility.

#### 4.2.1. Two-dimensional clustering

The first algorithms in PandoraNeutrino reconstruction path aim at clustering the hits on each of the three readout planes. The TrackClusterCreation algorithm is involved in this step in the “nominal” Pandora reconstruction (i.e., without any cheating applied). It performs the clustering of adjacent hits representing continuous lines, operating only on topological features. Cheating this step is straightforward. Using simulated data, the hits on the three views,  $u$ ,  $v$  and  $w$ , are associated with a value called “MCWeight”, expressing the contribution of a given Monte Carlo particle in the interaction to the simulated hit on the readout plane. Using the MCWeights, it is possible to map the hits to the respective MC particle and thus build a cluster on each of the 2D planes using the simulation’s true information. The effect for tracks, like muons and protons, is noticeable but not striking, whereas the impact on electromagnetic showers is relevant, since this approach does not just cluster continuous lines of hits but, using MC association to the true underlying event, can group together hits in more complex topologies. Hence, the presence of the CheatingClusterCreation algorithm makes the contribution of some of the subsequent algorithms to the reconstruction of the event hierarchy irrelevant.

Like most of the algorithms used within Pandora framework, the CheatingClusterCreation algorithm is highly customisable, allowing only one view of the three to be cheated and also allowing only one type of particle to have its cluster created by using true information. Due to the ICARUS geometry and the details discussed in [section 2.4](#) (illustrated in [Figure 2.6](#)), the first option is only possible considering either the induction-1 plane (associated with the  $w$  view) and/or the induction-2 and collection plane together (associated with a mix of  $u$  and  $v$  views).

[Figure 4.1](#) illustrates the action of the cheated algorithm, showing the clusters created after a single pass of the TrackClusterCreation algorithm and the cluster created by the

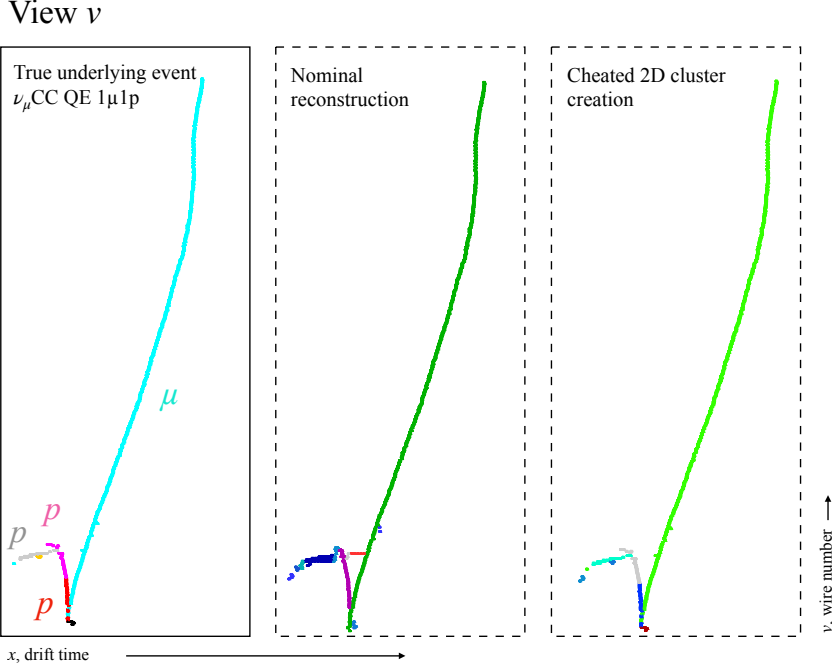


**Figure 4.1.** Illustration of the effect of the CheatingClusterCreation algorithm, with a  $1\mu 1p$  event. The reconstruction with the cheated cluster creation (shown in the last panel) is closer to the true underlying event (shown in the first panel). Also, compared to the “nominal” reconstruction (shown in the middle panel), the reconstructed interaction appears to have fewer noise hits associated and a more refined set of clusters.

CheatingClusterCreation algorithm. The effect, though very subtle, is noticeable, especially in the cluster refinements. A smaller fraction of noise hits are clustered together with particle hits, resulting in an overall improvement in the downstream reconstruction of the 3D particles.

To validate and assess the impact of the CheatingClusterCreation algorithm, we need to define a downstream reconstruction metric. Given that the TrackClusterCreation algorithm objective is to assign the correct hits to the respective track in each plane, two valid metrics are the *hit completeness* and *hit purity* scores. Given the hits on the readout plane, it is possible to define the MC matched hits, as the hits that are associated with

the true MC particle and are also associated by Pandora to the reconstructed so-called PFParticle

$$\text{Matched hits} \equiv \text{hits}_{\text{MCparticle}} \cap \text{hits}_{\text{PFParticle}}. \quad (4.3)$$

[Figure 4.2](#) illustrates this concept on an event with two particles. The reconstructed PFParticle  $j$  has a total of seven hits associated with Pandora reconstruction, whereas PFParticle  $k$  has six; the true MC particle  $j$  has nine hits and  $k$  has four. So for Particle  $j$  the matched hits are seven, and for particle  $k$  the number is four. If we introduce the definition of hit purity and hit completeness as

$$\text{Hit purity} \equiv \frac{\text{Matched hits}}{\text{hits}_{\text{PFParticle}}}, \quad (4.4)$$

and

$$\text{Hit completeness} \equiv \frac{\text{Matched hits}}{\text{hits}_{\text{MCparticle}}}. \quad (4.5)$$

we can say that for the case shown in [Figure 4.2](#) we have a purity of 100 % and 66.7 %, and a completeness of 77.8 % and 100 %, for the  $j$  and  $k$  particle, respectively.

Given the definitions of hit purity and completeness, we can use them to assess the impact of the CheatingClusterCreation on the event reconstruction. [Figure 4.3](#) illustrates both the hit purity and the hit completeness for a sample of  $1\mu Np$  events selected using the true signal definition [144], for both protons and muons involved in the process. Both hit purity and completeness spectra highlight an improvement in the case of the cheating compared to the nominal 2D clustering algorithm.

However, there is a non-zero fraction of events for which the muon completeness is lower than 0.4.

Visually scanning these events unveiled that two main issues arise:

1. Particles have poorly reconstructed hits on some of the wireplanes, making the correct association between views in downstream algorithms tough even if cheating the 2D clustering removes ambiguities at this level;
2. In some cases, the upstream slice creation fails and splits the muon into two or more slices. The slice that is reconstructed as a  $1\mu Np$  interaction and matches the truly generated one in these cases contains a muon with a smaller than true track length, resulting in a higher hit purity compared to the remaining slices but smaller than one hit completeness.

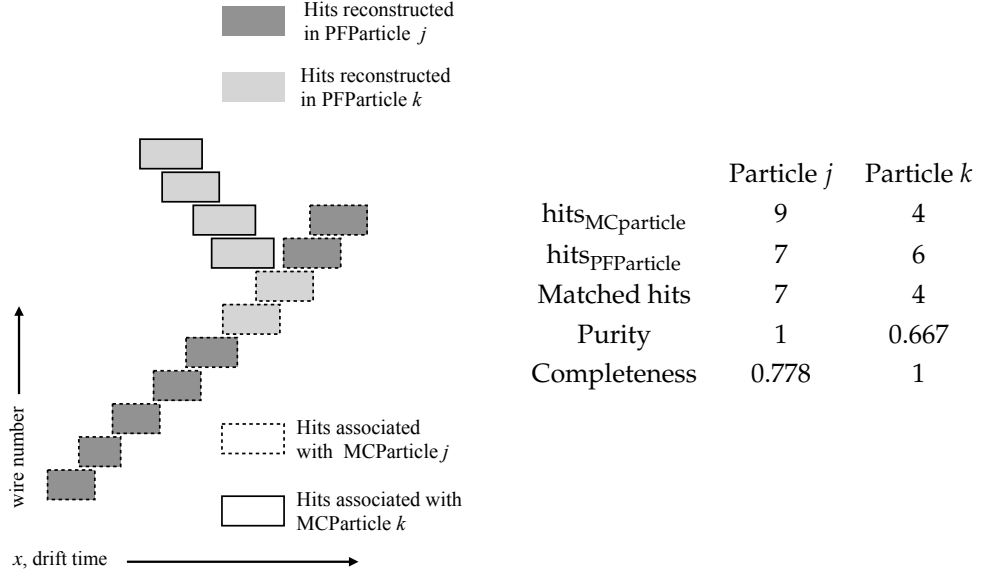


**Figure 4.2.** Illustration of the process of hit matching to truth information on an event with two true and two resulting reconstructed particles. More details are provided in the text.

This visual scanning reveals that it is very difficult to decouple the effects of the algorithms upstream in the event reconstruction from the algorithms downstream; since the hit purity and hit completeness metrics are computed downstream of the event reconstruction, these take into account all these effects and are not uniquely affected by the clustering performance. For instance, after the two-dimensional clusters are created, clusters are modified iteratively by the Overshoot- and UndershootTracksTool algorithms that help perform the 3D reconstruction. Similar clustering improvements are performed also before three-dimensional reconstruction is done, once the interaction vertex is created, and after 3D particle creation when the particle refinement tools are run. These downstream operations can cause a cluster to be split into multiple smaller clusters, thus creating multiple reconstructed particles that are matched to the same true particle, thereby undermining the impact of the 2D clustering cheating on the entire event reconstruction. By selecting all the particles that are truth-matched to a muon in the interaction, one recovers the entire muon track. So, it is evident that these events,

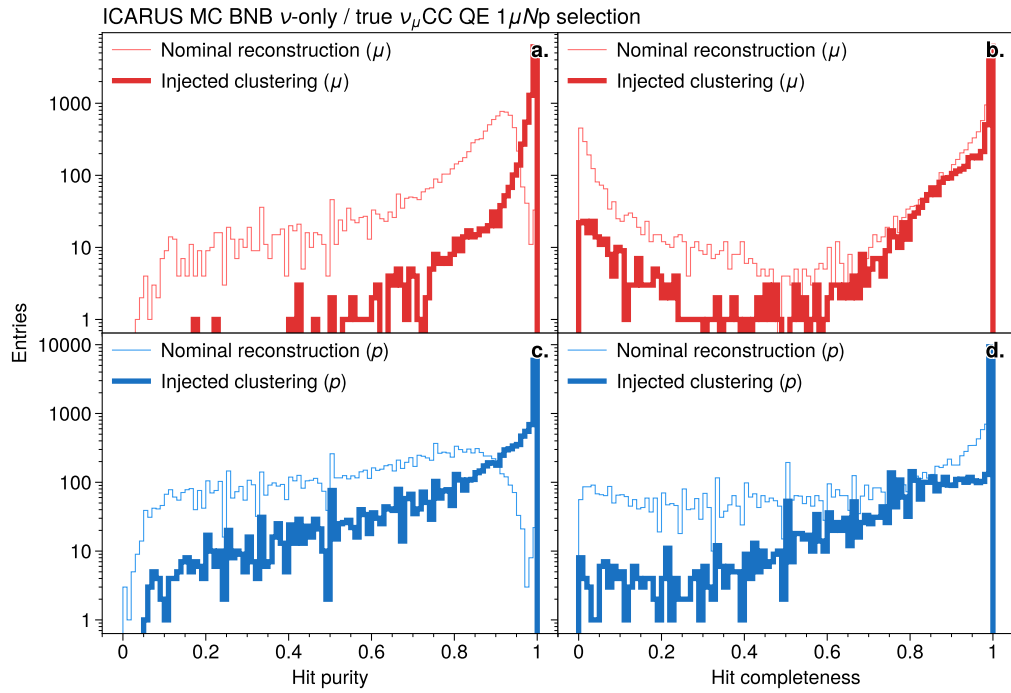


**Figure 4.3.** Hit purity and hit completeness spectra for the protons (blue) and muon (red) population, for both the cheated cluster reconstruction (thick line) and the nominal reconstruction (thin line).

showing a smaller hit completeness for both protons and muons, are not directly a result of an issue of the CheatingClusterCreation algorithm but more related to issues upstream (i.e., signal processing on the readout planes) or downstream (i.e., 3D reconstruction) of the CheatingClusterCreation algorithms. Comparing the hit completeness with the number of reconstructed hits on the collection plane, left and right plots in Figure 4.4, it is possible to double-check that low hit completeness values are related to a small number of reconstructed hits.

Figure 4.5 shows a case in which reconstruction issues are due to failure in the slice creation step, resulting in a less than 0.5 hit completeness for the reconstructed muon.

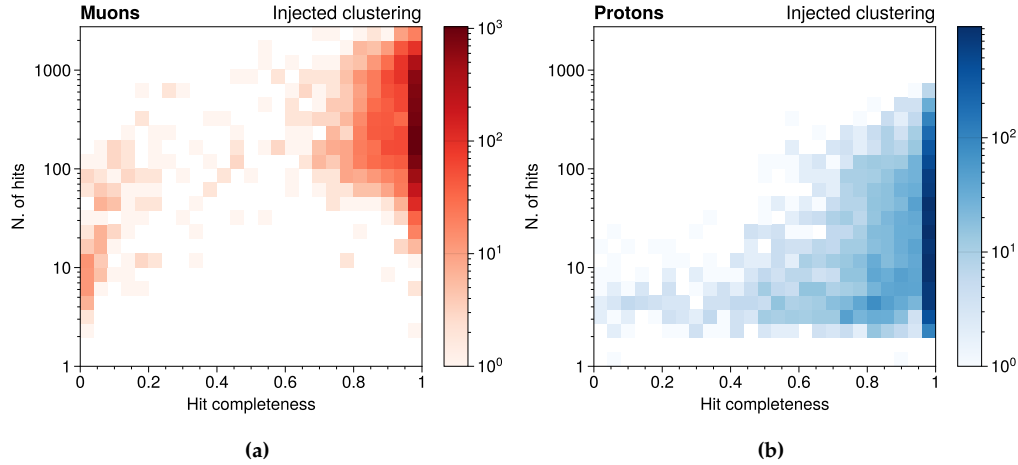


**Figure 4.4.** Number of hits reconstructed on the collection plane and associated with a reconstructed particle versus the hit completeness of the same reconstructed particle. The left plot shows the reconstructed particles associated with true muons, whereas the right one shows the same quantities for the protons. Both plots are generated for the case of performing the cheating of the cluster creation.

#### 4.2.2. Three-dimensional vertex

Recalling the description of the vertex reconstruction provided in section 3.3, two algorithms are mostly involved. The first, the `CandidateVertexCreation` algorithm, performs the creation of two candidate vertices for each 2D cluster created, comparing pairs of clusters from two different readout planes, therefore providing a list of all the “candidate vertices” in the interaction. The second, the `BdtVertexSelection` algorithm, selects from the list of candidate vertices the most probable interaction vertex, using a BDT algorithm and some geometric variables extracted from the clusters and the candidate vertices.

There are two ways true information can be used to inform the reconstruction of the interaction vertex. The most intuitive cheating mode is represented by the replacement of both steps in the vertex identification (candidates creation and final selection) with the assignment of the true 3D position of the interaction vertex from Monte Carlo simulation. This operation is performed by the `CheatingVertexCreation` algorithm that replaces all the vertex creation and selection algorithms in the XML steering configuration.

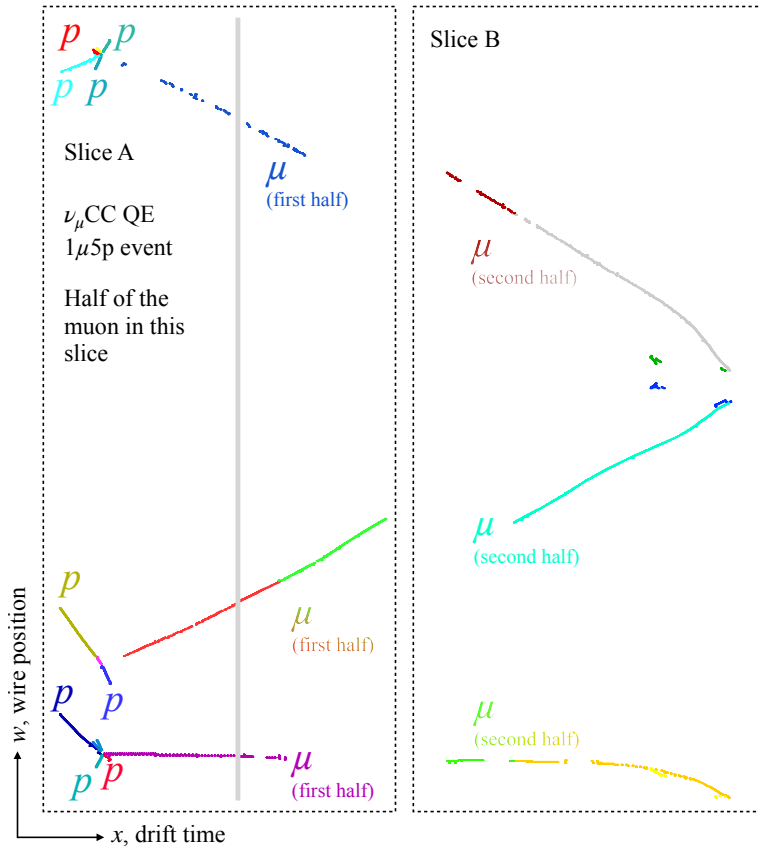


**Figure 4.5.** Example of an event for which the reconstructed muon completeness is lower than 0.4, i.e.,  $\mu_{\text{completeness}} \simeq 0.318$ . In this case the lower completeness is due to the true muon particle being split into two slices, of which only one (slice A) is reconstructed as corresponding to a  $1\mu 5p$  interaction and thus selected as a signal candidate.

Figure 4.6 shows an example of an event where the nominal reconstruction misplaces the interaction vertex. The event is a  $1\mu 1p$  event where the primary proton (short track) and the muon (long track) are produced nearly back-to-back. The muon decays in argon, thereby generating a Michel electron. Due to the topological features of the interaction, the vertex in the nominal reconstruction is placed at a distance of  $\sim 50$  cm from the true position. Using the CheatedVertexCreation algorithm, the correct interaction vertex is assigned, as shown in the right panel of Figure 4.6 where the true and reconstructed ver-

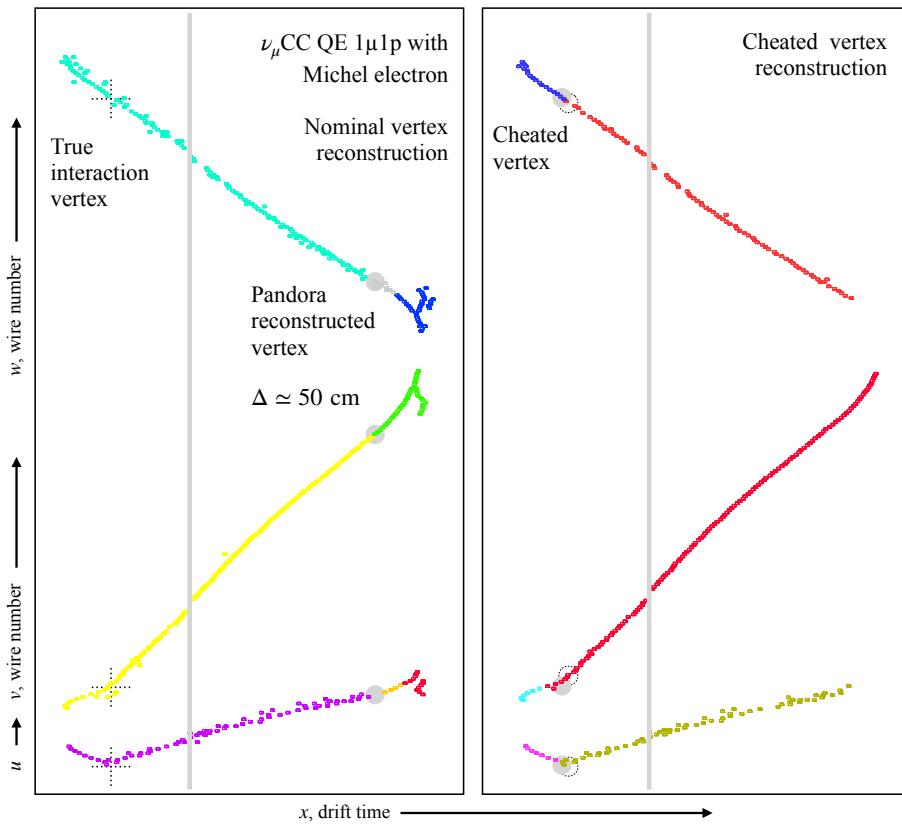


**Figure 4.6.** Illustration of the impact on Pandora reconstruction of the CheatedVertexCreationAlgorithm. On the left panel, showing the nominal vertex reconstruction, the true neutrino interaction vertex is shown by a dotted cross +, whereas the filled circle (o) indicates Pandora-reconstructed neutrino interaction vertex. In this case, vertex identification fails, resulting in a (3D) distance between true and reconstructed vertex of half a metre. In the right panel, the outcome of cheating vertex identification is shown, and, as expected, the filled circle matches the true interaction vertex. Additionally, the vertex selected by the CheatingVertexSelection algorithm is shown with a dashed circle.

tices coincide. It is worth noting that the impact of correct vertex reconstruction on the following steps of particle cluster creation is drastic: In the example shown in Figure 4.6, the proton (the particle on the left side of the vertex) is not reconstructed in the nominal case while correctly identified when the vertex reconstruction is cheated.

However, there are some caveats to take into account when evaluating vertex reconstruction performance. Since Pandora operates its algorithms on the reconstructed and filtered hits, it can only add vertices at the endpoint of 2D clusters. However, there are cases where the true interaction vertex position does not correspond to any reconstructed hits. This can happen in these three noteworthy cases:

1. the interaction vertex lies outside the active volume of the TPC, therefore not producing any signal in the wires in its vicinity;
2. the conversion gap (i.e., the distance of the first visible hit from the interaction vertex) for the final state particles involved in the interaction is large due to the underlying physics (for example, the production of a  $\pi^0$ , that is detected through the identification of two  $\gamma$  yielding electromagnetic showers in LAr);
3. the hits near the true interaction vertex are lost in the signal processing stage that takes place before Pandora performs hierarchy reconstruction upon the event.

In all these cases, cheating the vertex with the `CheatingVertexCreation` algorithm results in a vertex placement far from reconstructed hits on the three views. Pandora algorithms downstream of the vertex creation operate on the events and partially solve any ambiguity left by assigning the vertex to the closest hit in 3D space. [Figure 4.7](#) shows one of the mentioned cases. In this example, the simulated true vertex is outside the fiducial volume (hence out of the active TPC volume), and the candidate vertex reconstructed and identified by Pandora is highlighted yellow, far from the true position. It is worth remarking that events showing such problems (called *dirt events*) are excluded from the sample of events used in this work, by requiring the vertex to be contained in the fiducial region of the TPC active volume; therefore, such problems do not arise in future results.

A second point where the true Monte Carlo information can be used to inform the vertex algorithms, and thus a second possible cheating mode of the vertex identification, is the selection of the correct interaction vertex from the list of candidates created by the nominal `CandidateVertexCreation` algorithm. This operation essentially entails bypassing the BDT performing the choice and selecting, from the list of vertex candidates created as described in [subsection 3.3.4](#), the vertex which lies closest to the true interaction vertex. [Figure 4.6](#), on the right panel, shows the result of cheating the vertex selection (dashed circle).

Validating the cheating of the vertex reconstruction is straightforward: it is possible to check the distance of the true vertex with respect to the reconstructed vertex of the

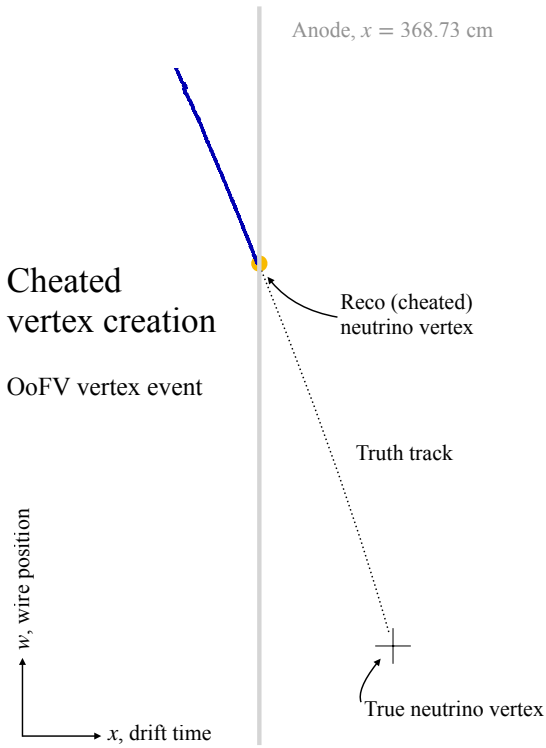


**Figure 4.7.** The illustration shows an example of events where the simulated vertex lies and the outcome of cheating vertex reconstruction. As discussed in detail in the text and expected, the position of the reconstructed vertex does not match the true one.

interaction. Figure 4.8 shows this for both the cheating of the vertex creation (thick black line) as well as the cheating of the vertex selection (thin black line), comparing the two cases with the distribution of the vertex distance when the nominal reconstruction is performed.

### 4.2.3. Three-dimensional track and shower reconstruction

The reconstruction of the 3D particles, starting from the 2D clusters created by upstream algorithms, as described in the subsections of section 3.3, is not trivial. It encompasses a large number of algorithms and tools: the starting point is the refinement of the two-

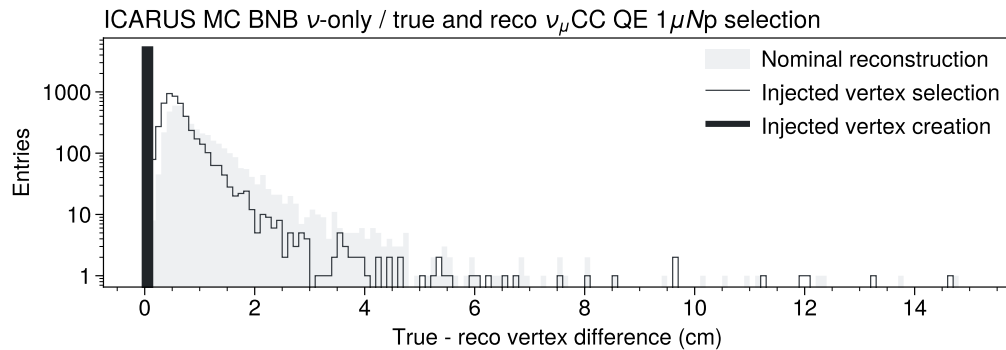


**Figure 4.8.** Displacement of the reconstructed vertex from the true vertex, evaluated in three cases: with the nominal vertex reconstruction (shaded area), cheating the vertex selection (thin black line) and cheating the vertex creation algorithm (thick black line).

dimensional clusters on different readout planes to remove any ambiguities (hits that have common  $x$  drift coordinate, that are from clusters of different particles) in order to create 3D clusters across the readout planes. Using the information from the different readout planes, together with the wire orientation, the 3D positions are computed, and the 2D clusters are projected into three-dimensional space.

Cheating the 3D reconstruction has a simpler structure: first, 2D clusters are associated across the readout planes by the CheatingPfoCreation algorithm; then, the ThreeDHitCreation algorithm performs the reconstruction of the 3D hits. This second step is the same as the nominal reconstruction: even though the interaction is generated in three-dimensional space, the simulation of the hits is performed only on the 2D readout planes, so there is no possibility to really inject the true  $(x, y, z)$  position of each hit, since it is not known a priori.

The CheatingPfoCreation algorithm goes through all the 2D clusters created by upstream stages of the reconstruction to identify the ones that share the same true MC particle. This operation is performed, similarly to the CheatingClusterCreation algorithm, exploiting the Monte Carlo weights associated with the hits in the cluster. For each MC particle in the interaction, the algorithm uses the MC weights to map the underlying particle to the deposited hits on the readout plane and then to the corresponding clusters on the different planes. Only clusters sharing more than 50 % of the hits with the underlying particle are associated with the correct particle; the other clusters (those that share less than 50 % of the hits with the MC particle) are discarded for three-dimensional

reconstruction. From these 3D clusters the 3D hits are reconstructed from geometrical considerations, as the nominal reconstruction.

It is worth noting that the CheatingPfoCreation algorithm does not alter in any way the output of the previous stages (unlike the nominal reconstruction, which implements the Under-/OverShootTracksTools to refine 2D clusters). Therefore, any issue of the reconstruction upstream of this stage is inherited and does impact the performance of this reconstruction.

In cases where a plane contains two ambiguous clusters, e.g., as a consequence of 2D clustering algorithms splitting in two parts a truly single cluster, only the cluster sharing the largest fraction of the hits with the true MC particle will be considered for the 3D reconstruction, thereby affecting the overall reconstruction efficiency and hit completeness for the particles involved. This is why the cheating of this step of the reconstruction is only performed cumulatively, and not as an individual module, as mixing nominal and cheating at this level might cause unrealistic reconstruction pathologies and thus bias the evaluation of the performance of these reconstruction steps.

To validate the effectiveness of cheating the three-dimensional cluster matching, the same metric used to evaluate the effectiveness of 2D cluster creation algorithms is used. This is illustrated in [Figure 4.9](#), where an improvement to the bare cheating of the 2d cluster creation algorithm (shown in the dashed line) is visible.

4

#### 4.2.4. Particle hierarchy reconstruction

The particle hierarchy reconstruction, implemented by three algorithms in the nominal Pandora event reconstruction, performs first the association between the primary particles and the interaction vertex. Then any leftover secondary particle is associated with its parent, and the vertex is computed using the distance of the daughter from the parent. Finally, all the daughters are associated with their parents, and the full particle hierarchy is saved.

The cheating of the particle hierarchy reconstruction, implemented by the CheatingNeutrinoCreation and CheatingNeutrinoDaughterVertices algorithms, aims at assigning the correct parent-daughter relationship to all reconstructed particles in the interaction. Using MC weights, it associates a reconstructed particle with the underlying MC particle that has the highest level of compatibility. Using this association, it then assigns the reconstructed neutrino interaction vertex to the particles identified as primary from the underlying MC particle. The same operation is then performed for secondary particles

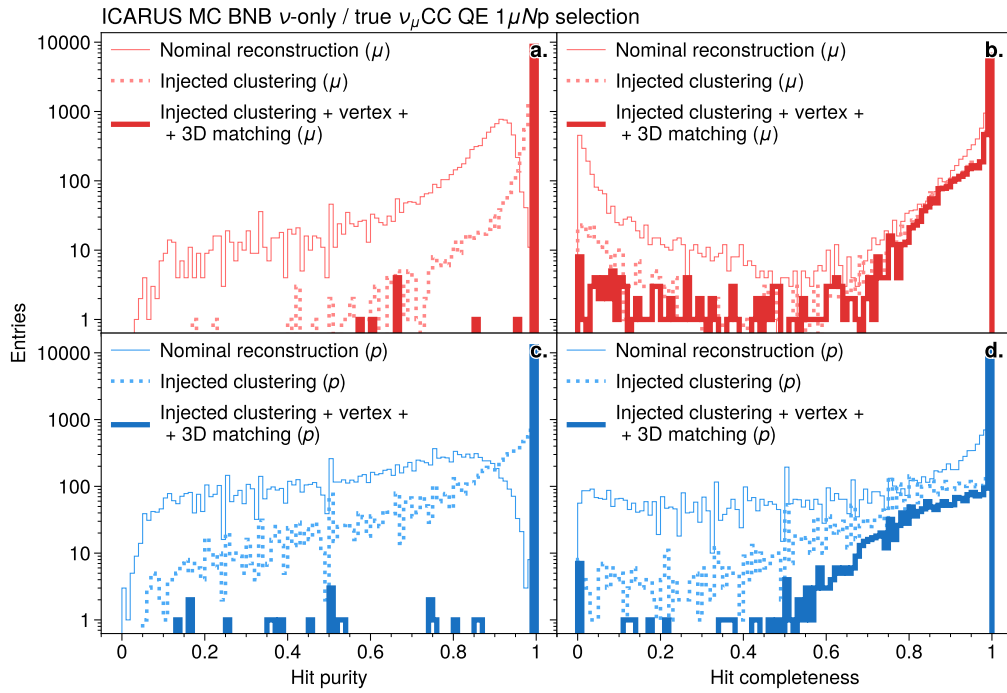


**Figure 4.9.** Hit purity and hit completeness spectra for the proton (blue) and muon (red) population when the nominal reconstruction is applied (thin line), when the 2D clusters are cheated (dashed line) and when all the steps up to the 3D cluster matching are cheated (thick line).

in the interaction: daughter particles are associated with their parents, and secondary vertices are created.

Since this step takes place downstream of the reconstruction chain, its performance is highly impacted by the outcome of previous stages, and extracting a reliable estimate of its effectiveness is not an easy task. As for previous algorithms, its capability to provide a reliable result depends on the upstream reconstruction stages, since the MC particle-reconstructed particle association is performed using the MC weights: if a MC particle gets split into two or more reconstructed particles, only the particle sharing the largest fraction of hits will be assigned the correct parent-daughter hierarchy.

Ideally, assigning the correct parent-daughter matches would result in more primary particles identified with this label. Also, a greater purity of the events selected should

be observed: no contamination from reinteracting particles that are not individually reconstructed should be present. Thus, for the  $\nu_\mu$ CC QE Np analysis, cheating the particle hierarchy should result in the proton multiplicity in the event being assigned correctly. [Figure 4.10](#) shows the comparison of reconstructed and true proton multiplicity, highlighting that if the reconstruction is cheated all the way up to the particle hierarchy creation, as shown in [Figure 4.10\(b\)](#), the diagonal is more prominent with respect to the nominal reconstruction, shown in [Figure 4.10\(a\)](#).

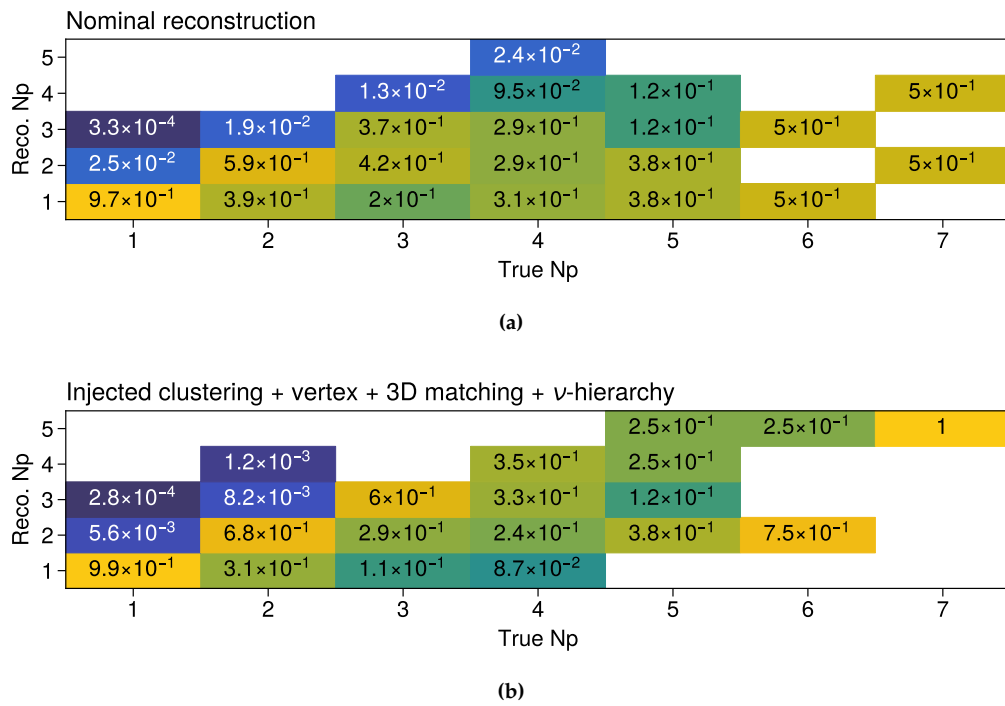


**Figure 4.10.** Reconstructed versus true proton multiplicity distribution. All the numbers are normalised with respect to the true number of protons in the interaction, i.e., normalised on a column basis. These plots show that when all the steps of the reconstruction up to the particle hierarchy creation are cheated, more events are assigned the correct number of primary protons.

This step is, however, delicate; hence, some remarks are mandatory to give a correct interpretation to the action of cheating in this specific case. Firstly, although correctly assigning the particle hierarchy is crucial for the downstream event selection, it is not the

only factor that affects it, as the multiplicity of the reconstructed protons highly depends on the efficiency of the particle identification. Furthermore, in [Figure 4.10\(b\)](#) there are some cases, especially when the proton multiplicity is higher, where the reconstruction fails to identify the associated hits. This is due to the fact that, for a certain interaction energy that is fixed to the value of the incoming neutrino (peaked at 800 MeV), a larger number of protons in the final state will imply a smaller amount of energy for each of them and thus a more complex topology to disentangle from noise. This in turn will make hit reconstruction on the wireplanes more difficult. Finally, given the event selection cuts presented in [section 4.1](#), two aspects are noteworthy:

1. The present selection strongly relies on this step, since it requires both the muon and the protons identified within the interaction to be primary particles, as well as ensuring that any other particle identified as belonging to a different species is not primary in the interaction.
2. Since a proper separation of secondary particles from primaries is known to be delicate in Pandora reconstruction and having secondaries collapsed onto primary particles is a common failure mode, the event selection for the present  $\nu_\mu$  oscillation analysis was tuned accordingly. This is why in the event selection the requirement for the primary protons to have at least 50 MeV of deposited energy was extended, at the truth level, to include also all their daughter particles, since in the reconstructed final states such behavior is expected.

These conditions, especially the latter, basically imply that the event selection does not rely on the creation of the particle hierarchy. Therefore, altering this step by injecting the true MC information to improve its performance, does not necessarily have a proportional impact on the reconstruction and selection efficiency. In reality, the interplay between how the nominal algorithm and its cheated version work causes some events that are selected with the nominal particle hierarchy creation algorithm to be lost due to misidentification in downstream event selection.

The issues preventing the correct reconstruction of the particle hierarchy and the correct identification of the interaction in some cases are multiple. Here we highlight two of the most common cases:

- o There are cases where all the particles in the final state are reconstructed, but where the prompt protons do not fulfill the selection requirements. Take for example [Figure 4.11\(a\)](#). In this case, the truth says that the prompt proton and its daughter

particles add up to a deposited energy  $E_{\text{dep}} > 50 \text{ MeV}$  (therefore a proton longer than 2.3 cm). However, if the reconstruction is cheated up to the particle hierarchy creation, the reconstructed prompt proton (alone, without its daughters) is shorter than 2.3 cm (or equivalently deposits less than 50 MeV. Therefore, even if the event is a signal event, it is not selected, lowering the efficiency. However, such events are selected when performing the cheating up to the stage that performs the three-dimensional reconstruction, since Pandora (mis-)identifies the daughter proton of the prompt proton reinteraction as a primary particle.

- Another case is represented by events where the prompt proton produces visible hits only on one readout plane. This happens e.g. for very short prompt protons that reinteract in LAr, producing a daughter proton. [Figure 4.11\(b\)](#) illustrates this failure mode with an example. In this case, the prompt proton is not reconstructed (as Pandora requires at least two planes to perform a three-dimensional reconstruction). If the particle hierarchy creation is left “uncheated”, its daughter particle gets assigned as a primary particle of the interaction vertex. When the particle hierarchy is cheated, the correct hierarchy is assigned, and this results in an event with no primary proton ( $1\mu 0p$ ) that is rejected by the selection.

After specific tests to better understand how particle hierarchy algorithms and their cheated version work, and considering the pathological cases partially due to the event selection used for the present analysis, we decided to keep the nominal version of this stage in the reconstruction chain.

#### 4.2.5. Particle classification

The last step of Pandora neutrino reconstruction path, aimed at classifying particles into tracks or electromagnetic showers based solely on topological and calorimetric features, can be cheated in two different ways.

The easiest way entails simply referring to the Particle Data Group (PDG) label, uniquely identifying each MC particle with a label and assigning it correctly to the reconstructed particle. This is the strategy that was originally implemented as part of Pandora cheated reconstruction chain but is not useful for the present work, since the event selection for the  $\nu_\mu$  CC QE Np ICARUS analysis does not rely on this information but instead makes use of the track/shower classification BDT score that is produced by the nominal reconstruction algorithm. So another way of cheating this stage of the reconstruction was

**(a)** illustrates one event where the primary (prompt) proton is shorter than the lower threshold of 2.3 cm or equivalently 50 MeV of deposited energy. This event is therefore not selected if the daughter proton of the prompt proton is assigned the correct parent-daughter hierarchy, like when performing the cheating of the particle hierarchy. **(b)** illustrates the case where the prompt proton is not reconstructed due to missing information on some of the readout planes. This event is not selected since the secondary proton, daughter to the prompt proton, is not identified as primary when the particle hierarchy is cheated.

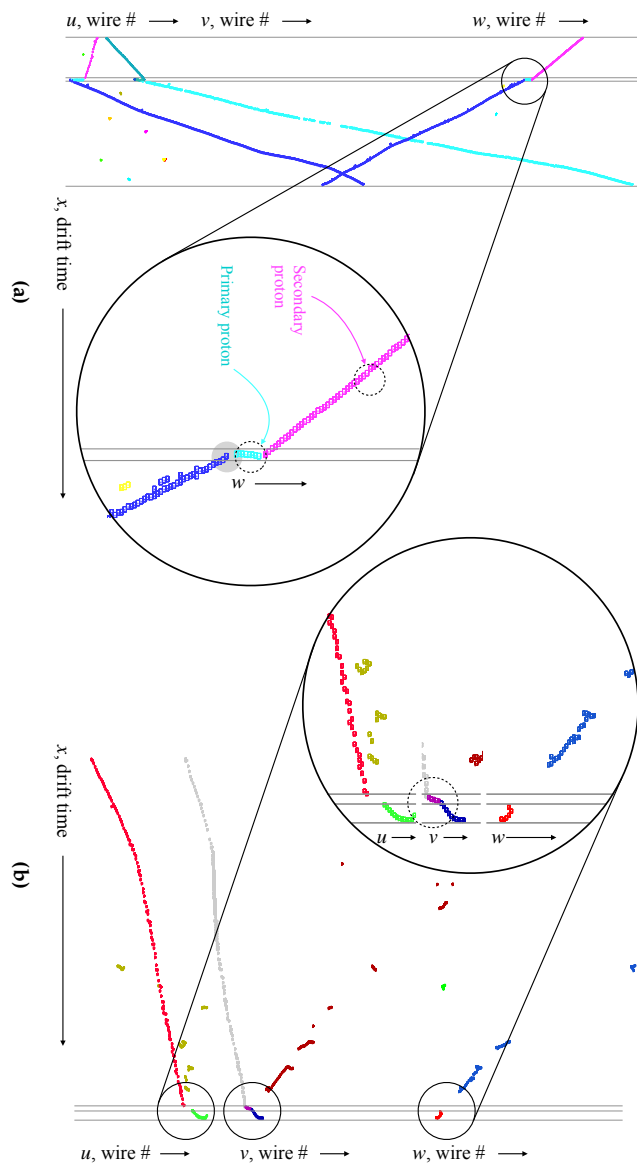


**Figure 4.11.** **(a)** illustrates one event where the primary (prompt) proton is shorter than the lower threshold of 2.3 cm or equivalently 50 MeV of deposited energy. This event is therefore not selected if the daughter proton of the prompt proton is assigned the correct parent-daughter hierarchy, like when performing the cheating of the particle hierarchy.

**(b)** illustrates the case where the prompt proton is not reconstructed due to missing information on some of the readout planes. This event is not selected since the secondary proton, daughter to the prompt proton, is not identified as primary when the particle hierarchy is cheated.

implemented as part of this work. This implementation uses the true PDG label associated with MC particles to cheat the value of the BDT track score, effectively making the track-shower separation perfect.

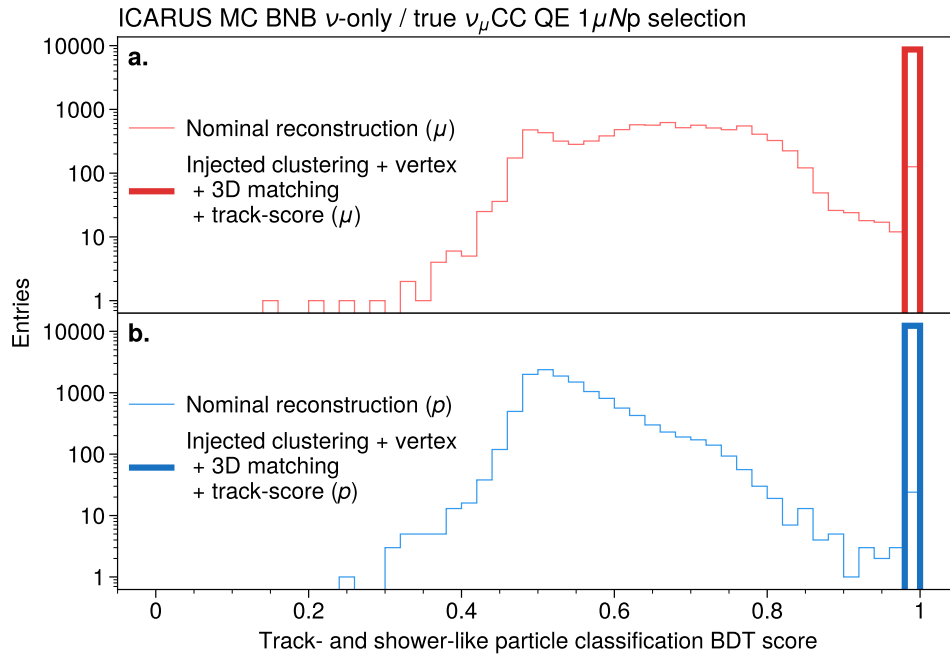


**Figure 4.12.** Plot of the score resulting as output of the track and shower BDT classification algorithm. Track-like particles should have a score of 1, whereas electromagnetic shower particles should have a score of 0. In the two panels we show muons (upper half, in red) and protons (lower half, in blue) with both the nominal reconstruction (thin line) as well as the cheated reconstruction and classification (thick line).

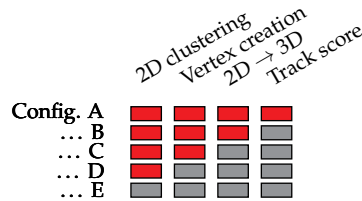
Checking this stage is straightforward since one can simply rely on true Monte Carlo label for the reconstructed particle cluster to assign with no ambiguities the correct track score: 0 for shower-like particles such as photons and 1 for track-like particles such as protons and muons. [Figure 4.12](#) shows the assigned BDT score with the nominal (thin line) and cheated (thick line) particle classification stage for protons (blue) and muons (red), where the latter cheated version was adopted.

### 4.3. Efficiency evaluation for different reconstruction stages: approach and results

Using this set of tools, whose performance have been thoroughly evaluated and whose limitations have been highlighted in the previous paragraphs, it is now possible to get a detailed understanding of the most critical reconstruction stages and understand the source of errors and how to address them, weighing their relevance on the impact these changes can have based on the reconstruction and downstream event selection performance.

Dealing with this task, we first focused on PandoraNeutrino reconstruction path. We can separate the operations of this stage into five substages: the 2D cluster creation, the 3D vertex creation, the 3D particle creation, the particle hierarchy creation, and the particle classification. As already stated previously, we will exclude the particle hierarchy identification from the present study.

Given the present division in subsequent reconstruction steps, we can validate their performance by comparing the cheated and uncheated versions. The idea is to compare five reconstruction chains that process the same events. Each one differs from the previous in that a stage previously cheated to reach maximal efficiency is now replaced by its standard (i.e., uncheated) version. Starting from a fully cheated configuration, where the 2D cluster creation, the 3D vertex creation, the 3D particle creation, and the particle classification are cheated, we then replace the last step with its nominal/standard uncheated version, leaving only the three steps happening before as cheated. Continuing on with the same idea for all the stages, with the exception of the particle hierarchy creation algorithm, the last explored configuration has all the stages in their nominal format. Schematically, representing with a gray square each substage of the reconstruction (■), and filling it red when it is cheated (■), the configurations reported in [Table 4.1](#) are shown below (here the columns are the individual substages of the reconstruction chain)



Under the assumption that Pandora reconstruction algorithms are decoupled from

one another (see [section 3.3](#) and references therein), it is possible to state that the overall event reconstruction and selection efficiency is given by the product of the efficiency of the signal processing stage (see [subsection 3.2.3](#)) and the efficiencies of the individual steps of the event reconstruction and the event selection efficiency, i.e.,

$$\begin{aligned} \epsilon = & \epsilon_{\text{signal processing}} \times \epsilon_{\text{2D clustering}} \times \epsilon_{\text{vertex creation}} \times \\ & \times \epsilon_{\text{3D reconstruction}} \times \epsilon_{\text{particle classification}} \times \epsilon_{\text{event selection}} \end{aligned} \quad (4.6)$$

Making the logical assumption that cheating a step of the reconstruction makes its efficiency effectively 100 %, and indicating with an asterisk the efficiency of a cheated reconstruction stage, it is possible to compare two of the aforementioned configurations that differ only in how a single step operates. For example, the ratio between the efficiencies of the “fully cheated” configuration (A) and that with all stages cheated except for the last (configuration B) is

$$\frac{\epsilon^B}{\epsilon^A} = \frac{\epsilon_{\text{sig.}} \times \epsilon_{\text{2D}}^* \times \epsilon_{\text{vertex}}^* \times \epsilon_{\text{3D}}^* \times \epsilon_{\text{class.}} \times \epsilon_{\text{ev. sel.}}^B}{\epsilon_{\text{sig.}} \times \epsilon_{\text{2D}}^* \times \epsilon_{\text{vertex}}^* \times \epsilon_{\text{3D}}^* \times \epsilon_{\text{class.}}^* \times \epsilon_{\text{ev. sel.}}^A} = \frac{\epsilon_{\text{class.}}}{\epsilon_{\text{class.}}^*} \times \left( \frac{\epsilon_{\text{ev. sel.}}^B}{\epsilon_{\text{ev. sel.}}^A} \right) \quad (4.7)$$

Here the apex refers to which of the configurations is used, and the asterisk is used to distinguish the cheated from the nominal version of a given reconstruction stage. All the configurations are listed in [Table 4.1](#), and the same notation is adopted for all the equations/for all the counts from now on. Additionally, the notation of the single stages is simplified for the sake of brevity.

It is possible to redraft/rewrite Eq. (4.7) as follows,

$$\epsilon_{\text{class.}} \times \left( \frac{\epsilon_{\text{ev. sel.}}^B}{\epsilon_{\text{ev. sel.}}^A} \right) = \frac{\epsilon^B}{\epsilon^A} \times \epsilon_{\text{class.}}^* \quad (4.8)$$

It is worth noting that, under the reasoned assumption that  $\epsilon^* = 100\%$  for any cheated stage, we can drop this term in Eq. (4.8) to obtain

$$\epsilon_{\text{class.}} \times \left( \frac{\epsilon_{\text{ev. sel.}}^B}{\epsilon_{\text{ev. sel.}}^A} \right) = \frac{\epsilon^B}{\epsilon^A} \quad (4.9)$$

It is worth remarking that this result is exactly the same as comparing the number of selected signal candidates in the two configurations,  $\epsilon^B / \epsilon^A \equiv N_{\text{signal}}^B / N_{\text{signal}}^A$ .

### 4.3.1. Results

Once an analysis method is established, we can start our evaluation by computing the reconstruction and selection efficiency for all the configurations shown in [Table 4.1](#). The

**Table 4.1.** List of all the configurations considered for the evaluation of the individual and global reconstruction performance in section 4.3. The red cross mark  $\times$  indicates the steps of the reconstruction that are kept nominal, whereas the green tick mark  $\checkmark$  indicates the ones that are cheated.

Id.	Configuration name	2D clusters	Vertex	3D particles	Particles
		creation	creation	reconstruction	classification
A	Fully cheated	$\checkmark$	$\checkmark$	$\checkmark$	$\checkmark$
B	Cheated up to the particle classification algorithm	$\checkmark$	$\checkmark$	$\checkmark$	$\times$
C	Cheated up to the particle three-dimensional reconstruction algorithm	$\checkmark$	$\checkmark$	$\times$	$\times$
D	Cheated up to the vertex reconstruction	$\checkmark$	$\times$	$\times$	$\times$
E	Nominal	$\times$	$\times$	$\times$	$\times$

first step was to compute the integral efficiency by extracting the ratio between the number of true and selected  $\nu_\mu$ CCQE Np events and the number of true  $1\mu Np$  interactions. These efficiencies are compared in Figure 4.13. A first remark is that, as more steps of the reconstruction are cheated, the overall efficiency increases: this suggests that, at least, the addition of any cheated algorithm improves the event reconstruction, which was expected but not necessarily granted. Further observations follow from the visual inspection of the efficiencies achieved under different reconstruction configurations. For example, it is clear that once the 2D clusters are created correctly, i.e., cheated, the reconstruction performs better overall by comparing the nominal reconstruction (configuration E) with the “cheated up to the vertex reconstruction” reconstruction (configuration D) bin,  $(54.7 \pm 0.5)$  % and  $(63.1 \pm 0.5)$  % respectively. From this it is evident that the impact of the cluster creation algorithms on the overall outcome of the chain is high. The same holds for the difference between the “cheated up to the vertex reconstruction” (configuration D) and the “cheated up to the particle three-dimensional reconstruction” (configuration C) bins,  $(63.1 \pm 0.5)$  % and  $(68.1 \pm 0.5)$  % respectively: the vertex creation algorithm has a large impact on the outcome of the chain. The uncertainties on the efficiencies presented here are computed considering a binomial statistic for the ratio of the number of selected signal events over the total number of signal events. The treatment for the statistical uncertainties is the same for all further computations.

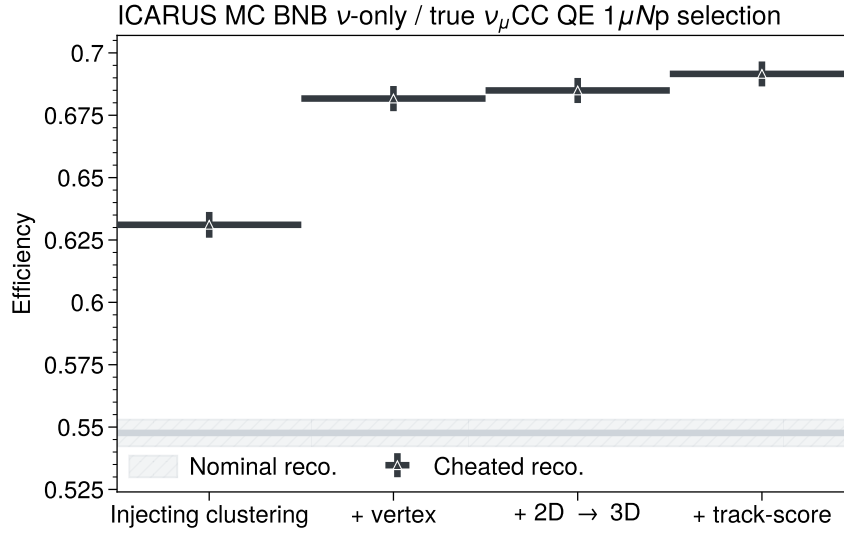


**Figure 4.13.** Evaluation of the event reconstruction and selection efficiencies for the configuration presented in Table 4.1. Each bin is labelled according to the stage whose cheated version is added to the full reconstruction chain; in the first only the clustering creation is cheated (configuration D), and each bin adds a cheated step up to the fully cheated configuration (A) shown in last bin.

We can now exploit these results to compute a value which is proportional to the efficiency of each reconstruction step by factorising the event selection efficiency for each of the two configurations considered in the computation, as highlighted in Eq. (4.9). Extracting this result for all possible combination of subsequent configurations, we can extract values proportional to the single-stage efficiencies,

$$\epsilon_{\text{2D clusters}} \times \left( \frac{\epsilon_{\text{ev. sel.}}^E}{\epsilon_{\text{ev. sel.}}^D} \right) = \frac{\epsilon^E}{\epsilon^D} = \frac{(54.7 \pm 0.5)\%}{(63.1 \pm 0.5)\%} = (86.8 \pm 1.1)\% \quad (4.10)$$

$$\epsilon_{\text{vertex creation}} \times \left( \frac{\epsilon_{\text{ev. sel.}}^D}{\epsilon_{\text{ev. sel.}}^C} \right) = \frac{\epsilon^D}{\epsilon^C} = \frac{(63.1 \pm 0.5)\%}{(68.1 \pm 0.5)\%} = (92.6 \pm 1.0)\% \quad (4.11)$$

$$\epsilon_{\text{3d reconstruction}} \times \left( \frac{\epsilon_{\text{ev. sel.}}^C}{\epsilon_{\text{ev. sel.}}^B} \right) = \frac{\epsilon^C}{\epsilon^B} = \frac{(68.1 \pm 0.5)\%}{(68.4 \pm 0.5)\%} = (99.5 \pm 1.0)\% \quad (4.12)$$

$$\epsilon_{\text{particle classification}} \times \left( \frac{\epsilon_{\text{ev. sel.}}^B}{\epsilon_{\text{ev. sel.}}^A} \right) = \frac{\epsilon^B}{\epsilon^A} = \frac{(68.4 \pm 0.5)\%}{(69.1 \pm 0.5)\%} = (99.0 \pm 1.0)\% \quad (4.13)$$

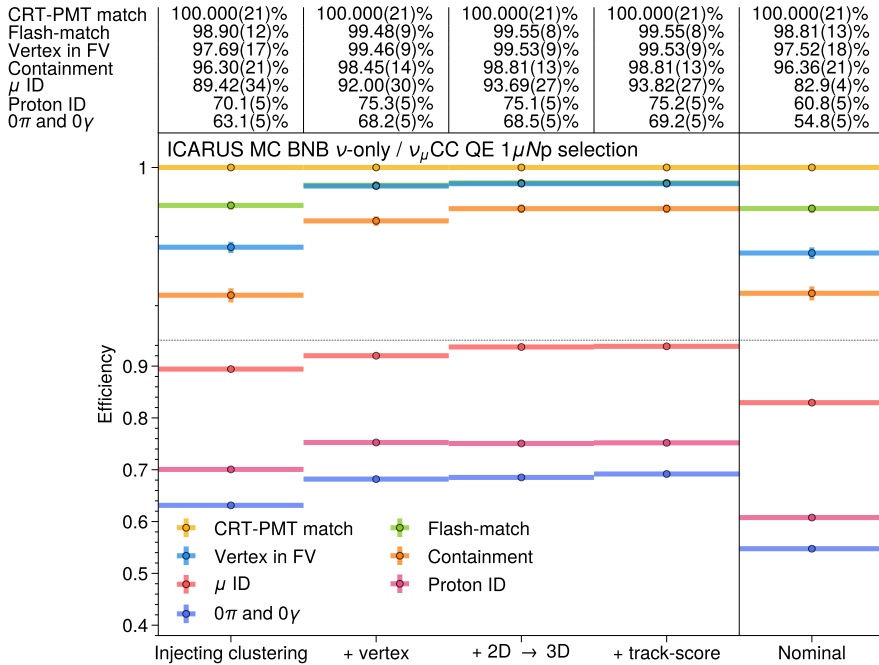


**Figure 4.14.** Cut-by-cut event reconstruction and selection efficiency for all configurations listed in Table 4.1. Selection cuts are subsequently added to the ones listed above. The top table shows the efficiency of each configuration for each selection cut. It is worth remarking that the scale on the  $y$  axis is not uniform in that the region from 0.9 to 1 is scaled up to allow for better visual separation of the cuts.

Since the signal definition is the same for all configurations, we could (qualitatively) assume that no major difference should be present in the efficiency of the event selection: in such a hypothesis, the ratio between the selection efficiencies in Eqs. (4.10)–(4.13) should be approximately one. However, a more quantitative estimation of these efficiencies is needed to provide a stronger result.

With this target in mind, it is interesting to evaluate the interplay between cheating cumulatively to a substage of the reconstruction chain and each of the selection cut applied (described in detail in section 4.1). To do so, the event reconstruction and selection efficiency are computed each time changing the reconstructed signal definition by cumulatively adding selection cuts. Figure 4.14 shows the result of this cut-by-cut efficiency for all five configurations in Table 4.1.

### 4.3.2. Extracting the selection efficiency

Referring to [Figure 4.14](#) it is evident that the first selection cut, i.e. CRT-PMT matching, has no impact on the events. For the present study, this is due to the type of events analysed, that include only neutrino candidate interactions, i.e. neither in-time nor out-of-time cosmics are simulated. The second cut, Flash-match, has a very small effect: this has the same explanation as CRT-PMT cut, since no cosmic-ray interaction is generated for the presently used sample. The first cut that introduces a reduction in the selected statistics is the requirement on the vertex position to lie inside the fiducial volume of the detector. This is a request that is strongly dependent on the reconstruction performance; therefore, it is expected that an improved vertex reconstruction results in an overall improvement on the efficiency. The following request that all particles are contained in the active volume of the detector is also strongly dependent on the reconstruction performance. Correct clustering of the hits and start-/end-point assignation is correlated with containment (if the true particles are contained, so should be the reconstructed ones). The last selection cuts concern the muon and proton identifications and the no-charged-pion and no-electromagnetic-shower requests. These have a large impact on the event selection efficiency, with a  $\sim 15\%$  loss in the identification of the proton, followed by the  $\sim 5\%$  loss due to the identification and rejection of charged pions and electromagnetic showers. The particle identification cuts, described in detail in [section 4.1](#), follows from cuts on variables that are direct consequence of the efficiency of Pandora reconstruction, such as the length requirements, the track and shower classification BDT score, the distance from the interaction vertex, and the particle hierarchy requirements, as well as variables that are heavily influenced by the calorimetric reconstruction performances, downstream of Pandora event reconstruction (see [section 3.4](#)). Assuming the correlation between variables that depend on Pandora topological reconstruction quality and variables that depends on the calorimetric reconstruction effectiveness is small, it is possible to factorise their contribution to the final selection efficiency, assigning a “reconstruction-related” event selection efficiency to the former and a “PID-related” event selection efficiency to the latter,

$$\epsilon_{\text{event selection}} = \epsilon_{\text{ev. sel., reco.}} \times \epsilon_{\text{ev. sel., pid.}} \quad (4.14)$$

Considering Eq. (4.6), we can rewrite it, as

$$\begin{aligned} \epsilon = & \epsilon_{\text{signal processing}} \times \epsilon_{\text{2D clusters}} \times \epsilon_{\text{vertex creation}} \times \epsilon_{\text{3D reconstruction}} \times \\ & \times \epsilon_{\text{particle classification}} \times \epsilon_{\text{event selection, reco.}} \times \epsilon_{\text{event selection, pid.}} \end{aligned} \quad (4.15)$$

We can make an additional assumption. Since the term  $\epsilon_{\text{event selection, reco.}}$  is related to the reconstruction efficiency, it is reasonable to assume that each stage in the reconstruction chain will give its specific contribution to the overall value. This hypothesis is supported, for example, by the observation that once the vertex reconstruction is cheated, the requirement that the vertex lie inside the TPC fiducial volume is automatically satisfied, as can be seen in Figure 4.14. In other words, the component of the selection efficiency associated with vertex containment is correlated with the success of correctly assigning the true interaction vertex. Taking this into account, we can rewrite Eq. (4.15) as

$$\begin{aligned} \epsilon = \epsilon_{\text{signal processing}} &\times \epsilon'_{\text{2D clusters}} \times \epsilon'_{\text{vertex creation}} \times \epsilon'_{\text{3D reconstruction}} \times \\ &\times \epsilon'_{\text{particle classification}} \times \epsilon_{\text{ev. sel., pid}} = \epsilon_{\text{sig. proc.}} \times \epsilon'_{\text{reco.}} \times \epsilon_{\text{ev. sel., pid}}, \end{aligned} \quad (4.16)$$

where the prime symbol ' is added to highlight that the efficiencies listed here slightly differ from the ones above in Eq. (4.15). Following the same strategy outlined in Eq. (4.6)–(4.9), we now obtain a new version of

$$\epsilon_{\text{particle class.}} \times \left( \frac{\epsilon_{\text{ev. sel.,pid}}^B}{\epsilon_{\text{ev. sel.,pid}}^A} \right) = \frac{\epsilon^B}{\epsilon^A}. \quad (4.17)$$

where we dropped the prime symbol for simplicity. We can now invert the equation to extract the term we want to evaluate:

$$\epsilon_{\text{particle class.}} = \frac{\epsilon^B}{\epsilon^A} \times \frac{\epsilon_{\text{ev. sel.,pid}}^A}{\epsilon_{\text{ev. sel.,pid}}^B}, \quad (4.18)$$

It is clear that to do this we need a final ingredient, which is given by the impact of PID onto selection efficiency, i.e.,  $\epsilon_{\text{ev. sel., pid}}$ . To extract such a parameter, we developed a modified event selection that allowed the effects of particle identification to be decoupled from the effects of the event reconstruction. In this modified event selection, all the cuts performed on variables that depend on the reconstruction performance are left unaltered, whereas the cuts that are dependent on the calorimetric particle identification are effectively bypassed considering the true particle labels. The requirements for this “modified” particle identification are detailed below.

To identify if a single muon is present in the interaction, the following cuts are applied:

- the particle should be tagged as a primary particle by Pandora,
- the conversion gap should be smaller than 10 cm,

- the track/shower classification score should be greater than 0.5,
- the track length should be greater than 50 cm,
- the label assigned via match with Monte Carlo information should correspond to a muon.

For the protons in the interaction, the following cuts are applied:

- the particle should be tagged as a primary particle by Pandora,
- the conversion gap should be smaller than 10 cm,
- the track/shower classification score should be greater than 0.4,
- the reconstructed deposited energy and the true kinetic energy should be greater than 50 MeV,
- the label assigned via match with Monte Carlo information should correspond to a proton.

For pions, the selection is the same as for protons, with the sole difference of requiring the true label of a charged pion and a lower energy threshold of 25 MeV.

For electromagnetic showers, the following cuts are applied:

- the particle should be tagged as a primary particle by Pandora,
- the track/shower classification score should be smaller than 0.5,
- the reconstructed deposited energy and the true kinetic energy should be greater than 25 MeV,
- the label assigned via match with Monte Carlo information should correspond to an electron or a photon.

Using this modified event selection, we extract again the efficiencies as a function of cheated stages and selection cuts (see [Figure 4.13](#)). [Figure 4.15](#) shows the efficiency for the same configurations (see [Table 4.1](#)) with the modified event selection.

For this modified event selection we can assume that the overall efficiency that accounts both for reconstruction, PID and selection is

$$\epsilon^{\text{mod. selection}} = \epsilon_{\text{sig. proc.}} \times \epsilon_{\text{reco.}} \times \epsilon_{\text{ev. sel., pid}}^{\text{mod. selection}}. \quad (4.19)$$

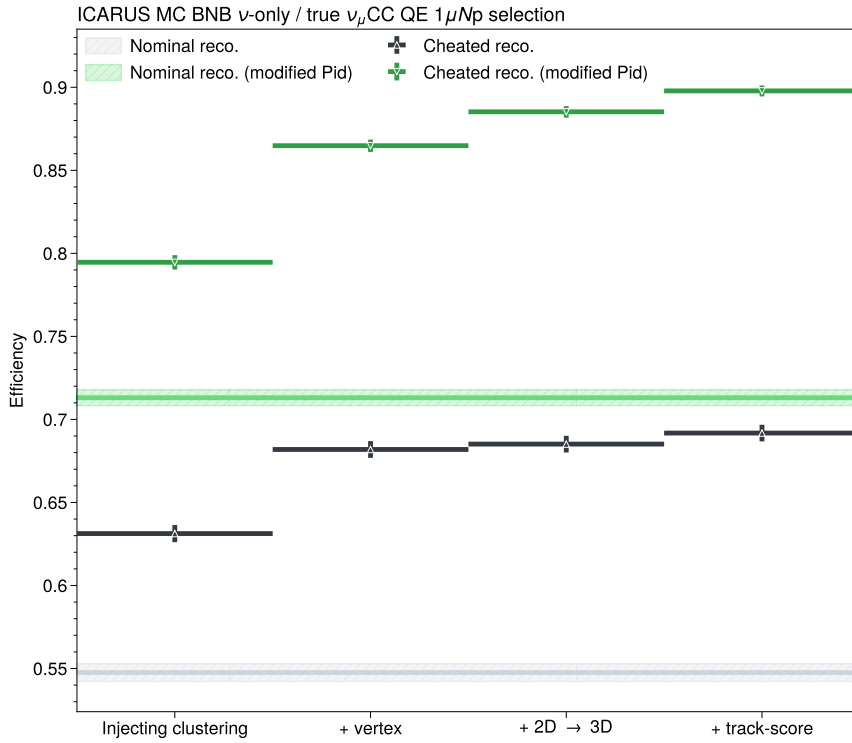


**Figure 4.15.** Evaluation of the event reconstruction and selection efficiency for all the configurations listed in Table 4.1. Both the event selection with the nominal particle identification (black markers) and the event selection with the modified particle identification (green markers) are shown.

This modified event selection does not rely on the performance of the PID, using the true underlying MC label to uniquely identify reconstructed particle species. Therefore we assumed that  $\epsilon_{\text{ev. sel., pid}}^{\text{mod. selection}} \simeq 1$ , since no particle misidentification inefficiencies related to PID are possible. We exploit this simplification, and comparing Eq. (4.19) and (4.16), we can extract the efficiency of the particle identification stage for each configuration of Table 4.1. The ratio of these two equations leads to

$$\frac{\epsilon^{\text{mod. selection}, c}}{\epsilon^c} = \frac{\epsilon_{\text{sig. proc.}} \times \epsilon_{\text{reco.}} \times \epsilon_{\text{ev. sel., pid}}^{\text{mod. selection}, c}}{\epsilon_{\text{sig. proc.}} \times \epsilon_{\text{reco.}} \times \epsilon_{\text{ev. sel., pid}}^c} = \frac{1}{\epsilon_{\text{ev. sel., pid}}^c} \quad (4.20)$$

for each configuration  $c$ . By inverting Eq. (4.20) we can estimate the contribution of

**Table 4.2.** For each configuration the corresponding efficiency is shown, using both the nominal event selection and the modified event selection described in subsection 4.3.2. The third column is the resulting efficiency of the particle identification step. Further details on the evaluation of the listed parameters are provided in the text.

Id.	Configuration name	$\epsilon$ (see Eq. 4.14)	$\epsilon^{\text{mod. selection}}$ (see Eq. 4.19)	$\epsilon_{\text{ev. sel., pid}}$ (see Eq. 4.21)
A	Fully cheated	$(69.2 \pm 0.5) \%$	$(89.78 \pm 0.33) \%$	$(77.1 \pm 0.6) \%$
B	Cheated up to the particle classification algorithm	$(68.5 \pm 0.5) \%$	$(88.52 \pm 0.35) \%$	$(77.4 \pm 0.6) \%$
C	Cheated up to the particle three-dimensional reconstruction algorithm	$(68.2 \pm 0.5) \%$	$(86.5 \pm 0.4) \%$	$(78.8 \pm 0.7) \%$
D	Cheated up to the vertex reconstruction	$(63.1 \pm 0.5) \%$	$(79.5 \pm 0.4) \%$	$(79.4 \pm 0.8) \%$
E	Nominal	$(54.8 \pm 0.5) \%$	$(71.3 \pm 0.5) \%$	$(76.8 \pm 0.9) \%$

particle identification, and thus calorimetric reconstruction, to the overall selection efficiency.

$$\epsilon_{\text{ev. sel., pid}}^c = \frac{\epsilon^c}{\epsilon^{\text{mod. selection}, c}}. \quad (4.21)$$

The particle identification efficiencies extracted are reported in Table 4.2.

By replacing the PID efficiency values extracted thanks to the modified selection in Eq. (4.18), we can derive an estimate for the efficiency of each stage of the reconstruction. This leads to the following results

$$\begin{aligned} \epsilon_{\text{reco.}} &= \epsilon_{\text{2D clusters}} \times \epsilon_{\text{vertex creation}} \times \epsilon_{\text{3D reco.}} \times \epsilon_{\text{particle class.}} = \\ &= (89.7 \pm 1.8) \% \times (91.9 \pm 1.6) \% \times (97.7 \pm 1.6) \% \times (98.6 \pm 1.5) \% \end{aligned} \quad (4.22)$$

These findings should be interpreted with caution. Firstly, they are obtained targeting a specific event topology. Therefore, it is reasonable to assume that a different event topology would yield significantly different results. As explicitly stated throughout the text, numerous assumptions and approximations have been made to obtain these results. All correlations between the various algorithms involved in Pandora reconstruction chain are assumed to be minimal. Additionally, to obtain the selection efficiencies,

most of the variables involved in the event selection cuts are assumed to be uncorrelated. These assumptions hold true to a certain extent.

However, as discussed in the subsequent section, an independent test on the vertex reconstruction was conducted. The results from this independent test, which are in good agreement with the results in Eq. (4.22), suggest that the starting point hypothesis is reasonable.

## 4.4. Impact of the vertex reconstruction

From the results shown in subsection 4.3.1 and subsection 4.3.2 it is possible to deduce that assigning correctly the interaction vertex plays a central role in the event reconstruction. This is obviously true for electromagnetic showers, where the distance from the vertex, often referred to as the “conversion gap”, is key to separating electron-induced electromagnetic showers from photon-induced ones. Since the radiation length  $X_0$  in LAr is approximately 14 cm, having an accurate measurement of the vertex location, with a  $\mathcal{O}(\text{mm})$  precision, is core for physics analyses, especially the ones relying on  $\nu_e$  interactions. Furthermore, there are instances where enhancing the vertex results in an overall improvement of the reconstruction (see subsection 4.2.2 and Refs. [146, 147]).

Qualitative tests were conducted on a Pandora reconstruction configuration where only certain aspects of the vertex reconstruction were cheated. The results demonstrated that this step did not suffer from the other components remaining uncheated and also resulted in a significant overall improvement in the event reconstruction performance, specifically in terms of selection efficiency enhancements for the selected events. Figure 4.16 shows the impact of cheating the vertex reconstruction, in terms of efficiency, considering each cut of the event selection alone. Several elements shown in Figure 4.16 are noteworthy. The bins shown here correspond to the three cheating configurations tested for the present study and also shown in Table 4.3. As mentioned in Table 4.3, the “Inj. vertex selection” configuration results from replacing the vertex selection step alone, as opposed to the full vertex identification step, i.e., replacing with the truth information the outcome of the BDT algorithm that selects the best interaction vertex from the list of the candidate vertices.

Looking at the result, a similar pattern to that of the previous section, specifically in Figure 4.13 and 4.14, emerges. This pattern suggests that enhancing the vertex reconstruction process positively impacts the overall event reconstruction performance. The efficiencies presented in Figure 4.16, particularly the efficiency achieved with all selec-

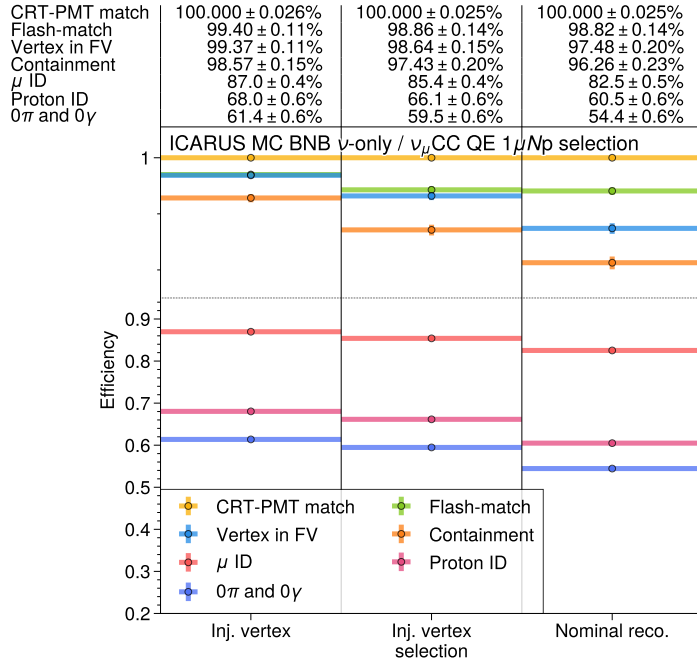


**Figure 4.16.** Cut-by-cut event reconstruction and selection efficiency for all the reconstruction configurations listed in Table 4.3. Each row in the table corresponds to the addition of a new cut on top of the previous ones. The top table shows the efficiency of each configuration for each selection cut. It is worth remarking that the scale on the  $y$  axis is not uniform in that the region from 0.9 to 1 is scaled up to allow for better visual separation of the cuts.

tion criteria simultaneously applied, serve as an upper bound on the potential improvement that can be realised if the vertex reconstruction were perfect. The two cheated configurations listed in Table 4.3 can provide further insight into the impact of different reconstruction stages.

Starting from configuration B, we studied the configuration where only the vertex selection step is cheated, meaning that the creation of the vertex candidates is still performed by the nominal reconstruction, but only the vertex closest in 3D space to the true one gets selected. We interpret this outcome as the maximum improvement we could achieve by a retraining of the BDT algorithm responsible for selecting the best vertex candidate. Notably, the efficiency enhancement from the nominal value ( $\epsilon = (54.4 \pm 0.6) \%$ )

**Table 4.3.** List of all the configurations used for the evaluation of the reconstruction performance in [section 4.4](#). The red cross mark  $\times$  indicates the steps of the reconstruction for which the nominal version is used, whereas the green tick mark  $\checkmark$  indicates those that are cheated. The orange asterisk  $*$  indicates that the cheating is done partially, such as in the case of the CheetedVertexSelection algorithm.

Id.	Configuration name	2D clusters	Vertex	3D particles	Particles
		creation	creation	reconstruction	classification
A	Cheated vertex creation algorithm (Inj. vertex)	$\times$	$\checkmark$	$\times$	$\times$
B	Cheated vertex selection algorithm (Inj. vertex selection)	$\times$	$*$	$\times$	$\times$
C	Nominal	$\times$	$\times$	$\times$	$\times$

to the outcome of this configuration, which is  $\epsilon_{\text{inj. vertex selection}} = (59.6 \pm 0.6)\%$ , is  $(5.1 \pm 0.8)\%$ . We might be tempted to conclude that retraining the BDT algorithm responsible for selecting the interaction vertex is the next step to improve the efficiency of Pandora event reconstruction. However, we should first explore all the results obtained with the other configuration.

Consequently, we conduct our analysis on configuration A of [Table 4.3](#), where all the algorithms involved with the reconstruction and identification of the interaction vertex are replaced by the CheatingVertexCreation algorithm, and the rest of the reconstruction chain is left unaltered (see [Table 4.3](#)). From this configuration, we intend to derive an upper bound on the reconstruction capabilities, assuming that the vertex reconstruction is optimal. Additionally, we aim to accomplish this independently of the results obtained in [subsection 4.3.1](#). We can exploit this result to strengthen the outcome of the work in [section 4.3](#).

In the analysis performed in [section 4.3](#), we were able to factorise the efficiency related to the PID by employing a modified event selection. To maintain the independence of this analysis, an alternative method to constrain the PID selection cut efficiency is required. We examined the distribution of the PID variables, specifically the  $\chi^2$ -based score defined in Eq. (3.8). These distributions are presented in [Figure 4.17](#), alongside the ratio of the spectra of the cheated configuration over the nominal configuration. Since no difference is highlighted, in accordance with expectations, we can conclude that the

enhancement in efficiency is predominantly attributable to a correct vertex assignment.

Given that the vertex impact is entirely reflected in an efficiency improvement, and no effect of the event selection PID is present, we computed the efficiency value for both the nominal configuration and for the cheated vertex reconstruction and identification (configuration A); both results are in Figure 4.16. The difference between these two configurations,  $(7.0 \pm 0.1)\%$ , represents the maximum improvement achievable by perfecting the vertex reconstruction alone, for the topology considered in this study.

To further validate this result, a parallel study was performed using a different sample of events with a completely different topology: electron neutrino charge-current quasi-elastic candidates,  $\nu_e$ CC QE. The  $\nu_e$ CC QE analysis reported an improvement in efficiency of  $\sim 7.3\%$ , which is perfectly compatible (within less than  $1\sigma$ ) with that found by this work  $(7.0 \pm 0.1)\%$  [146, 147].

This independent study of the vertex reconstruction and identification algorithms performance yields two noteworthy outcomes. The first outcome arises from the analysis conducted with configuration B. This approach demonstrated that retraining the BDT algorithm, specifically selecting the correct interaction vertex among the vertex candidates, can lead to an improvement of up to a maximum of approximately 5%. The second and most significant conclusion of this independent analysis is a cross-check of the results obtained using the analysis described in subsection 4.3.1 and presented in Eq. (4.22). In that analysis, the vertex reconstruction and identification stage was found to have an efficiency of  $(91.9 \pm 1.6)\%$ , corresponding to an “inefficiency” of  $(8.1 \pm 1.6)\%$ . Similarly, this independent analysis revealed that the vertex creation algorithm was found to have an “inefficiency of  $(7.0 \pm 0.1)\%$ . These two values are in good agreement, compatible within  $1\sigma$ , proving two fundamental points. Firstly, that the results presented in Eq. (4.22) are reliable, and secondly, that the vertex creation algorithm is decoupled from the other algorithms in the reconstruction chain; however, improving this algorithm results in enhanced performance across the whole reconstruction chain.

#### 4.4.1. Future outlook: improving the vertex creation algorithm

Given that the vertex reconstruction plays a pivotal role in the event reconstruction chain, as previously demonstrated, and that there is a potential  $\sim 8\%$  efficiency gain that can be realised by enhancing this specific reconstruction step, this section endeavours to outline the subsequent steps necessary to achieve this objective. This will surely prove core for the  $\nu_\mu$ CC QE Np analysis channel, but also for many future analyses, such

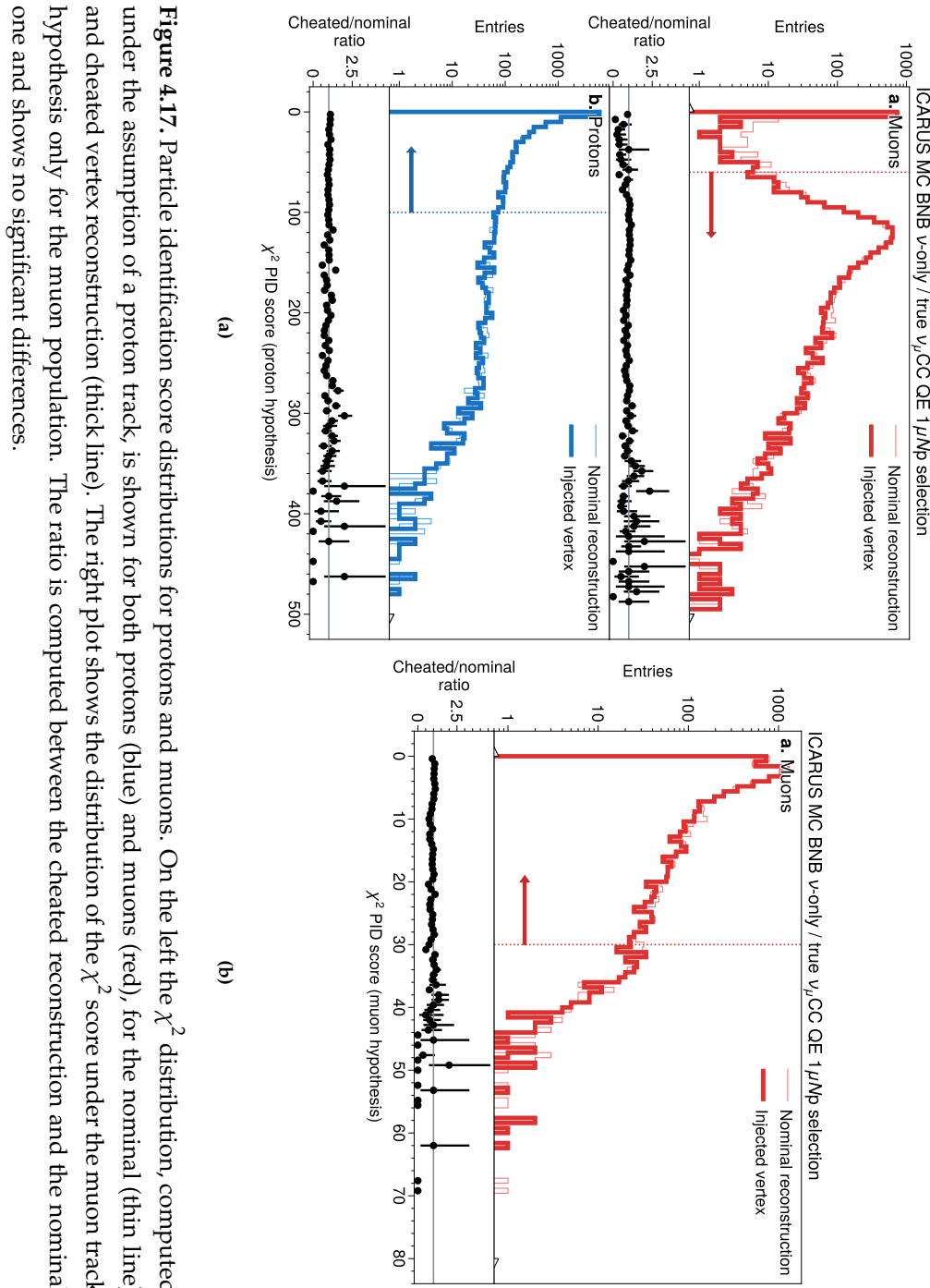


**Figure 4.17.** Particle identification score distributions for protons and muons. On the left the  $\chi^2$  distribution, computed under the assumption of a proton track, is shown for both protons (blue) and muons (red), for the nominal (thin line) and cheated vertex reconstruction (thick line). The right plot shows the distribution of the  $\chi^2$  score under the muon track hypothesis only for the muon population. The ratio is computed between the cheated reconstruction and the nominal one and shows no significant differences.

as a  $\nu_e$ CC QE analysis, for which preliminary work is now being performed [146].

To improve the vertex reconstruction, two strategies are possible. One might take the currently existing algorithms, which are described in section 3.3, and fine-tune their parameters and retrain the vertex selection algorithm: this is a valid solution, but this work highlights that the maximum improvement which can be achieved in this way would result in a  $\sim 5\%$  boost in the event reconstruction efficiency. Another possibility is represented by newer software algorithms, currently being developed within Pandora software framework and tested in other LArTPC experiments, such as DUNE. Such tools employ the use of newer and improved machine-learning-based technologies, such as Deep Neural Networks (DNNs) and Convolutional Neural Networks (CNNs).

The idea of the deep learning vertex creation algorithm [148] arises from two considerations. The first is that the filtered hits on the readout planes taken as input for Pandora topological event reconstruction can be assimilated to 2D images, where each hit is a point on the image itself. The second is that, upon a visual inspection of the images of the neutrino interaction by a human, the interaction vertex is often, though not always, easily identified. Such a premise suggests that it is reasonable to assume that a machine-learning-based algorithm, employing deep convolutional neural networks, often used in the context of medical imaging [149, 150], would be well suited to serve this inherently visual task.

The concept for this network design adopted in this context is to relate each hit to the distance from the interaction vertex: each hit contributes to the identification of the interaction vertex, and the network can learn reciprocal hit spatial correlations, providing context to the vertex identification. If the hit is defined as a pixel point of coordinates  $(h_x, h_c)$ , with  $x$  being the drift coordinate and  $c$  being the readout channel in  $u$ ,  $v$ , and  $w$  views, and the same is done for the true interaction vertex,  $(v_x, v_c)$ , it is possible to define as a distance metric

$$D = \frac{\sqrt{(v_x - h_x)^2 + (v_c - h_c)^2}}{\lfloor \sqrt{2(L-1)} \rfloor}. \quad (4.23)$$

It should be noted that this definition of distance is scale-invariant, since the denominator accounts for the characteristic dimension of the interaction  $L$ . This is core to prevent the network from learning any scale-related feature (i.e., not being correlated with the interaction characteristic dimension). The computed distance is then allocated into one of 19 classes: in this context, a “class” is a label that is added to each hit in the interaction; the network target is to learn this semantic label and, during inference, to assign the cor-

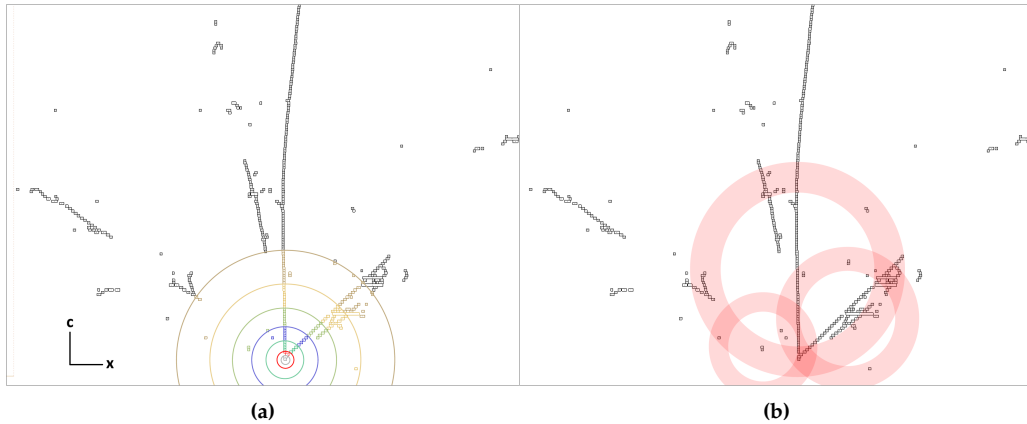


**Figure 4.18.** (a) shows the input hits and assignment of the first seven of the nineteen true distance classes for those hits. (b) shows a schematic of the heat map produced by three arbitrary hits during inference, for one view ( $w$ ) of an event.

rect class (for further details, see Figure 4.18(a)). The network then tries to infer the class for each hit. Once the classes are inferred for each hit in the interaction, the class number provides each hit the information of its relative distance to the reconstructed vertex. This information is used to project rings of appropriate inner and outer radii, centred on each hit. The width of the rings depends on the distance of the hit from the reconstructed vertex and is useful to provide a weight for each hit: the furthest hits are supposedly less spatially correlated with the interaction features closer to the vertex; therefore, the accuracy in their distance to the vertex is supposed to be less. In Figure 4.18(b) the projected rings for three hits in the interaction are shown as an example. The reconstructed interaction vertex lies in the common region where the rings cross.

Further details on the implementation of the deep learning (DL) vertex algorithm are presented in Ref. [148].

Preliminary tests and applications in DUNE show remarkable improvements in the vertex reconstruction; however, implementing it properly for the case of ICARUS requires caution. Firstly, it is important to remark that it was originally developed for use within DUNE, where the rate of cosmic-ray interaction is significantly lower. This means that a lower rate of cosmic contamination in neutrino interaction is present, helping the performance of the algorithm. This in turn implies that in order to both train the algorithm and then use it in inference with real data, some upgrades are required to the

reconstruction chain to ensure that slices are created correctly and no particle is split into multiple reconstructed slices, i.e., into different reconstructed interactions.

The analysis conducted in this work, as detailed in section 4.3, yielded the results presented in Eq. (4.22). These findings indicated that enhancing the vertex reconstruction process and addressing the approximately 8 % inefficiencies caused by its misidentification are essential. In this section, we outlined the subsequent steps involved, employing a novel approach for vertex reconstruction and outlining the other necessary steps to implement this revised algorithm.

However, the vertex reconstruction is not the only step that, given the results in Eq. (4.22), has a significant impact on the reconstruction performance. The cluster creation is also strongly influencing the performance of the event reconstruction. This is a more intricate step, which is addressed not only by the dedicated tools performing the cluster creation, but also by the tools involved in the three-dimensional reconstruction that perform the refinements of the clusters, as highlighted in the dedicated subsection in section 3.3. Therefore, plans to also perform improvements toward a more efficient cluster creation are foreseen, but given the complexity of the task, they require a more detailed study.



# Conclusions

I conclude that when I'm done with my  
thesis, life will be better

---

(Anonymous)

In the past twenty years several short-baseline anomalies hinted at the possibility of a fourth eV-scale “sterile” neutrino state, with incompatible results from appearance and disappearance results. The need to unravel the sterile neutrino picture led to the development of the SBN program. In the SBN program two functionally identical LArTPC-based experiments, the ICARUS and SBND experiments, are employed to measure with unprecedented  $>5\sigma$  sensitivity short baseline neutrino oscillations, with an accumulated predicted exposure of  $6.6 \times 10^{20}$  POT. ICARUS was the first large-scale LArTPC ever built and was the largest LArTPC, with an active LAr mass of 476 t, until the development of the ProtoDUNE detector. It is installed at Fermilab at a distance of 600 m from the on-axis BNB neutrino beam source, collecting neutrinos also from the NuMI neutrino beam  $\sim 6^\circ$  off-axis. It started data taking in 2022 and has now completed its fourth data-taking campaign. SBND operates closer to the BNB beam source, at a distance of 110 m, and joined ICARUS data taking as part of the SBN program, in 2024. SBND is relevant for the SBN program since it provides a flux monitor, measuring the unoscillated neutrino spectrum.

Data streams from both the ICARUS and SBND detectors are analysed to extract the physical information with a wide set of tools, performing multiple operations, from the raw signal processing to higher-level reconstruction of the interaction happening inside the LAr active volume.

This thesis focuses on a thorough study of the high-level reconstruction of the interaction, with a primary focus on the Pandora framework. A large set of tools is involved in performing the event reconstruction, and different approaches are taken to ensure a robust result is achieved. One key task of the event reconstruction and signal identifica-

tion pipeline is the identification of the interaction hierarchy from the processed signal deposited on the TPC wire-planes: all the final state particles in the interaction and their orientation in three-dimensional space are created building from their 2D projections on the readout planes, the interaction vertex is assigned, and the parent-daughter hierarchy is defined. In the context of the ICARUS experiment, two main frameworks are adopted: Pandora, which takes a more “task-oriented” approach to the event reconstruction task, providing hundreds of algorithms sequentially building up events, and SPINE, which provides an end-to-end optimisable machine-learning-based approach to the event reconstruction.

The highly modular approach of the Pandora event reconstruction framework allows algorithms within the reconstruction chain to be modified and replaced. This is exploited by a set of tools that enable the use of true Monte Carlo information to alter the reconstruction output of the different stages. This comprehensive set of tools has already been tested and used in the context of the SBND reconstruction, as well as for other Pandora-based reconstruction pipelines [138, 139]. These tools allow to investigate the impact of each step of Pandora reconstruction by altering the reconstructed objects using simulated events, where the true information derived from Monte Carlo is available. Using these altered reconstruction tools provides a strategy to validate the contribution of each algorithm to the entire reconstruction chain.

The first part of the work was devoted to thoroughly validating the impact of using these algorithms to the event reconstruction chain in different places, either as a standalone replacement of the nominal algorithm or cumulatively, replacing the “nominal” reconstruction algorithms up to a certain step of the sequence. Using a sample of events corresponding to an exposure of  $8 \times 10^{19}$  POT, or about  $6000 \nu_\mu$  CCQE Np interaction  $1\mu$ Np events inside the detector active volume, selected using the same event selection as the ongoing standalone ICARUS  $\nu_\mu$ -disappearance study, each algorithm was characterised in terms of its impact on downstream variables.

After a comprehensive validation of all these algorithms, testing their implementation in the context of the ICARUS event reconstruction, the results are consistent with expectations. We did find issues with the current implementation of the particle-hierarchy creation, which prevented us from using its cheated version in any of the subsequent studies.

Having validated these tools, we developed a method to exploit them to extract the efficiencies of each stage of Pandora reconstruction chain. We compared five reconstruction configurations: a sequence of four “cheated” configurations, arranged hierarchically

so that the first has all stages cheated, the second cheats all but the final stage, the third cheats only the first two stages, and the fourth cheats only the first stage; and finally, a baseline configuration using the standard, uncheated Pandora setup.

For all configurations, we evaluated the overall reconstruction and selection efficiency. To isolate the contribution of each reconstruction stage, we compared pairs of configurations: one in which all stages up to the step of interest were cheated, and the subsequent configuration in which that final stage was left uncheated.

To decouple the impact of the particle identification stage, which occurs downstream of event reconstruction, we designed a modified event selection. In this version, cuts related to particle identification were bypassed and true Monte Carlo labels were used instead. By comparing the events selected with the standard and modified procedures, we decoupled the particle identification efficiency for each of the five configurations from the efficiency of the stages.

The results of this analysis, showing the efficiency for all the major steps of the reconstruction chain, are presented below

$$\begin{aligned} \epsilon_{\text{reco.}} &= \epsilon_{\text{2D clusters}} \times \epsilon_{\text{vertex creation}} \times \epsilon_{\text{3D reco.}} \times \epsilon_{\text{particle class.}} = \\ &= (89.7 \pm 1.8) \% \times (91.9 \pm 1.6) \% \times (97.7 \pm 1.6) \% \times (98.6 \pm 1.5) %. \end{aligned}$$

The correct interpretation of our results requires some remarks. Firstly, we obtained them by targeting a specific event topology. Therefore, it is reasonable to assume that a different event topology would yield significantly different results. As explicitly stated throughout the text, we made numerous assumptions and approximations to obtain these results. We assumed that all correlations between the various algorithms involved in the Pandora reconstruction chain are minimal. Additionally, to extract the selection efficiencies, we assumed that most of the variables involved in the event selection cuts are uncorrelated. These assumptions hold true to a certain extent.

To test this result and the hypotheses that were made to obtain it, we performed an independent evaluation of the vertex performance. Using a different configuration, where only the vertex creation algorithm was cheated, we estimated the inefficiencies associated to an “incorrect reconstruction” of the interaction vertex. The outcome of this study, quoting the inefficiencies of the vertex reconstruction to  $(7.0 \pm 0.1) \%$ , allowed us to independently cross-check the main work presented in this thesis: the inefficiencies observed in the main body of this work accounted for  $(8.1 \pm 1.6) \%$ , compatible within  $1\sigma$  to these independent results.

This work shows that in order to significantly improve the performance of the event

reconstruction, some work has to be devoted to improving the vertex reconstruction. Additionally, it highlighted other areas of the event reconstruction where improvements are possible: the cluster creation and refinement, for example, that take place in both the first stage and the stage devoted to three-dimensional reconstruction, are not fully optimised for the ICARUS detector, and tuning the parameters involved in the reconstruction can lead to improving the performances of the event reconstruction.

In conclusion, this work had two main objectives. The first was to validate the implementation of the cheating tools within the ICARUS event reconstruction chain, showing their strong points and highlighting the steps that require more attention. The second was to demonstrate that this approach, which targets precise physics analysis, leads to meaningful results and provides a path to the next steps in improving the event reconstruction chain.

# A

## Acronyms

Throughout the thesis, multiple acronyms or concepts are presented and used; here are the most common with some context

<b>BNB</b>	Booster Neutrino Beam, the main beam feeding the SBN experiment
<b>BSM</b>	Beyond Standard Model
<b>CC/NC</b>	Charge/neutral current interactions
<b>CKM</b>	Cabibbo-Kobayashi-Maskawa matrix of quark mixing
<b>CNGS</b>	Cern Neutrinos to Gran Sasso beam
<b>Coh.</b>	Coherent neutrino scattering
<b>DaR/DiF</b>	Decay-at-Rest / -in-Flight
<b>DIS</b>	Deep inelastic scattering interaction
<b>DUNE</b>	Deep Underground Neutrino Experiment
<b>ES</b>	Elastic scattering interaction
<b>GALLEX</b>	Gallium neutrino observatory at LNGS
<b>GALLEX+GNO</b>	
<b>ICARUS</b> <i>or SBN-FD</i>	<i>Imaging Cosmic And Rare Underground Signals</i> , as it was called in the Gran Sasso era, now Far Detector in the SBN experiment
<b>LArTPC</b>	Liquid Argon Time Projection Chamber
<b>LSND</b>	Liquid Scintillator Neutrino Detector
<b>LEP</b>	Large Electron Positron collider
<b>LNGS</b>	Laboratori Nazionali del Gran Sasso
<b>Mini(Micro)BooNE</b>	Mini(micro) Booster Neutrino Experiment
<b>MSW</b>	Mikheyev-Smirnov-Wolfenstein oscillation of neutrinos in matter effect

A

A-2      *Appendix A. Acronyms*

<b>NO/NH and IO/IH</b>	Normal and inverted ordering/hierarchy of neutrino masses
<b>NOvA</b>	NuMI Off-axis $\nu_e$ Appearance
<b>NuMI</b>	Neutrinos at the Main Injector
<b>PMNS</b>	Pontecorvo-Maki-Nakagawa-Sakata matrix of neutrino oscillation
<b>PMT</b>	Photomultiplier tubes
<b>QE</b>	Quasielastic interactions
<b>Res.</b>	Resonant pion production interaction
<b>SAGE</b>	Soviet-American Gallium experiment
<b>SBN</b>	The Short Baseline Neutrino experiment, consisting of the three detectors on the BNB baseline
<b>SBND</b>	Short Baseline neutrino Near Detector
<b>SK</b>	Super Kamiokande
<b>SM</b>	the Standard Model of particle physics
<b>SNO</b>	Sudbury Neutrino Observatory
<b>SppS</b>	Super Proton (anti)Proton Synchrotron

A

# Bibliography

1. J. Chadwick, "The intensity distribution in the magnetic spectrum of  $\beta$  particles from radium (B + C)", *Verh. Phys. Gesell.* **16** (1914) 383–391. [Cited on p. 5](#)
2. W. Pauli, "Dear radioactive ladies and gentlemen", *Phys. Today* **31N9** (1978) 27. [Cited on p. 5](#)
3. E. Fermi, "Tentativo di una Teoria Dei Raggi  $\beta$ ", *Il Nuovo Cimento (1924-1942)* **11** (Jan, 1934) 1–19. [Cited on p. 5](#)
4. E. Fermi, "Versuch einer Theorie der  $\beta$ -Strahlen. I", *Zeitschrift für Physik* **88** (Mar, 1934) 161–177. [Cited on p. 5](#)
5. C. L. Cowan, F. Reines, F. B. Harrison, H. W. Kruse, and A. D. McGuire, "Detection of the free neutrino: A Confirmation", *Science* **124** (1956) 103–104. [Cited on p. 6](#)
6. C. D. Anderson and S. H. Neddermeyer, "Cloud chamber observations of cosmic rays at 4300 meters elevation and near sea-level", *Phys. Rev.* **50** (Aug, 1936) 263–271. [Cited on p. 6](#)
7. S. H. Neddermeyer and C. D. Anderson, "Note on the nature of cosmic-ray particles", *Phys. Rev.* **51** (May, 1937) 884–886. [\(Not cited.\)](#)
8. J. C. Street and E. C. Stevenson, "New Evidence for the Existence of a Particle of Mass Intermediate Between the Proton and Electron", *Phys. Rev.* **52** (Nov, 1937) 1003–1004. [Cited on p. 6](#)
9. B. Pontecorvo, *Electron and muon neutrinos*. Cambridge University Press., 1991. [Cited on p. 7](#)
10. G. Danby, J.-M. Gaillard, K. Goulianos, L. M. Lederman, N. Mistry, M. Schwartz, and J. Steinberger, "Observation of High-Energy Neutrino Reactions and the

- Existence of Two Kinds of Neutrinos”, *Phys. Rev. Lett.* **9** (Jul, 1962) 36–44. Cited on p. 7
11. ALEPH Collaboration, D. Decamp *et al.*, “A Precise Determination of the Number of Families With Light Neutrinos and of the Z Boson Partial Widths”, *Phys. Lett. B* **235** (1990) 399–411. Cited on pp. 7 and 24
  12. M. L. Perl, *et al.*, “Evidence for anomalous lepton production in  $e^+ - e^-$  annihilation”, *Phys. Rev. Lett.* **35** (Dec, 1975) 1489–1492. Cited on p. 7
  13. M. E. Peskin and D. V. Schroeder, *An Introduction to quantum field theory*. Addison-Wesley, Reading, USA, 1995. Cited on pp. 7 and 16
  14. M. Goldhaber, L. Grodzins, and A. W. Sunyar, “Helicity of neutrinos”, *Phys. Rev.* **109** (Feb, 1958) 1015–1017. Cited on p. 7
  15. UA1 Collaboration, G. Arnison *et al.*, “Experimental Observation of Lepton Pairs of Invariant Mass Around  $95 \text{ GeV}/c^2$  at the CERN SPS Collider”, *Phys. Lett. B* **126** (1983) 398–410. Cited on p. 8
  16. UA2 Collaboration, M. Banner *et al.*, “Observation of Single Isolated Electrons of High Transverse Momentum in Events with Missing Transverse Energy at the CERN anti-p p Collider”, *Phys. Lett. B* **122** (1983) 476–485. Cited on p. 8
  17. J. A. Formaggio and G. P. Zeller, “From eV to EeV: Neutrino cross sections across energy scales”, *Rev. Mod. Phys.* **84** (Sep, 2012) 1307–1341. Cited on pp. 9, 10, 11, and 12
  18. P. Musset and J.-P. Vialle, “Neutrino physics with gargamelle”, *Physics Reports* **39** (1978) 1–130. Cited on p. 12
  19. **Gargamelle Neutrino** Collaboration, F. J. Hasert *et al.*, “Observation of Neutrino Like Interactions without Muon or Electron in the Gargamelle Neutrino Experiment”, *Nucl. Phys. B* **73** (1974) 1–22. Cited on p. 12
  20. F. J. Hasert *et al.*, “Search for Elastic  $\nu_\mu$  Electron Scattering”, *Phys. Lett. B* **46** (1973) 121–124. Cited on p. 12
  21. M. Sajjad Athar, A. Fatima, and S. K. Singh, “Neutrinos and their interactions with matter”, *Prog. Part. Nucl. Phys.* **129** (2023) 104019, arXiv:2206.13792 [hep-ph]. Cited on p. 12

22. **Borexino** Collaboration, M. Agostini, *et al.*, “Experimental evidence of neutrinos produced in the CNO fusion cycle in the Sun”, *Nature* **587** (Nov, 2020) 577–582.  
*Cited on pp. 12 and 22*
23. C. Giunti, Y. F. Li, C. A. Ternes, and Z. Xin, “Reactor antineutrino anomaly in light of recent flux model refinements”, *Phys. Lett. B* **829** (2022) 137054,  
[arXiv:2110.06820 \[hep-ph\]](https://arxiv.org/abs/2110.06820). *Cited on p. 12*
24. K. Lande, L. M. Lederman, and W. Chinowsky, “Report on Long-Lived  $K^0$  Mesons”, *Phys. Rev.* **105** (Mar, 1957) 1925–1927. *Cited on p. 12*
25. B. Pontecorvo, “Mesonium and Antimesonium”, *Sov. Phys. JETP* **6** (1958) 429–431.  
*Cited on p. 13*
26. Z. Maki, M. Nakagawa, and S. Sakata, “Remarks on the unified model of elementary particles”, *Prog. Theor. Phys.* **28** (1962) 870–880. *Cited on p. 13*
27. B. T. Cleveland, T. Daily, R. Davis, Jr., J. R. Distel, K. Lande, C. K. Lee, P. S. Wildenhain, and J. Ullman, “Measurement of the solar electron neutrino flux with the Homestake chlorine detector”, *Astrophys. J.* **496** (1998) 505–526. *Cited on p. 13*
28. A. Serenelli, “Alive and well: A short review about standard solar models”, *The European Physical Journal A* **52** (Apr, 2016) 78. *Cited on p. 14*
29. J. N. Bahcall, W. F. Huebner, S. H. Lubow, P. D. Parker, and R. K. Ulrich, “Standard solar models and the uncertainties in predicted capture rates of solar neutrinos”, *Rev. Mod. Phys.* **54** (Jul, 1982) 767–799. *Cited on pp. 13 and 17*
30. J. N. Bahcall, A. M. Serenelli, and S. Basu, “New solar opacities, abundances, helioseismology, and neutrino fluxes”, *Astrophys. J. Lett.* **621** (2005) L85–L88,  
[arXiv:astro-ph/0412440](https://arxiv.org/abs/astro-ph/0412440). *Cited on pp. 13 and 17*
31. **SAGE** Collaboration, J. N. Abdurashitov, *et al.*, “Measurement of the solar neutrino capture rate with gallium metal”, *Phys. Rev. C* **60** (Oct, 1999) 055801.  
*Cited on p. 14*
32. W. Hampel, *et al.*, “GALLEX solar neutrino observations: results for GALLEX IV”, *Physics Letters B* **447** (1999) 127–133. *Cited on p. 14*
33. M. Altmann, *et al.*, “GNO solar neutrino observations: results for GNO I”, *Physics Letters B* **490** (2000) 16–26. *Cited on p. 14*

34. **Super-Kamiokande** Collaboration, K. Abe, *et al.*, “Solar neutrino measurements in Super-Kamiokande-IV”, *Phys. Rev. D* **94** (Sep, 2016) 052010. Cited on p. 15
35. **Kamiokande-II** Collaboration, K. S. Hirata *et al.*, “Experimental Study of the Atmospheric Neutrino Flux”, *Phys. Lett. B* **205** (1988) 416. Cited on pp. 15 and 22
36. D. Casper, *et al.*, “Measurement of atmospheric neutrino composition with the IMB-3 detector”, *Phys. Rev. Lett.* **66** (May, 1991) 2561–2564. Cited on p. 15
37. P. Lipari, “The Atmospheric neutrino problem”, in *8th Rencontres de Blois on Neutrinos, Dark Matter and the Universe*. 6, 1996. Cited on p. 15
38. **The Super-Kamiokande** Collaboration, Y. Ashie, *et al.*, “Evidence for an Oscillatory Signature in Atmospheric Neutrino Oscillations”, *Phys. Rev. Lett.* **93** (Sep, 2004) 101801. Cited on pp. 15 and 22
39. **OPERA** Collaboration, N. Agafonova, *et al.*, “Discovery of  $\tau$  Neutrino Appearance in the CNGS Neutrino Beam with the OPERA Experiment”, *Phys. Rev. Lett.* **115** (Sep, 2015) 121802. Cited on p. 15
40. **SNO** Collaboration, Q. R. Ahmad, *et al.*, “Measurement of the Rate of  $\nu_e + d \rightarrow p + p + e^-$  Interactions Produced by  $^8B$  Solar Neutrinos at the Sudbury Neutrino Observatory”, *Phys. Rev. Lett.* **87** (Jul, 2001) 071301. Cited on p. 16
41. **SNO** Collaboration, Q. R. Ahmad, *et al.*, “Direct Evidence for Neutrino Flavor Transformation from Neutral-Current Interactions in the Sudbury Neutrino Observatory”, *Phys. Rev. Lett.* **89** (Jun, 2002) 011301. (Not cited.)
42. **Super-Kamiokande** Collaboration, S. Fukuda, *et al.*, “Solar  $^8B$  and hep Neutrino Measurements from 1258 Days of Super-Kamiokande Data”, *Phys. Rev. Lett.* **86** (Jun, 2001) 5651–5655. Cited on p. 16
43. **SAGE** Collaboration, J. N. Abdurashitov, *et al.*, “Measurement of the solar neutrino capture rate with gallium metal. III. Results for the 2002–2007 data-taking period”, *Phys. Rev. C* **80** (Jul, 2009) 015807. Cited on pp. 16 and 22
44. **GNO** Collaboration, M. Altmann *et al.*, “Complete results for five years of GNO solar neutrino observations”, *Phys. Lett. B* **616** (2005) 174–190, [arXiv:hep-ex/0504037](https://arxiv.org/abs/hep-ex/0504037). Cited on pp. 16 and 22

45. SNO Collaboration, B. Aharmim, *et al.*, “Electron energy spectra, fluxes, and day-night asymmetries of  ${}^8\text{B}$  solar neutrinos from measurements with nacl dissolved in the heavy-water detector at the sudbury neutrino observatory”, *Phys. Rev. C* **72** (Nov, 2005) 055502. [Cited on p. 17](#)
46. K. Zuber, *Neutrino Physics*. Series in High Energy Physics, Cosmology & Gravitation. Taylor & Francis, Boca Raton, FL, third edition. ed., 2020. [Cited on p. 18](#)
47. G. C. Branco, L. Lavoura, and M. N. Rebelo, “Majorana Neutrinos and CP Violation in the Leptonic Sector”, *Phys. Lett. B* **180** (1986) 264–268. [Cited on p. 19](#)
48. Particle Data Group Collaboration, S. Navas, *et al.*, “Review of particle physics”, *Phys. Rev. D* **110** (Aug, 2024) 030001. [Cited on pp. 19, 24, and 82](#)
49. KamLAND Collaboration, K. Eguchi, *et al.*, “First Results from KamLAND: Evidence for Reactor Antineutrino Disappearance”, *Phys. Rev. Lett.* **90** (Jan, 2003) 021802. [Cited on pp. 19 and 24](#)
50. S. P. Mikheev and A. Y. Smirnov, “Resonant amplification of neutrino oscillations in matter and solar neutrino spectroscopy”, *Nuovo Cim. C* **9** (1986) 17–26. [Cited on p. 19](#)
51. S. P. Mikheyev and A. Y. Smirnov, “Resonance Amplification of Oscillations in Matter and Spectroscopy of Solar Neutrinos”, *Sov. J. Nucl. Phys.* **42** (1985) 913–917. [\(Not cited.\)](#)
52. L. Wolfenstein, “Neutrino oscillations in matter”, *Phys. Rev. D* **17** (May, 1978) 2369–2374. [Cited on p. 19](#)
53. K. J. Kelly and S. J. Parke, “Matter density profile shape effects at DUNE”, *Phys. Rev. D* **98** (Jul, 2018) 015025. [Cited on p. 20](#)
54. Borexino Collaboration, S. K. Agarwalla *et al.*, “Constraints on flavor-diagonal non-standard neutrino interactions from Borexino Phase-II”, *JHEP* **02** (2020) 038, [arXiv:1905.03512 \[hep-ph\]](#). [Cited on p. 20](#)
55. O. Mena and S. Parke, “Unified graphical summary of neutrino mixing parameters”, *Phys. Rev. D* **69** (Jun, 2004) 117301. [Cited on pp. 21 and 30](#)

56. **BOREXINO** Collaboration, M. Agostini *et al.*, “Sensitivity to neutrinos from the solar CNO cycle in Borexino”, *Eur. Phys. J. C* **80** (2020) 1091, [arXiv:2005.12829 \[hep-ex\]](#). Cited on p. 22
57. S. Kumaran, L. Ludhova, Ö. Penek, and G. Settanta, “Borexino Results on Neutrinos from the Sun and Earth”, *Universe* **7** (2021) 231, [arXiv:2105.13858 \[hep-ex\]](#). Cited on p. 22
58. **JUNO** Collaboration, A. Abusleme *et al.*, “JUNO sensitivity to  ${}^7\text{Be}$ , pep, and CNO solar neutrinos”, *JCAP* **10** (2023) 022, [arXiv:2303.03910 \[hep-ex\]](#). Cited on p. 22
59. **Super-Kamiokande** Collaboration, K. Abe *et al.*, “Solar neutrino measurements using the full data period of Super-Kamiokande-IV”, *Phys. Rev. D* **109** (2024) 092001, [arXiv:2312.12907 \[hep-ex\]](#). Cited on p. 22
60. **KamLAND** Collaboration, A. Gando, *et al.*, “ ${}^7\text{Be}$  solar neutrino measurement with KamLAND”, *Phys. Rev. C* **92** (Nov, 2015) 055808. Cited on p. 22
61. **MACRO** Collaboration, M. Ambrosio *et al.*, “Matter effects in upward going muons and sterile neutrino oscillations”, *Phys. Lett. B* **517** (2001) 59–66, [arXiv:hep-ex/0106049](#). Cited on p. 22
62. **T2K** Collaboration, K. Abe, *et al.*, “Observation of Electron Neutrino Appearance in a Muon Neutrino Beam”, *Phys. Rev. Lett.* **112** (Feb, 2014) 061802. Cited on p. 23
63. **T2K** Collaboration, K. Abe *et al.*, “Measurements of neutrino oscillation parameters from the T2K experiment using  $3.6 \times 10^{21}$  protons on target”, *Eur. Phys. J. C* **83** (2023) 782, [arXiv:2303.03222 \[hep-ex\]](#). Cited on p. 23
64. **NOvA** Collaboration, P. Adamson, *et al.*, “Constraints on Oscillation Parameters from  $\nu_e$  Appearance and  $\nu_\mu$  Disappearance in NOvA”, *Phys. Rev. Lett.* **118** (Jun, 2017) 231801. Cited on p. 23
65. **Double Chooz** Collaboration, Y. Abe, *et al.*, “Indication of Reactor  $\bar{\nu}_e$  Disappearance in the Double Chooz Experiment”, *Phys. Rev. Lett.* **108** (Mar, 2012) 131801. Cited on p. 24
66. F. P. An, *et al.*, “Observation of Electron-Antineutrino Disappearance at Daya Bay”, *Phys. Rev. Lett.* **108** (Apr, 2012) 171803. Cited on p. 24

67. RENO Collaboration, J. K. Ahn, *et al.*, “Observation of Reactor Electron Antineutrinos Disappearance in the RENO Experiment”, *Phys. Rev. Lett.* **108** (May, 2012) 191802. Cited on p. 24
68. C. A. Argüelles *et al.*, “New opportunities at the next-generation neutrino experiments I: BSM neutrino physics and dark matter”, *Rept. Prog. Phys.* **83** (2020) 124201, arXiv:1907.08311 [hep-ph]. Cited on p. 24
69. M. A. Acero *et al.*, “White paper on light sterile neutrino searches and related phenomenology”, *J. Phys. G* **51** (2024) 120501, arXiv:2203.07323 [hep-ex]. Cited on p. 24
70. LSND Collaboration, A. Aguilar, *et al.*, “Evidence for neutrino oscillations from the observation of  $\bar{\nu}_e$  appearance in a  $\bar{\nu}_\mu$  beam”, *Phys. Rev. D* **64** (Nov, 2001) 112007. Cited on pp. 25, 26, and 27
71. KARMEN Collaboration, B. Armbruster, *et al.*, “Upper limits for neutrino oscillations  $\bar{\nu}_\mu \rightarrow \bar{\nu}_e$  from muon decay at rest”, *Phys. Rev. D* **65** (Jun, 2002) 112001. Cited on pp. 26 and 31
72. B. Louis, V. Sandberg, H. White, and D. Kestenbaum, “A thousand eyes: The story of LSND”, *Los Alamos Science* (1997) 92–115. Cited on p. 27
73. MiniBooNE Collaboration, A. A. Aguilar-Arevalo *et al.*, “Updated MiniBooNE neutrino oscillation results with increased data and new background studies”, *Phys. Rev. D* **103** (2021) 052002, arXiv:2006.16883 [hep-ex]. Cited on p. 27
74. G. Mention, M. Fechner, T. Lasserre, T. A. Mueller, D. Lhuillier, M. Cribier, and A. Letourneau, “The Reactor Antineutrino Anomaly”, *Phys. Rev. D* **83** (2011) 073006, arXiv:1101.2755 [hep-ex]. Cited on p. 27
75. C. Giunti, Y. F. Li, C. A. Ternes, O. Tyagi, and Z. Xin, “Gallium Anomaly: critical view from the global picture of  $\nu_e$  and  $\bar{\nu}_e$  disappearance”, *JHEP* **10** (2022) 164, arXiv:2209.00916 [hep-ph]. Cited on pp. 29 and 33
76. S. R. Elliott, V. Gavrin, and W. Haxton, “The gallium anomaly”, *Prog. Part. Nucl. Phys.* **134** (2024) 104082, arXiv:2306.03299 [nucl-ex]. Cited on p. 29
77. NOMAD Collaboration, P. Astier *et al.*, “Search for  $\nu_\mu \rightarrow \nu_e$  oscillations in the NOMAD experiment”, *Phys. Lett. B* **570** (2003) 19–31, arXiv:hep-ex/0306037. Cited on p. 31

78. C. Rubbia, “The Liquid Argon Time Projection Chamber: A New Concept for Neutrino Detectors”, Tech. Rep. CERN-EP-INT-77-08, CERN-EP-77-08, CERN, 5, 1977. [Cited on pp. 31, 37, and 45](#)
79. **MicroBooNE** Collaboration, P. Abratenko, *et al.*, “Search for an excess of electron neutrino interactions in MicroBooNE using multiple final-state topologies”, *Phys. Rev. Lett.* **128** (Jun, 2022) 241801. [Cited on p. 32](#)
80. C. A. Argüelles, I. Esteban, M. Hostert, K. J. Kelly, J. Kopp, P. A. N. Machado, I. Martinez-Soler, and Y. F. Perez-Gonzalez, “MicroBooNE and the  $\nu_e$  Interpretation of the MiniBooNE Low-Energy Excess”, *Phys. Rev. Lett.* **128** (Jun, 2022) 241802. [Cited on p. 32](#)
81. **ICARUS** Collaboration, M. Antonello *et al.*, “Search for anomalies in the  $\nu_e$  appearance from a  $\nu_\mu$  beam”, *Eur. Phys. J. C* **73** (2013) 2599, [arXiv:1307.4699 \[hep-ex\]](#). [Cited on pp. 32 and 51](#)
82. M. Antonello *et al.*, “Some conclusive considerations on the comparison of the ICARUS  $\nu_\mu \rightarrow \nu_e$  oscillation search with the MiniBooNE low-energy event excess”, [arXiv:1502.04833 \[hep-ph\]](#). [Cited on p. 32](#)
83. **OPERA** Collaboration, N. Agafonova *et al.*, “New results on  $\nu_\mu \rightarrow \nu_\tau$  appearance with the OPERA experiment in the CNGS beam”, *JHEP* **11** (2013) 036, [arXiv:1308.2553 \[hep-ex\]](#). [Erratum: JHEP 04, 014 (2014)]. [Cited on pp. 32 and 51](#)
84. Y. Declais *et al.*, “Search for neutrino oscillations at 15-meters, 40-meters, and 95-meters from a nuclear power reactor at Bugey”, *Nucl. Phys. B* **434** (1995) 503–534. [Cited on p. 32](#)
85. **NEOS** Collaboration, Y. J. Ko, *et al.*, “Sterile neutrino search at the NEOS experiment”, *Phys. Rev. Lett.* **118** (Mar, 2017) 121802. [Cited on p. 32](#)
86. **PROSPECT** Collaboration, M. Andriamirado *et al.*, “Improved short-baseline neutrino oscillation search and energy spectrum measurement with the PROSPECT experiment at HFIR”, *Phys. Rev. D* **103** (2021) 032001, [arXiv:2006.11210 \[hep-ex\]](#). [Cited on p. 32](#)

87. **STEREO** Collaboration, H. Almazán *et al.*, “STEREO neutrino spectrum of  $^{235}\text{U}$  fission rejects sterile neutrino hypothesis”, *Nature* **613** (2023) 257–261, [arXiv:2210.07664 \[hep-ex\]](https://arxiv.org/abs/2210.07664). Cited on p. 32
88. **RENO and NEOS** Collaboration, Z. Atif, *et al.*, “Search for sterile neutrino oscillations using RENO and NEOS data”, *Phys. Rev. D* **105** (Jun, 2022) L111101. Cited on p. 32
89. M. Maltoni, “(eV) sterile neutrinos: Global picture and local views”, in *XXXI International Conference on Neutrino Physics and Astrophysics*. Milan, Italy, June, 2024. <https://agenda.infn.it/event/37867/contributions/233957>. Cited on p. 33
90. A. P. Serebrov, R. M. Samoilov, M. E. Chaikovskii, and O. M. Zhrebtssov, “The result of the Neutrino-4 experiment, sterile neutrinos and dark matter, the fourth neutrino and the Hubble constant”, [arXiv:2302.09958 \[hep-ph\]](https://arxiv.org/abs/2302.09958). Cited on p. 33
91. **NOvA** Collaboration, P. Adamson *et al.*, “Search for active-sterile neutrino mixing using neutral-current interactions in NOvA”, *Phys. Rev. D* **96** (2017) 072006, [arXiv:1706.04592 \[hep-ex\]](https://arxiv.org/abs/1706.04592). Cited on p. 33
92. **MINOS+** Collaboration, P. Adamson *et al.*, “Search for sterile neutrinos in MINOS and MINOS+ using a two-detector fit”, *Phys. Rev. Lett.* **122** (2019) 091803, [arXiv:1710.06488 \[hep-ex\]](https://arxiv.org/abs/1710.06488). Cited on p. 33
93. M. Dentler, Á. Hernández-Cabezudo, J. Kopp, P. A. N. Machado, M. Maltoni, I. Martínez-Soler, and T. Schwetz, “Updated Global Analysis of Neutrino Oscillations in the Presence of eV-Scale Sterile Neutrinos”, *JHEP* **08** (2018) 010, [arXiv:1803.10661 \[hep-ph\]](https://arxiv.org/abs/1803.10661). Cited on pp. 33 and 34
94. **JUNO** Collaboration, B. Yu, “Status and progress of the JUNO liquid scintillator”, *PoS TIPP2023* (2025) 087. Cited on p. 33
95. **ICARUS-WA104, LAr1-ND, MicroBooNE** Collaboration, C. Rubbia, “A Proposal for a Three Detector Short-Baseline Neutrino Oscillation Program in the Fermilab Booster Neutrino Beam”, Tech. Rep. FERMILAB-LOI-2015-01, 1, 2015. [arXiv:1503.01520 \[physics.ins-det\]](https://arxiv.org/abs/1503.01520). Cited on pp. 33, 37, 38, 39, 41, 43, and 48
96. A. Diaz, C. A. Argüelles, G. H. Collin, J. M. Conrad, and M. H. Shaevitz, “Where Are We With Light Sterile Neutrinos?”, *Phys. Rept.* **884** (2020) 1–59, [arXiv:1906.00045 \[hep-ex\]](https://arxiv.org/abs/1906.00045). Cited on p. 35

x      *Bibliography*

97. S. Böser, C. Buck, C. Giunti, J. Lesgourgues, L. Ludhova, S. Mertens, A. Schukraft, and M. Wurm, “Status of Light Sterile Neutrino Searches”, *Prog. Part. Nucl. Phys.* **111** (2020) 103736, [arXiv:1906.01739 \[hep-ex\]](#). [Cited on p. 35](#)
98. R. Triozzi, A. Guglielmi, and D. Gibin, *Study of the Trigger System Performance of the ICARUS T600 Detector at Fermilab Exposed to the Booster and NuMI Neutrino Beams*. M. Sc. thesis, Università degli studi di Padova, Padova, 2023. [Cited on p. 45](#)
99. M. Artero Pons, D. Gibin, and G. Monaco, *Study of the Reconstruction of  $\nu_\mu$ CC QE Events from the Booster Neutrino Beam with the ICARUS Detector*. PhD thesis, Università degli studi di Padova, Padova, 2023. [Cited on pp. 60, 64, 81, 82, 84, 86, and 88](#)
100. P. A. Machado, O. Palamara, and D. W. Schmitz, “The Short-Baseline Neutrino Program at Fermilab”, *Ann. Rev. Nucl. Part. Sci.* **69** (2019) 363–387, [arXiv:1903.04608 \[hep-ex\]](#). [Cited on pp. 37, 39, and 41](#)
101. I. Stancu *et al.*, “Technical Design Report for the 8 GeV Beam”, Tech. Rep. FERMILAB-DESIGN-2001-03, 5, 2001. [Cited on p. 37](#)
102. P. Adamson *et al.*, “The NuMI Neutrino Beam”, *Nucl. Instrum. Meth. A* **806** (2016) 279–306, [arXiv:1507.06690 \[physics.acc-ph\]](#). [Cited on pp. 38 and 41](#)
103. **ICARUS** Collaboration, P. Abratenko *et al.*, “ICARUS at the Fermilab Short-Baseline Neutrino program: initial operation”, *Eur. Phys. J. C* **83** (2023) 467, [arXiv:2301.08634 \[hep-ex\]](#). [Cited on pp. 38, 51, 53, and 60](#)
104. **SBND** Collaboration, R. Acciarri *et al.*, “The Short-Baseline Near Detector at Fermilab: Input to the European Strategy for Particle Physics 2026 Update”, Tech. Rep. FERMILAB-PUB-25-0154-PPD, 3, 2025. [arXiv:2504.00245 \[hep-ex\]](#). [Cited on pp. 38 and 48](#)
105. **ICARUS** Collaboration, F. Abd Alrahman, *et al.*, “Search for a Hidden Sector Scalar from Kaon Decay in the Dimuon Final State at ICARUS”, *Phys. Rev. Lett.* **134** (Apr, 2025) 151801. [Cited on p. 41](#)
106. R. Ainsworth, P. Adamson, B. C. Brown, D. Capista, K. Hazelwood, I. Kourbanis, D. K. Morris, M. Xiao, and M.-J. Yang, “High intensity operation using proton stacking in the fermilab recycler to deliver 700 kw of 120 gev proton beam”, *Phys. Rev. Accel. Beams* **23** (Dec, 2020) 121002. [Cited on p. 42](#)

107. **MiniBooNE** Collaboration, A. A. Aguilar-Arevalo, *et al.*, “Neutrino flux prediction at MiniBooNE”, *Phys. Rev. D* **79** (Apr, 2009) 072002. Cited on p. 43
108. J. N. Marx and D. R. Nygren, “The Time Projection Chamber”, *Phys. Today* **31N10** (1978) 46–53. Cited on p. 44
109. **ALICE** Collaboration, C. Lippmann, “Upgrade of the ALICE Time Projection Chamber”, Tech. Rep. CERN-LHCC-2013-020, ALICE-TDR-016, 3, 2014. Cited on p. 45
110. C. Farnese, “Some recent results from ICARUS”, *AIP Conf. Proc.* **1666** (2015) 110002. Cited on p. 46
111. M. Antonello *et al.*, “Experimental observation of an extremely high electron lifetime with the ICARUS-T600 LAr-TPC”, *JINST* **9** (2014) P12006, [arXiv:1409.5592 \[physics.ins-det\]](https://arxiv.org/abs/1409.5592). Cited on pp. 47 and 51
112. W. M. Bonivento and F. Terranova, “The science and technology of liquid argon detectors”, *Rev. Mod. Phys.* **96** (2024) 045001, [arXiv:2405.01153 \[physics.ins-det\]](https://arxiv.org/abs/2405.01153). Cited on p. 49
113. **ICARUS** Collaboration, S. Amerio *et al.*, “Design, construction and tests of the ICARUS T600 detector”, *Nucl. Instrum. Meth. A* **527** (2004) 329–410. Cited on pp. 49, 50, 51, and 70
114. **ICARUS** Collaboration, M. Antonello *et al.*, “Muon momentum measurement in ICARUS-T600 LAr-TPC via multiple scattering in few-GeV range”, *JINST* **12** (2017) P04010, [arXiv:1612.07715 \[physics.ins-det\]](https://arxiv.org/abs/1612.07715). Cited on p. 51
115. **ICARUS-T600** Collaboration, L. Bagby *et al.*, “Overhaul and Installation of the ICARUS-T600 Liquid Argon TPC Electronics for the FNAL Short Baseline Neutrino Program”, *JINST* **16** (2021) P01037, [arXiv:2010.02042 \[physics.ins-det\]](https://arxiv.org/abs/2010.02042). Cited on p. 54
116. **ICARUS** Collaboration, M. Bonesini, R. Benocci, R. Bertoni, S. Copello, M. Diwan, A. Menegolli, G. L. Raselli, M. Rossella, D. Torretta, and M. Vicenzi, “The upgraded laser calibration system of the ICARUS experiment at FNAL”, *Nucl. Instrum. Meth. A* **1067** (2024) 169670. Cited on p. 55

117. **ICARUS** Collaboration, A. Aduszkiewicz *et al.*, “Design and implementation of the cosmic ray tagger system for the ICARUS detector at FNAL”, *JINST* **20** (2025) T04002, [arXiv:2501.03034 \[hep-ex\]](#). Cited on pp. 56 and 60
118. F. Poppi, *The cosmic ray tagger of the ICARUS detector: construction, commissioning and performances in the first physics run*. PhD thesis, amsdottorato, Alma Mater Studiorum - Università di Bologna, Bologna U., 2023. Cited on p. 64
119. **ICARUS** Collaboration, F. Poppi, “The Cosmic Ray Tagger system of the ICARUS detector at Fermilab”, *PoS ICHEP2022* (2022) 580. Cited on pp. 56 and 60
120. **ICARUS** Collaboration, F. A. Alrahman *et al.*, “Operation of the Trigger System for the ICARUS Detector at Fermilab”, [arXiv:2506.20137 \[hep-ex\]](#). Cited on pp. 57 and 58
121. E. Segreto, “Properties of Liquid Argon Scintillation Light Emission”, *Phys. Rev. D* **103** (2021) 043001, [arXiv:2012.06527 \[physics.ins-det\]](#). Cited on p. 57
122. K. Biery, C. Green, J. Kowalkowski, M. Paterno, and R. Rechenmacher, “artdaq: An Event-Building, Filtering, and Processing Framework”, *IEEE Trans. Nucl. Sci.* **60** (2013) 3764 – 3771. Cited on p. 58
123. C. Green, J. Kowalkowski, M. Paterno, M. Fischler, L. Garren, and Q. Lu, “The Art Framework”, *J. Phys. Conf. Ser.* **396** (2012) 022020. Cited on p. 60
124. R. Brun, *et al.*, “root-project/root: v6.18/02”, Aug., 2019. Cited on p. 60
125. E. D. Church, “LArSoft: A Software Package for Liquid Argon Time Projection Drift Chambers”, [arXiv:1311.6774 \[physics.ins-det\]](#). Cited on p. 60
126. E. L. Snider and G. Petrillo, “LArSoft: Toolkit for Simulation, Reconstruction and Analysis of Liquid Argon TPC Neutrino Detectors”, *J. Phys. Conf. Ser.* **898** (2017) 042057. (Not cited.)
127. R. Pordes and E. Snider, “The Liquid Argon Software Toolkit (LArSoft): Goals, Status and Plan”, in *Proceedings of 38th International Conference on High Energy Physics — PoS(ICHEP2016)*, vol. 282, p. 182. 2017. Cited on p. 60
128. **MicroBooNE** Collaboration, R. Acciarri *et al.*, “Noise Characterization and Filtering in the MicroBooNE Liquid Argon TPC”, *JINST* **12** (2017) P08003, [arXiv:1705.07341 \[physics.ins-det\]](#). Cited on p. 65

129. **ICARUS** Collaboration, P. Abratenko *et al.*, “Calibration and simulation of ionization signal and electronics noise in the ICARUS liquid argon time projection chamber”, *JINST* **20** (2025) P01032, [arXiv:2407.11925 \[hep-ex\]](#). Cited on p. 65
130. **MicroBooNE** Collaboration, C. Adams *et al.*, “Ionization electron signal processing in single phase LArTPCs. Part I. Algorithm Description and quantitative evaluation with MicroBooNE simulation”, *JINST* **13** (2018) P07006, [arXiv:1802.08709 \[physics.ins-det\]](#). Cited on p. 67
131. **MicroBooNE** Collaboration, C. Adams *et al.*, “Ionization electron signal processing in single phase LArTPCs. Part II. Data/simulation comparison and performance in MicroBooNE”, *JINST* **13** (2018) P07007, [arXiv:1804.02583 \[physics.ins-det\]](#). Cited on p. 67
132. **MicroBooNE** Collaboration, R. Acciarri *et al.*, “The Pandora multi-algorithm approach to automated pattern recognition of cosmic-ray muon and neutrino events in the MicroBooNE detector”, *Eur. Phys. J. C* **78** (2018) 82, [arXiv:1708.03135 \[hep-ex\]](#). Cited on pp. 69, 72, 74, 75, and 78
133. F. Drielsma, K. Terao, L. Dominé, and D. H. Koh, “Scalable, End-to-End, Deep-Learning-Based Data Reconstruction Chain for Particle Imaging Detectors”, in *34th Conference on Neural Information Processing Systems*. 2, 2021. [arXiv:2102.01033 \[hep-ex\]](#). Cited on pp. 69, 82, 83, and 84
134. A. Campani, L. Di Noto, A. Fava, and M. Sotgia, “Update on the new training for track vs shower discrimination in Pandora”, Tech. Rep. SBN-doc-37990-v1, ICARUS TPC Reconstruction WG, 2024. Cited on p. 79
135. **ArgoNeuT** Collaboration, R. Acciarri *et al.*, “A Study of Electron Recombination Using Highly Ionizing Particles in the ArgoNeuT Liquid Argon TPC”, *JINST* **8** (2013) P08005, [arXiv:1306.1712 \[physics.ins-det\]](#). Cited on p. 82
136. **DeepLearnPhysics** Collaboration, F. Drielsma, Q. Lin, P. C. de Soux, L. Dominé, R. Itay, D. H. Koh, B. J. Nelson, K. Terao, K. V. Tsang, and T. L. Usher, “Clustering of electromagnetic showers and particle interactions with graph neural networks in liquid argon time projection chambers”, *Phys. Rev. D* **104** (2021) 072004, [arXiv:2007.01335 \[physics.ins-det\]](#). Cited on p. 84

137. C. Andreopoulos, C. Barry, S. Dytman, H. Gallagher, T. Golan, R. Hatcher, G. Perdue, and J. Yarba, “The GENIE Neutrino Monte Carlo Generator: Physics and User Manual”, [arXiv:1510.05494 \[hep-ph\]](https://arxiv.org/abs/1510.05494). [Cited on p. 84](#)
138. I. Mawby, *Optimisation of the search for CP-symmetry violation at the deep underground neutrino experiment*. PhD thesis, University of Warwick, Warwick U., Warwick U., 2023. [Cited on pp. 86, 91, and 130](#)
139. V. C. L. Nguyen, “How to Cheat Pandora”, Tech. Rep. SBN-doc-31192-v1, May, 2023. [Cited on pp. 86, 91, and 130](#)
140. M. Artero Pons, “ICARUS at the Short-Baseline Neutrino Program: First Results”, *Particles* **8** (2025) . [Cited on pp. 86 and 89](#)
141. **ICARUS** Collaboration, M. Artero Pons, *et al.*, “ICARUS  $\nu_\mu$  Disappearance Analysis Technote”, Tech. Rep. SBN-doc-42799-v1, ICARUS  $\nu_\mu$  oscillation task-force, Aug, 2025. [Cited on p. 87](#)
142. S. Dellepiane, L. Di Noto, S. Di Domizio, and M. Pallavicini, *Study and training of a Boosted Decision Tree algorithm for track and shower discrimination in the ICARUS experiment*. M. Sc. thesis, Università degli studi di Genova, Genova, 2023. [Cited on pp. 88 and 89](#)
143. A. Campani, “Track vs shower discrimination in the event reconstruction of the ICARUS experiment”, in *Neutrino 2024*. June, 2024. [Cited on p. 89](#)
144. M. Artero Pons, “Neutrino reconstruction analysis at ICARUS detector”, in *Neutrino 2024*. Zenodo, June, 2024. [Cited on pp. 89 and 94](#)
145. I. Mawby, “Debugging Pandora: Insights from a Pandora developer”, in *FCC-ee Workshop on Particle Flow Reconstruction*. 9, 2025. [Cited on p. 91](#)
146. R. Triozzi, “Impact of reconstruction changes on a NuMI  $\nu_e$  CC  $0\pi$  selection”, Tech. Rep. SBN-doc-41293-v2, May, 2025. [Cited on pp. 120, 123, and 125](#)
147. M. Sotgia, “Update on the status of Pandora reconstruction cheating tests”, Tech. Rep. SBN-doc-42066-v1, Jul, 2025. [Cited on pp. 120 and 123](#)
148. **DUNE** Collaboration, A. A. Abud *et al.*, “Neutrino interaction vertex reconstruction in DUNE with Pandora deep learning”, *Eur. Phys. J. C* **85** (2025) 697, [arXiv:2502.06637 \[hep-ex\]](https://arxiv.org/abs/2502.06637). [Cited on pp. 125 and 126](#)

149. O. Ronneberger, P. Fischer, and T. Brox, “U-net: Convolutional networks for biomedical image segmentation”, [arXiv:1505.04597 \[cs.CV\]](#). Cited on p. 125
150. O. Ronneberger, P. Fischer, and T. Brox, “U-net: Convolutional networks for biomedical image segmentation”, in *Medical Image Computing and Computer-Assisted Intervention – MICCAI 2015*, N. Navab, J. Hornegger, W. M. Wells, and A. F. Frangi, eds., pp. 234–241. Springer International Publishing, Cham, 2015. Cited on p. 125